

ATOMIZATION AND COMBUSTION
OF LIQUID BIOFUELS

by

BENJAMIN MARTIN SIMMONS

AJAY K. AGRAWAL, COMMITTEE CHAIR
DANIEL T. DALY
K. CLARK MIDKIFF
WILLARD C. SCHREIBER
ROBERT P. TAYLOR

A DISSERTATION

Submitted in partial fulfillment of the requirements
for the degree of Doctor of Philosophy
in the Department of Mechanical Engineering
in the Graduate School of
The University of Alabama

TUSCALOOSA, ALABAMA

2011

Copyright Benjamin Martin Simmons 2011
ALL RIGHTS RESERVED

ABSTRACT

Biofuel research will continue to be important as the world seeks to address limited fossil fuel supplies, concerns over greenhouse gases, and demand for energy independence. Biofuels can meet these needs by being a potentially carbon neutral energy source that can be utilized wherever any of a vastly varied feedstock is available. Since much of the energy infrastructure is set up for liquid fuels, liquid biofuels should fill many needs. One common biofuel is biodiesel, produced from bio-oil to match physical properties (like viscosity) of conventional fuels such as diesel. Biodiesel is produced through the transesterification of a source bio-oil and results in the byproduct, glycerol. This study seeks to investigate the combustion performance of a soy biodiesel, the source vegetable oil (VO), and the byproduct glycerol, while using number 2 diesel as the baseline for comparison. This study implements a novel fuel atomization technique known as flow-blurring (FB) atomization to atomize and cleanly combust not only biodiesel but also VO and glycerol. FB atomization uses a simple geometry to create a two-phase air/fuel mixture upstream of an orifice to produce which results in very fine sprays which burn cleanly and produce lower CO and NO_x as compared to standard air-blast (AB) fuel injectors.

First, the combustion performance of biodiesel and VO are compared to a diesel baseline. Results indicate that the FB mechanism provides a simple technique that can be used to successfully atomize and combust VO with resulting emissions comparable to diesel fuel. It was also observed that the FB atomizer incurred no adverse pressure drop penalties when operating with VO or biodiesel. Next, a study into the combustion performance of glycerol was conducted. First glycerol was co-fired with methane in an un-insulated quartz combustor. Results show high

combustion efficiency, although CO emissions at the combustor wall were high (~5000 ppm) because of heat loss. Insulating the combustor made it possible to burn pure glycerol flames. An optimum air to liquid mass ratio (ALR) was found and used to investigate combustion performance at three different heat release rates. Residence time in the combustor was found to be an important parameter to achieve low CO emissions. Finally, glycerol/ methane flames were investigated in the insulated chamber to demonstrate dual fuel capabilities of the combustor. The emissions were minimized by splitting methane flow between primary and atomizing air lines.

Next, spray characteristics of the FB atomizer were compared to the AB atomizer using a phase Doppler particle analyzer (PDPA) system. Results for water as the liquid show that the FB atomizer produces sprays with smaller droplets and also a narrower range of droplet sizes. The FB injector also incurred a smaller pressure drop in the atomizing air line. The FB atomizer incurred higher pressure drop in the liquid supply line resulting from the intense two-phase mixing at the tip of the liquid tube. Next, non-reacting VO and diesel sprays were compared using the PDPA technique. Diesel sprays resulted in smaller droplets compared to VO sprays. Upon further investigation it was revealed that the majority of the fuel mass flow within both sprays passes through a region with similar droplet diameter. Therefore, the mass-weighted Sauter mean diameter (SMD) was similar for VO and diesel sprays in spite of the large difference in their kinematic viscosity.

Finally, a reacting glycerol spray flame was investigated with the PDPA technique to establish velocity and droplet size trends. Glycerol sprays contain droplets comparable to those from VO cold sprays. In summary, this study establishes the potential of the FB atomizer: the ability to successfully atomize and combust highly viscous fuels with performance much superior to AB atomizers.

LIST OF ABBREVIATIONS AND SYMBOLS

| | |
|-----------------|--|
| AA | Atomizing air |
| AB | Air-blast |
| ALR | Air to liquid mass ratio through fuel injector |
| CO | Carbon monoxide |
| EA | Effervescent atomization |
| FB | Flow-blurring |
| HRR | Heat release rate |
| NO _x | Nitric oxides |
| PDPA | Phase Doppler particle analyzer |
| PM | Particulate matter |
| VO | Fully refined soybean oil |

ACKNOWLEDGEMENTS

I would like to thank my research advisor and dissertation committee chair, Ajay K. Agrawal, for his support and guidance throughout my graduate work. I am also indebted to the other members of my committee including Dan Daly, Clark Midkiff, Will Schreiber, and Bob Taylor for their input on this dissertation. I would also like to thank the staff in the Department of Mechanical Engineering including Lynn Hamric, Lisa Hinton, Betsy Singleton, Barry Johnson, and Pamela Bedingfield. The timely support of Ken Dunn, Jim Edmonds, Sam Tingle, and James Yarbrough in the Engineering Machine Shop has also been critical in fabricating and maintaining experimental setups. I also appreciate the help and camaraderie of Dr. Agrawal's former and current students: Tanisha Booker, Allison Copus, Troy Dent, Seydou Diop, Lulin Jiang, Pankaj Kolhe, Joseph Meadows, Dan Mitchell, Yonas Niguse, Heena Panchasara, Daniel Sequera, Zach Smith, and Justin Williams.

The author also acknowledges U. S. Department of Education GAANN fellowship program for financial assistance throughout graduate studies. Southern Company supported combustion research of biodiesel and diesel/vegetable oil blends presented in chapter 1. Glycerol research was supported in part by the U. S. Department of Energy.

CONTENTS

| | |
|--|----|
| ABSTRACT..... | ii |
| LIST OF ABBREVIATIONS AND SYMBOLS..... | iv |
| ACKNOWLEDGEMENTS..... | v |
| LIST OF TABLES..... | ix |
| LIST OF FIGURES..... | x |
| 1. INTRODUCTION | 1 |
| 1.1 Background | 1 |
| 1.2 Combustion Performance of an AB Atomizer..... | 2 |
| 1.2.1 Experimental Setup..... | 2 |
| 1.2.2 Results and Discussion..... | 4 |
| 1.3 Concluding Remarks..... | 8 |
| 1.4 Objectives..... | 9 |
| 1.5 Overview..... | 9 |
| 2. BIO-OIL COMBUSTION USING FLOW-BLURRING ATOMIZATION..... | 17 |
| 2.1 Background | 17 |
| 2.2 Experimental Setup | 20 |
| 2.3 Results and Discussions | 23 |
| 2.3.1 Visual Flame Images | 23 |
| 2.3.2 Emissions Measurements..... | 23 |
| 2.3.3 Comparison of FB and AB Atomization..... | 25 |

| | |
|--|----|
| 2.3.4 Pressure Drop Measurements..... | 25 |
| 2.4 Conclusions | 26 |
| 3. GLYCEROL COMBUSTION USING FLOW-BLURRING ATOMIZATION..... | 41 |
| 3.1 Background | 41 |
| 3.2 Experimental Setup | 44 |
| 3.3 Results and Discussion | 47 |
| 3.3.1 Un-Insulated Combustion Chamber..... | 47 |
| 3.3.2 Effect of Air to Liquid Mass Ratio (ALR)..... | 49 |
| 3.3.3 Effect of Heat Release Rate (HRR)..... | 50 |
| 3.3.4 Effect of Methane Addition..... | 51 |
| 3.4 Conclusions | 52 |
| 4. FLOW AND DROPSIZE MEASUREMENTS IN WATER SPRAYS..... | 68 |
| 4.1 Background | 68 |
| 4.2 Experimental Setup | 71 |
| 4.3 Results and Discussion | 74 |
| 4.3.1 Pressure Measurements..... | 74 |
| 4.3.2 Spray Images | 76 |
| 4.3.3 Sauter Mean Diameter..... | 77 |
| 4.3.4 Droplet Diameter Distributions..... | 78 |
| 4.3.5 Mean and RMS Velocities..... | 79 |
| 4.3.6 Effect of Air-to-Liquid Mass Ratio..... | 80 |
| 4.4 Conclusions | 82 |
| 5. FLOW AND DROPSIZE MEASUREMENTS IN NON-REACTING BIODIESEL AND VEGETABLE OIL SPRAYS..... | 97 |

| | |
|---|-----|
| 5.1 Background | 97 |
| 5.2 Experimental Setup | 101 |
| 5.3 Results and Discussion | 103 |
| 5.3.1 Pressure Measurements..... | 103 |
| 5.3.2 PDPA Measurements | 103 |
| 5.3.3 Effect of ALR..... | 107 |
| 5.4 Conclusions | 108 |
| 6. FLOW AND DROPSIZE MEASUREMENTS IN GLYCEROL SPRAY FLAMES..... | 130 |
| 6.1 Background | 130 |
| 6.2 Experimental Setup | 133 |
| 6.3 Results and Discussions | 135 |
| 6.4 Conclusions..... | 137 |
| 7. CONCLUSIONS AND RECOMMENDATIONS..... | 161 |
| 7.1 Conclusions | 161 |
| 7.2 Recommendations | 163 |
| REFERENCES | 165 |
| APPENDIX A..... | 170 |
| APPENDIX B..... | 172 |
| APPENDIX C..... | 174 |
| APPENDIX D..... | 176 |
| APPENDIX E..... | 178 |
| APPENDIX F..... | 182 |

LIST OF TABLES

| | | |
|-----|--|----|
| 2.1 | Fuel properties..... | 18 |
| 3.1 | Chemical and physical properties of fuels..... | 42 |
| 3.2 | Temperature measurements from insulated combustor..... | 46 |
| 5.1 | Physical properties of fuels..... | 99 |

LIST OF FIGURES

| | | |
|------|---|----|
| 1.1 | Schematic of the experimental setup; all dimensions in cm..... | 11 |
| 1.2 | (a) Schematic of a swirler; (b) air assist injector schematic and picture..... | 12 |
| 1.3 | Radial profiles of CO and NO _x emissions at the combustor exit plane for diesel and biodiesel fuels: (a) and (b), profiles for 15% AA; (c) and (d), profiles for 25% AA..... | 13 |
| 1.4 | Axial profiles of CO and NO _x emissions at the combustor exit plane for diesel and biodiesel fuels: (a) and (b), profiles for 15% AA; (c) and (d), profiles for 25% AA..... | 14 |
| 1.5 | Radial profiles of CO and NO _x emissions at the combustor exit plane for diesel and diesel-VO blends: (a) and (b), profiles for 15% AA; (c) and (d), profiles for 25% AA.... | 15 |
| 1.6 | Axial profiles of CO and NO _x emissions at the combustor exit plane for diesel and diesel-VO blends: (a) and (b), profiles for 15% AA; (c) and (d), profiles for 25% AA.... | 16 |
| 2.1 | FB atomization concept..... | 28 |
| 2.2 | Experimental setup..... | 29 |
| 2.3 | Predicted adiabatic flame temperatures..... | 30 |
| 2.4 | Flame images at constant Q (a) diesel, (b) biodiesel, (c) VO(scale in cm)..... | 31 |
| 2.5 | CO emissions at combustor exit plane, ALR = 2.0..... | 32 |
| 2.6 | NO _x emissions at combustor exit plane, ALR = 2.0..... | 33 |
| 2.7 | CO emissions at combustor exit plane, ALR = 3.0..... | 34 |
| 2.8 | NO _x emissions at combustor exit plane, ALR = 3.0..... | 35 |
| 2.9 | CO emissions at combustor exit plane, ALR = 4.0..... | 36 |
| 2.10 | NO _x emissions at combustor exit plane, ALR = 4.0..... | 37 |

| | | |
|------|---|----|
| 2.11 | Comparison of CO emissions between FB and AB injectors, ALR = 2.0..... | 38 |
| 2.12 | Comparison of NO _x emissions between FB and AB injectors, ALR = 2.0..... | 39 |
| 2.13 | Fuel and atomizing air supply pressure..... | 40 |
| 3.1 | FB injection concept..... | 53 |
| 3.2 | Experimental setup..... | 54 |
| 3.3 | Effect of glycerol content on flame images..... | 55 |
| 3.4 | Effect of glycerol content on reaction zone from chemiluminescence images..... | 56 |
| 3.5 | CO emissions from un-insulated combustion chamber..... | 57 |
| 3.6 | NO _x emissions from un-insulated combustion chamber..... | 58 |
| 3.7 | Effect of ALR on heat loss through insulated combustor wall..... | 59 |
| 3.8 | Effect of ALR on CO emissions at exit plane of insulated combustor..... | 60 |
| 3.9 | Effect of ALR on NO _x emissions at exit plane of insulated combustor..... | 61 |
| 3.10 | Effect of HRR on heat loss through insulated combustor wall..... | 62 |
| 3.11 | Effect of HRR on CO emissions at exit plane of insulated combustor..... | 63 |
| 3.12 | Effect of HRR on NO _x emissions at exit plane of insulated combustor..... | 64 |
| 3.13 | Effect of methane addition on heat loss through insulated combustor wall..... | 65 |
| 3.14 | Effect of methane addition on CO emissions at exit plane of insulated combustor..... | 66 |
| 3.15 | Effect of methane addition on NO _x emissions at exit plane of insulated combustor..... | 67 |
| 4.1 | FB injection concept..... | 84 |
| 4.2 | Spray setup schematic..... | 85 |
| 4.3 | Detailed view of fluid path in: (a) Flow-Blurring (FB) injector; (b) Air-Blast (AB) injector..... | 86 |
| 4.4 | Pressure data: (a) atomizing air pressure drop; (b) liquid pressure drop without atomizing airflow; (c) liquid supply and exit pressures..... | 87 |

| | | |
|------|---|-----|
| 4.5 | Laser sheet spray images for FB atomizer (water, 12.0 mlpm) for ALRs ranging from 1.0 to 4.0 (dimensions in mm)..... | 88 |
| 4.6 | Laser sheet spray images for AB atomizer (water, 12.0 mlpm) for ALRs ranging from 1.0 to 4.0 (dimensions in mm) | 89 |
| 4.7 | SMD for FB and AB atomizers: (a) Y = 1.0 cm; (b) Y = 2.0 cm; (c) Y = 3.0 cm..... | 90 |
| 4.8 | Droplet diameter distributions for FB and AB atomizers: (a) Y = 1.0 cm, r = 0.7 cm; (b) Y = 3.0 cm, r = 0.0 cm; (c) Y = 3.0 cm, r = 0.5 cm..... | 91 |
| 4.9 | Cumulative volume fraction distributions for FB and AB atomizers: (a) Y = 1.0 cm, r = 0.7 cm; (b) Y = 3.0 cm, r = 0.0 cm; (c) Y = 3.0 cm, r = 0.5 cm..... | 92 |
| 4.10 | Axial velocity profiles for FB and AB atomizers: (a) Y = 1.0 cm; (b) Y = 2.0 cm; (c) Y = 3.0 cm..... | 93 |
| 4.11 | RMS Axial velocity profiles for FB and AB atomizers: (a) Y = 1.0 cm; (b) Y = 2.0 cm; (c) Y = 3.0 cm..... | 94 |
| 4.12 | Effect of ALR on SMD, axial velocity, and RMS axial velocity for FB injector: (a), (c), (e) Y = 1.0 cm; (b), (d), (e) Y = 3.0 cm..... | 95 |
| 4.13 | Effect of ALR on SMD, axial velocity, and RMS axial velocity for AB injector: (a), (c), (e) Y = 1.0 cm; (b), (d), (e) Y = 3.0 cm..... | 96 |
| 5.1 | VO and diesel CO and NO _x emissions..... | 110 |
| 5.2 | FB injection concept..... | 111 |
| 5.3 | Experimental setup..... | 112 |
| 5.4 | Fuel and atomizing air supply pressure..... | 113 |
| 5.5 | SMD profiles, ALR = 2..... | 114 |
| 5.6 | Droplet distribution at Z = 20 mm, R = 0 mm..... | 115 |
| 5.7 | Droplet distribution at Z = 20 mm, R = 8 mm..... | 116 |
| 5.8 | Cumulative volume distribution at Z = 20 mm, R = 0 mm..... | 117 |
| 5.9 | Cumulative volume distribution at Z = 20 mm, R = 8 mm..... | 118 |
| 5.10 | Axial velocity, ALR = 2..... | 119 |

| | | |
|------|--|-----|
| 5.11 | Axial turbulence intensity, ALR = 2..... | 120 |
| 5.12 | Swirl velocity, ALR = 2..... | 121 |
| 5.13 | RMS swirl velocity, ALR = 2..... | 122 |
| 5.14 | Axial volume flow, ALR = 2..... | 123 |
| 5.15 | SMD profiles..... | 124 |
| 5.16 | Axial velocity profiles..... | 125 |
| 5.17 | Axial turbulence intensity profiles..... | 126 |
| 5.18 | Swirl velocity profiles..... | 127 |
| 5.19 | RMS swirl velocity profiles..... | 128 |
| 5.20 | Axial volume flow profiles..... | 129 |
| 6.1 | CO emissions at exit of insulated combustion chamber..... | 139 |
| 6.2 | NO _x emissions at exit of insulated combustion chamber..... | 140 |
| 6.3 | FB injection concept..... | 141 |
| 6.4 | Experimental setup..... | 142 |
| 6.5 | Insulated pentagonal enclosure with optical access..... | 143 |
| 6.6 | Diagram of PDPA setup, traverse, and pentagonal enclosure..... | 144 |
| 6.7 | Diagram of PDPA pentagonal enclosure..... | 145 |
| 6.8 | Diagram of spray and flame location in pentagonal insulated combustor..... | 146 |
| 6.9 | Mean axial velocity profiles of three cases..... | 147 |
| 6.10 | RMS axial velocity profiles of three cases..... | 148 |
| 6.11 | Mean radial velocity profiles of three cases..... | 149 |
| 6.12 | RMS radial velocity profiles of three cases..... | 150 |
| 6.13 | Mean swirl velocity profiles of three cases..... | 151 |

| | | |
|------|--|-----|
| 6.14 | RMS swirl velocity profiles of three cases..... | 152 |
| 6.15 | SMD profiles of three cases..... | 153 |
| 6.16 | Droplet diameter distribution at R = 10 mm..... | 154 |
| 6.17 | Cumulative volume distribution at R = 10 mm..... | 155 |
| 6.18 | Droplet diameter distribution at R = 20 mm..... | 156 |
| 6.19 | Cumulative volume distribution at R = 20 mm..... | 157 |
| 6.20 | Droplet diameter distribution at R = 30 mm..... | 158 |
| 6.21 | Cumulative volume distribution at R = 30 mm..... | 159 |
| 6.22 | Axial glycerol volumetric flow rate as measured by PDPA..... | 160 |

CHAPTER 1

INTRODUCTION

1.1 Background

Despite increased utilization of wind, solar, and other emerging alternative energy sources, the combustion of fuels still supplies the majority of the world's energy needs. Combustion is the simple exothermic reaction of fuel and oxidizer, mainly air, used to harvest the released energy. Combustion systems can operate on solid, liquid, or gaseous fuels, with liquid fuels being common in applications such as internal combustion engines, aircraft engines, and home furnaces. This study focuses on the atomization and combustion of liquid biofuels.

Biofuels are fuels produced from renewable biological sources such as plant or animal matter. Biofuels are unique in that they have the possibility of one day becoming carbon neutral, meaning any carbon released would have been absorbed during the fuel's life cycle. Biofuels also offer other benefits: allowing energy independence and providing a renewable energy source that will be around long after the world's fossil fuel reserves are exhausted. Biodiesel, one of the most common biofuels is created to match the physical properties of diesel. Thus, a device using diesel can also be operated on biodiesel without major hardware changes, for example, to the fuel injection system.

A fuel injector facilitates atomization, a process of breaking up a bulk liquid into droplets. Fuel droplets vaporize and the fuel vapor mixes and reacts with the surrounding air. Finer droplets result in faster vaporization, increased premixing of fuel and air, lower flame temperatures, and cleaner combustion. All flames in this study pertain to overall fuel lean

(equivalence ratio, Φ , < 1) partially premixed combustion to reduce the flame temperature. A further explanation of equivalence ratio calculations is given in appendix A. The following section introduces the methods used to assess combustion performance of a conventional air-blast (AB) atomizer operated on different fuels.

1.2 Combustion Performance of an AB Atomizer

1.2.1 Experimental Setup

The test apparatus for assessing AB injector performance, shown schematically in figure 1.1, consists of the combustor assembly and the injector assembly. The primary air enters the system through a plenum filled with marbles to breakdown the large vortical structures. The air passes through a swirler into the mixing section, where the gaseous fuel is supplied during the startup. The reactants or primary-air enter the combustor through a swirler section shown schematically in figure 1.2(a). The swirler is used to enhance fuel-air mixing and it also helps to stabilize the flame. The swirler has six vanes positioned at 28° to the horizontal to produce swirl number of about 1.5. The bulk axial inlet velocity of the primary air is 1.9 to 2.1 m/s, which resulted in Reynolds number (based on the equivalent diameter of the injector) varying from 5960 to 6750. An example of Reynolds number calculations is given in appendix B. The combustor is enclosed within an 8.0 cm inside diameter, 46 cm long quartz tube, and it is back-side cooled by natural convection. The liquid fuel is supplied to the injector with separate concentric tube inlets for fuel and atomization air.

The injector system runs through the plenum and the mixing chamber. An O-ring within a sleeve is located at the bottom of the plenum to prevent air leakage. A commercial air-blast atomizer (Delavan Siphon type SNA nozzle) with its details shown schematically and photographically in figure 1.2(b) was used for the experiments. This commercial atomizer

creates a swirling flow of atomizing air to breakdown the fuel jet as the fluids exit the orifice plate. The liquid fuel was supplied by a peristaltic pump with reported calibration error of +/- 0.25% of the flow rate reading ranging from 12 ml/min to 130 ml/min in steps of 2 ml/min. Viton tubes were used to prevent degradation of the fuel lines. A 25 micron filter was placed in the fuel supply line to prevent dirt and foreign particles from entering into the injector.

The primary and atomizing air was supplied by an air compressor. The air passed through a pressure regulator, and a dehumidifier and water traps to remove the moisture. Then, the air was split into primary air supply and atomizing air supply lines. The primary air flow rate was measured by a laminar flow element (LFE) with reported calibration error of +/- 5 liters per minute (lpm). The pressure drop across the LFE was measured by a differential pressure transducer. An absolute pressure transducer was used to measure air pressure in the LFE. The flow rate measured by the LFE is corrected for temperature and pressure as specified by the manufacturer. The atomizing airflow rate was measured by calibrated mass flow meter with measurement uncertainty of +/- 1.5 lpm. The product gas was sampled continuously by a quartz probe (OD = 7.0 mm) attached to a three-way manual traversing system. The upstream tip of the probe was tapered to 1 mm ID to quench reactions inside the probe. The probe was traversed in the axial direction at the center of the combustor and in the radial direction at the combustor exit plane. The gas sample passed through an ice bath and water traps to remove moisture upstream of the gas analyzers. The dry sample entered the electrochemical analyzers to measure concentrations of CO and NO_x in ppm. The analyzer also measured oxygen and carbon dioxide concentrations, which were used to cross-check the equivalence ratio computed from the measured fuel and air flow rates. An example of this cross-check method is given in appendix C.

The uncorrected emissions data on dry basis are reported with uncertainty of +/-2 ppm. Further details of measurement uncertainty are given in appendix D.

The experiment was started by supplying gaseous methane and then igniting the methane-air reactant mixture in the combustor. Next, the liquid fuel flow rate was gradually increased to attain the desired value, while the methane flow rate was slowly decreased to zero. In this study, the volume flow rate of total air (primary + atomizing) was constant at 150 standard liters per minute (slpm). Experiments were conducted for fixed volume flow rate of fuel and for fixed heat release rate in the combustor. For the latter case, the volume flow rate of biodiesel fuels was increased to match the heat release rate of the diesel fuel. In case of diesel-VO blends, the fuel volume flow rate approximated the heat release rate and hence, no flow rate adjustment was necessary. Previous studies have shown significant effect of atomizing airflow rate (AA) on emissions of NO_x and CO (Sequera et al., 2007). Hence, atomizing airflow rates of 15% and 25% of the total air flow rate were used for experiments with all fuels considered in this study. These atomizing airflow rates can also be expressed in terms of air-to-liquid mass ratio (ALR) through the injector. In this manner, AA of 15% and 25% can be expressed as ALRs of 2.4 to 2.7 and 3.9 to 4.5, respectively. The spray was also photographed without the flame to determine the cone angle for different fuels.

1.2.2 Results and Discussion

Figures 1.3(a)-(b) present radial profiles of CO and NO_x emissions at the combustor exit plane, i.e., $z = 46$ cm, when 15% of the total airflow rate (AA = 15%) is used for fuel atomization. Results are shown for diesel and both biodiesel fuels, with the diesel serving as the reference fuel. In case of biodiesels, data are reported for a fixed fuel volume flow rate (same as that of diesel, constant V) and for a fixed heat input rate (same as that of diesel, constant Q).

Figure 1.3(a) shows a typical parabolic profile with higher CO emissions near the center and decreasing values near the combustor wall. This trend is caused by the fuel-air mixing processes, which confine the flame to the center region and shield it from the combustor wall. Minor asymmetry in radial profiles is attributed to minor imperfections in the injector/swirler geometry and large turbulent flame fluctuations.

For a fixed fuel flow rate (constant V), the CO emissions for diesel are higher than those for biodiesel fuels. The two biodiesel CO emissions profiles overlap, indicating negligible effect of the fatty oil source (vegetable oil or animal fat). For a fixed heat input rate (constant Q), the CO emissions for biodiesels are higher than those for diesel. Again, the CO profiles for the two biodiesel fuels are similar. These results illustrate that biodiesel can be incorrectly characterized as cleaner fuel compared to diesel, based on data obtained for a fixed fuel flow rate. Since the gas turbine must generate the same power regardless of the fuel, the comparison based on fixed heat input rate is more appropriate. In this case, biodiesel CO emissions exceed those for diesel. Higher CO emissions for biodiesel do not pertain to the fuel chemistry effects alone. Later on, it will be shown that the flow effects such as fuel atomization (intimately related to fuel kinematic viscosity and injector design) can dominate emissions from the combustor. Overall, the CO emissions for all of the cases are within 30 ppm.

Radial profiles of NO_x emissions shown in figure 1.3(b) provide support to the above discussion. For constant V , the NO_x emissions for both biodiesels are lower than those for diesel. The profiles for the two biodiesels are nearly identical, indicating negligible effect of fatty oil source on NO_x emissions. Interestingly, for constant Q , the NO_x profiles for all three fuels overlap each other. The NO_x emissions are relatively high, approximately 150 ppm. If the thermal mechanism is dominant, the NO_x emissions can be correlated to the flame temperature,

which remains constant for constant Q . These results suggest that the NO_x is formed mainly by the thermal mechanism, and that the fuel chemistry has a negligible effect on NO_x emissions.

The superiority of flow effects in comparison to chemical effects is illustrated by the result presented in figures 1.3(c)-(d). In this case, the total air and fuel flow rates are identical to those in figures 1.3(a)-(b). However, a larger percentage of the total airflow rate ($AA = 25\%$) is routed through the fuel injector to improve atomization, and hence, the fuel-air mixing processes. Results show that improved atomization associated with higher AA leads to dramatic reductions in CO and NO_x emissions for diesel and biodiesel fuels. The CO emissions show nearly five-fold decrease, with single digit CO concentrations measured for all of the cases. In figure 1.3(c), the CO profiles for different fuels are within the measurement uncertainty of the gas analyzer.

The radial profiles in figure 1.3(d) show more than 15-fold decrease in NO_x emissions compared to the data for $AA = 15\%$ presented in figure 1.3(b). The NO_x emissions for diesel are higher than those with biodiesels for constant V and lower than those with biodiesels for constant Q . However, the difference among various cases is rather small. The maximum NO_x concentration is only about 11 ppm compared to the maximum of about 150 ppm for $AA = 15\%$.

Clearly, the fuel atomization and associated flow processes dominate emissions from the combustor. Thus, in principle, one can optimize the fuel injector to overcome the negative effects of the fuel chemistry, for example, by adjusting the atomizing airflow rate and/or injector geometry for each fuel.

Figure 1.4 presents CO and NO_x emissions profiles at the centerline of the combustor. The axial distance in these profiles is measured from the combustor inlet plane. Figure 1.4(a) shows a decrease of CO emissions in the axial direction. Initially, the fuel decomposes in the flame region to produce high CO concentrations. Subsequently, the CO decreases as the

products pass through the combustor to attain the residence time needed to complete the oxidation reactions. The overall trends for various cases are similar to those presented in figure 1.3(a); the CO emissions for biodiesel fuels with constant V are lower and with constant Q are higher than those with diesel fuel. Higher measurement uncertainties can be expected for the data in figure 1.4(a), because of the large turbulent fluctuations in the flame region, i.e., $z < 25$ cm. Axial profiles in figure 1.4(b) show that the NO_x emissions are nearly constant in the axial direction for $z > 15$ cm. Thus, NO_x is formed within $z = 15$ cm or in a short reaction zone. The NO_x emissions for both biodiesel fuels are nearly the same, and for constant V, they are lower than the NO_x emissions for diesel. Axial profiles in figure 1.4(c)-(d) were taken for the higher atomizing airflow rate ($\text{AA} = 25\%$), and they represent the trends discussed previously; i.e., CO and NO_x emissions decrease dramatically for higher atomizing airflow rate. Overall, results illustrate the significance of fluid dynamics effects on emissions from combustion of diesel and biodiesel fuels in the present burner replicating continuous flow operation of gas turbines for power generation.

Figure 1.5 presents radial profiles of CO and NO_x emissions at the combustor exit plane for diesel and diesel-VO blends. Because of the high diesel concentration in blends, constant V and constant Q cases were essentially equivalent, and hence, experiments were conducted for constant V only. Figure 1.5(a) shows that the diesel-VO blends produced slightly higher CO emissions compared to diesel. Higher viscosity of the blends, and deterioration in fuel atomization associated with it, are the likely cause for this result. The low volatility of VO is another factor, since the droplets of the blended fuels will be more difficult to vaporize compared to diesel. Although the relative importance of these factors cannot be ascertained, data suggest the fuel chemistry effects on CO emissions are minor. This result is supported by radial profiles

of NO_x emissions in figure 1.5(b). The NO_x emissions for diesel-VO blends are slightly higher than those for diesel. For all cases, the NO_x emission is high, approximately 150 ppm, which matches NO_x values for biodiesel fuels. Results suggest that the flame temperature or the heat input rate is the determining factor affecting NO_x emissions for all fuels in this study. Similar to biodiesel fuels, the CO and NO_x emissions for diesel-VO blends decrease dramatically with increase in the atomizing airflow rate (see figures 1.5c-d). The CO emissions decreased by a factor of 5 and the NO_x emissions decreased by a factor of 15 as AA was changed from 15% to 25%. In spite of the different physical and chemical properties of diesel, biodiesels, and diesel-VO blends, CO and NO_x emissions for all fuels are nearly the same for AA = 25%.

The axial profiles of CO and NO_x emissions at the combustor centerline are presented in figure 1.6. After the CO is formed in the reaction zone, it is oxidized along the length of the combustor, especially in the post flame region around $z = 20$ cm. The NO_x emissions are independent of the axial location, suggesting that NO_x is formed within the reaction zone located at $z < 15$ cm. Data suggest that CO and NO_x emissions for diesel-VO blends are slightly higher than those for diesel.

1.3 Concluding Remarks

While the AB atomizer is effective for the atomization of diesel, biodiesel, and diesel-VO blends, it is unable to successfully atomize straight VO for combustion. The AB atomizer relies on an atomizing air stream interacting with a fuel stream at high relative velocities. This velocity difference creates shear stresses that destabilize the fuel jet. Instabilities in the fuel surface grow and cause the formation of droplets. Physical properties that suppress these instabilities (high viscosity and surface tension) limit the fuels that can be properly atomized with an AB injector. Fuel heating and mixing can be used to improve fuel physical properties, but both require energy

and effort, thereby increasing fuel costs. Therefore, a passive technique for overcoming this problem would be desirable. The flow-blurring (FB) atomization technique offers a passive solution by providing a simple atomization method that is insensitive to fuel physical properties. The FB method will be described and discussed throughout this work.

1.4 Objectives

The objectives of this study are to investigate the atomization and combustion performance of the FB atomization technique and its application to biofuels through detailed combustion and spray studies. The ultimate motivation is to demonstrate a technique of fuel atomization that allows biofuels and waste products to be utilized without fuel treatment, thus eliminating energy and cost, while broadening the market for domestically available biofuels.

1.5 Overview

1. In chapter 2 the FB atomization technique is presented. Because of VO's high viscosity (about 13 times that of diesel), it has proven difficult to atomize VO using standard AB atomization methods. The FB atomization concept does not rely heavily on fuel physical properties and therefore is well suited for viscous fuels. Combustion performance is assessed using visual flame images, CO and NO_x emissions, and supply pressure data. Experiments are conducted with VO as well as diesel and biodiesel for comparison. Finally, results are compared to those from an AB injector to document the improvement in the combustion performance.
2. In chapter 3 the FB concept is applied to an even more highly viscous fluid, glycerol. Glycerol's high kinematic viscosity (about 190 times that of diesel) makes it virtually impossible to atomize it using AB atomization without fuel preheating or blending with other low viscous fuels. Several experimental parameters are studied, namely the air to

liquid mass ratio (ALR) and total flow rate (or heat release rate) in the combustion system. The effect of methane addition is also studied as a means of exploiting the combustor's dual fuel capabilities. Results are presented for both un-insulated and insulated combustion chambers. Combustion performance is documented by heat loss measurements and CO and NO_x emissions.

3. In chapter 4, a detailed comparison between water sprays produced by AB and FB injectors is conducted using the phase Doppler particle analyzer (PDPA) technique to understand the differences in the performance of the two injectors. This study provides velocity and drop size statistics to quantitatively assess the atomizer performance. Measurements are obtained in water sprays for simplicity and safety. Qualitative laser spray visualization is also used to compare injector characteristics.
4. In chapter 5 the PDPA technique is applied to VO cold flow sprays produced by the FB injector to assess atomization performance and explain emissions results from chapter 2. Measurements are also obtained in diesel sprays as a baseline. Again, velocity and droplet diameter statistics are presented to highlight the difference in the resulting VO and diesel sprays without the flame.
5. Chapter 6 presents PDPA measurements for glycerol spray flames (without and with methane addition) in an insulated enclosure to understand flow characteristics and thus explain emissions measurements presented in chapter 3. Velocity and droplet diameter data are presented as a means of quantifying the effect of these parameters.
6. Chapter 7 integrates the findings of the individual chapters and presents the conclusions from the studies and comments on the effectiveness of the FB atomization technique. Recommendations for future work are also provided.

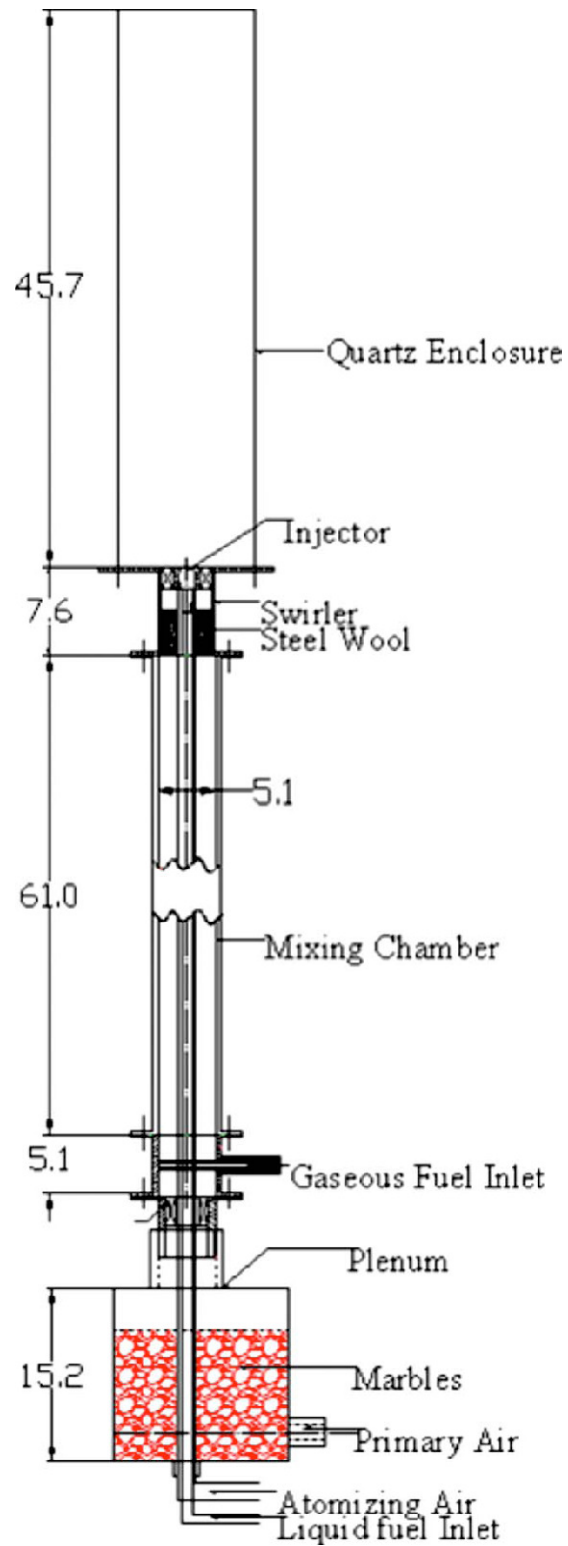


Figure 1.1 Schematic of the experimental setup; all dimensions in cm

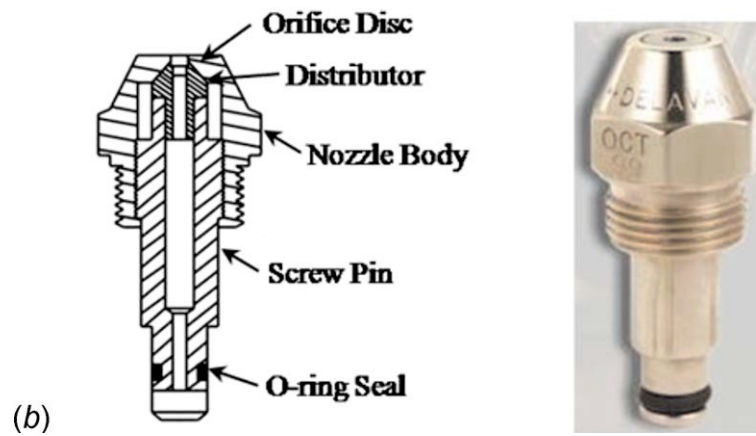
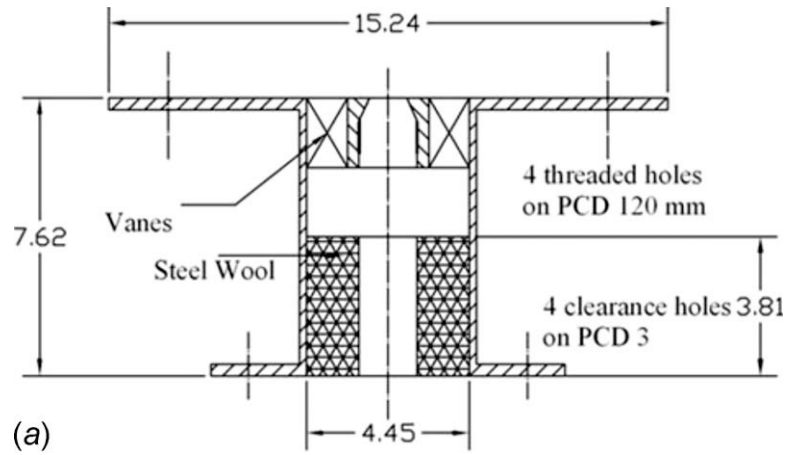


Figure 1.2 (a) Schematic of a swirler; (b) air assist injector schematic and picture, dimensions in cm

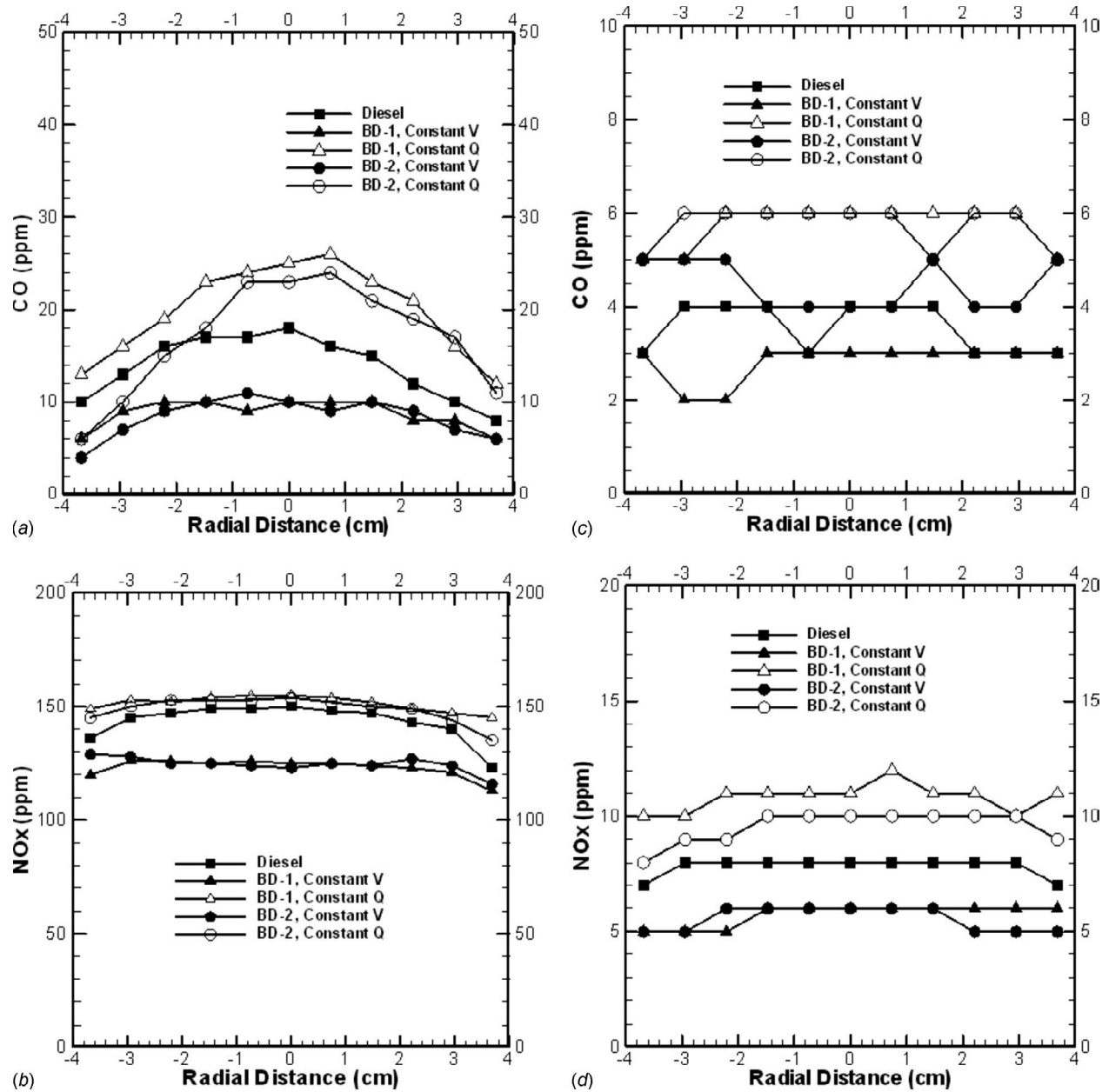


Figure 1.3 Radial profiles of CO and NO_x emissions at the combustor exit plane for diesel and biodiesel fuels: (a) and (b), profiles for 15% AA; (c) and (d), profiles for 25% AA

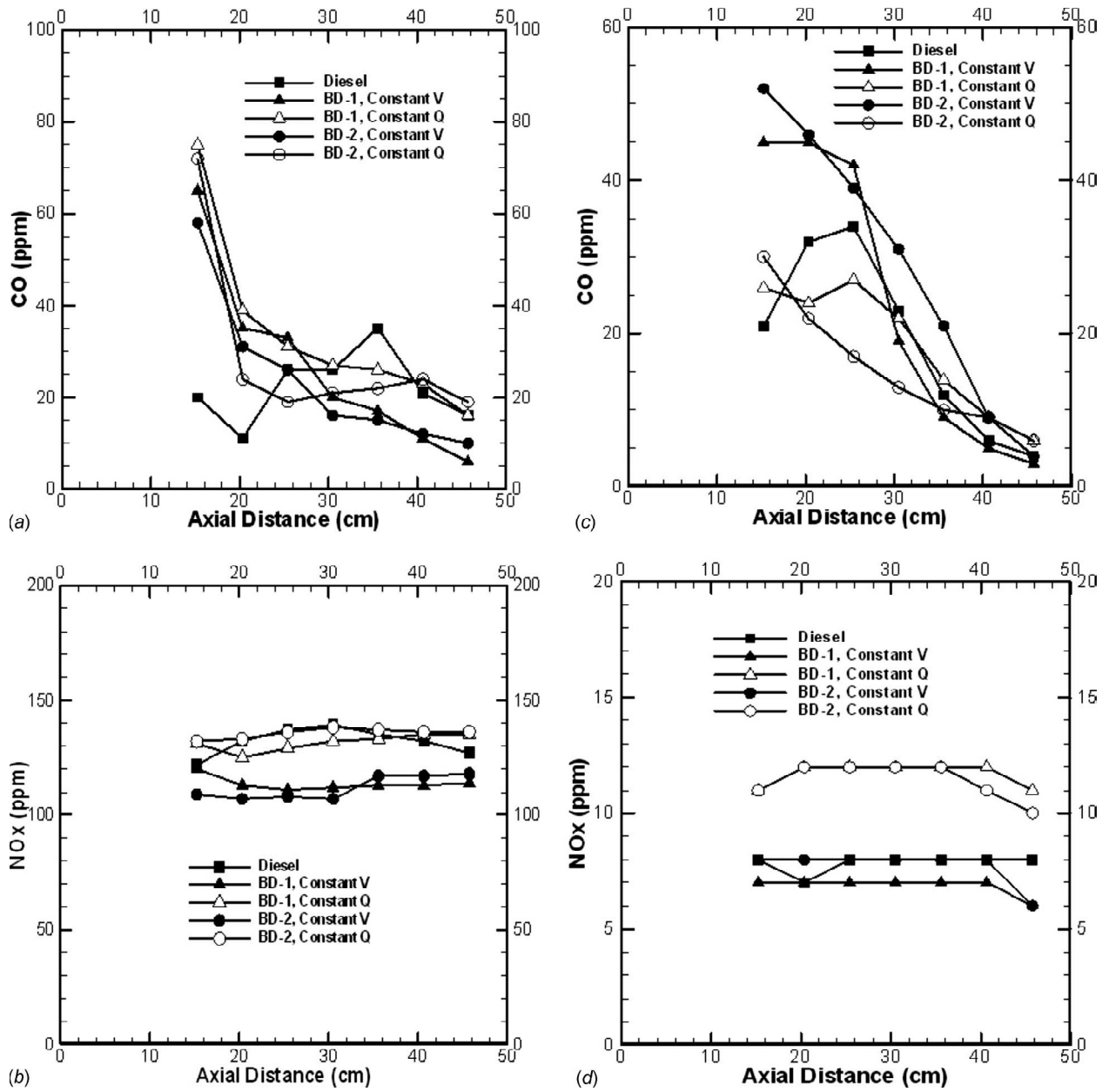


Figure 1.4 Axial profiles of CO and NO_x emissions at the combustor exit plane for diesel and biodiesel fuels: (a) and (b), profiles for 15% AA; (c) and (d), profiles for 25% AA

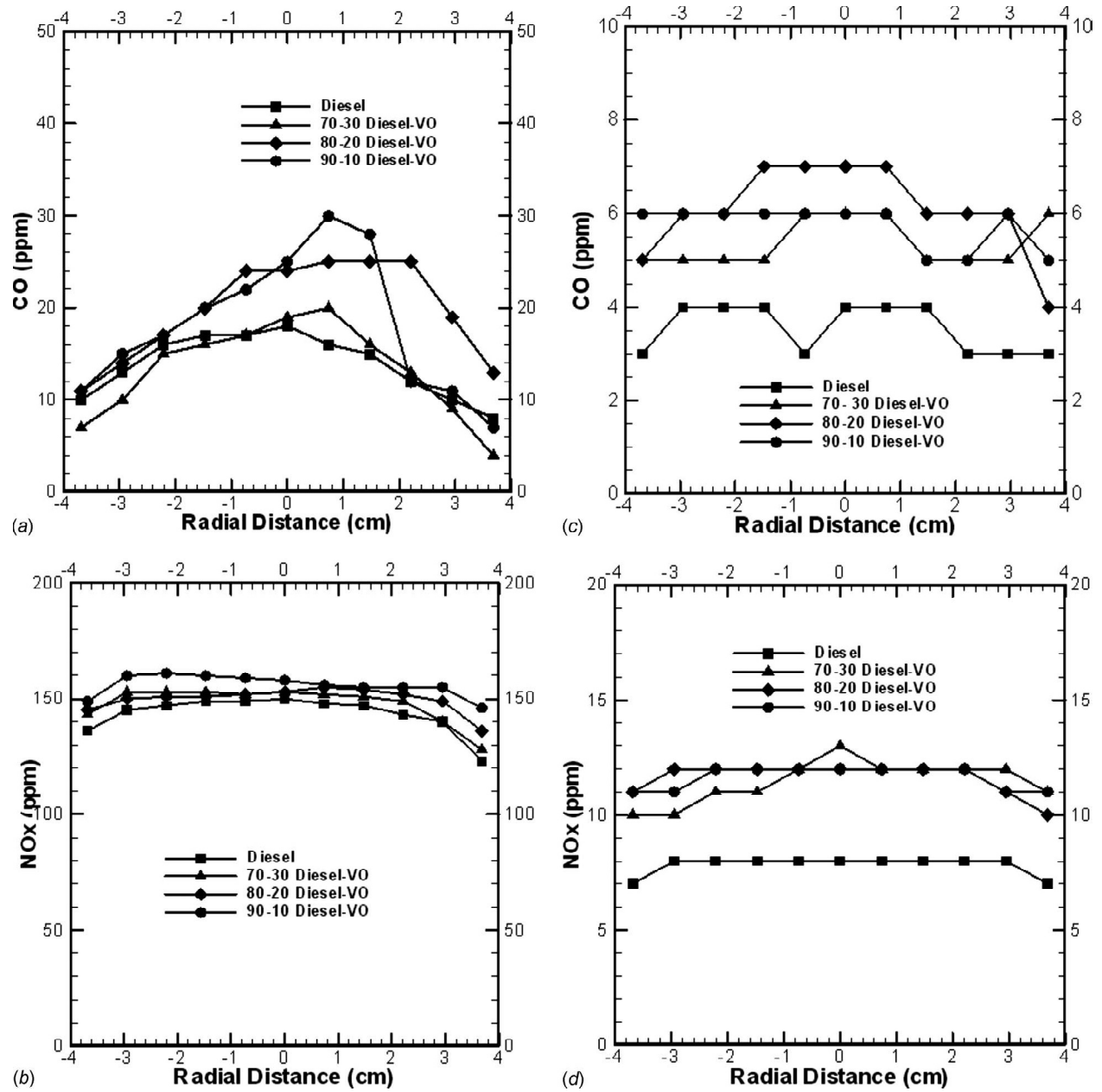


Figure 1.5 Radial profiles of CO and NO_x emissions at the combustor exit plane for diesel and diesel-VO blends: (a) and (b), profiles for 15% AA; (c) and (d), profiles for 25% AA

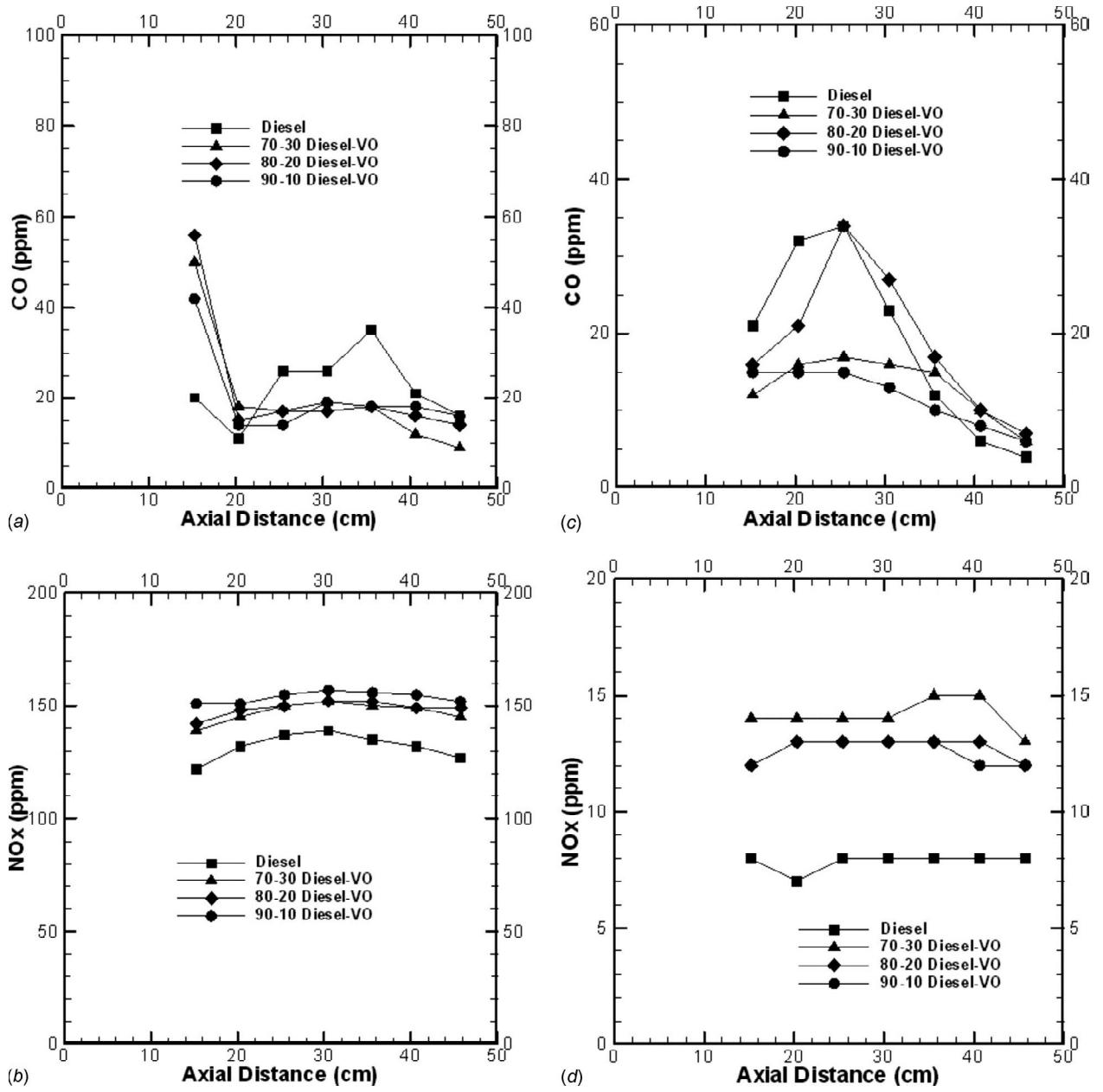


Figure 1.6 Axial profiles of CO and NO_x emissions at the combustor exit plane for diesel and diesel-VO blends: (a) and (b), profiles for 15% AA; (c) and (d), profiles for 25% AA

CHAPTER 2

BIO-OIL COMBUSTION USING FLOW BLURRING ATOMIZATION

2.1 Background

Liquid biofuels can serve as environmentally benign energy sources for stationary applications such as boilers, process burners, and power generating gas turbines (Moliere et al. 2007). Biodiesels are among the most widely studied biofuels because of their similarity to conventional diesel fuels (Graboski and McCormick 1998, Raghavan et al. 2009, Song et al. 2007, Bolszo and McDonell 2009, Wang et al. 2011, Pan et al. 2009, Li et al. 2011, Park et al. 2011). Biodiesels are produced by transesterification of source oils such as bio-oils or vegetable oil (VO). The transesterification process modifies the physical properties (e.g., kinematic viscosity) of bio-oil to produce biodiesel, which can readily replace diesel fuel in an application. Thus, existing fuel injectors, e.g., an air-blast (AB) atomizer, can be used to produce a fine spray, necessary to minimize emissions of nitric oxides (NO_x), carbon monoxide (CO), and particulate matter (PM). However, transesterification requires significant energy input and results in glycerol byproduct. With increasing biodiesel production, glycerol can become a significant waste stream, with its supply far exceeding the demand in the cosmetics, medical, and chemical industries. Thus, the present study is focused on efficient atomization for clean combustion of straight bio-oils to maximize economic and environmental benefits of liquid biofuels.

Table 2.1 compares thermo-physical properties for VO (fully-refined soybean oil in the present study) with those of soybean biodiesel, and No. 2 diesel. At room temperature, the kinematic viscosity of VO is almost 10 times that of biodiesel and over 13 times that of diesel.

VO also has significantly higher flash point temperature, auto-ignition temperature, and specific heat capacity compared to biodiesel and diesel. Relevant fuel properties were used to predict the Sauter Mean Diameter (SMD) for a plain-jet AB atomizer using the correlation of from Rizk and Lefebvre (1984). Atomizing air-to-liquid mass ratio (ALR) of 2.0 and 4.0 were considered for a fixed fuel flow rate of 12 milliliters per minute (mlpm). The predicted SMD for VO spray is two to three times larger than that for biodiesel or diesel. Large fuel droplets in a spray are likely to burn in non-premixed mode, which results in higher reaction zone temperatures and higher NO_x, CO, and PM emissions. Thus, direct combustion of VO in a combustor using an AB atomizer produces unacceptable levels of harmful emissions.

Table 2.1 Fuel Properties (Panchasara et al. 2009b)

| Property | VO | Biodiesel | Diesel |
|---|-----------------------------|-------------------------------------|-------------------------------------|
| Mol. Weight [kg/kmol] | 277.9 (Schwab et al 1998) | 291.5 | 142.2 |
| Density at 25 °C [kg/m ³] | 925.0 ± 8.6 | 880.0 ± 8.3 | 834.0 ± 9.2 |
| Viscosity at 25 °C [mm ² /sec] | 53.74 ± 0.22 | 5.61 ± 0.02 | 3.88 ± 0.02 |
| Surface Tension at 25 °C [mN/m] | 30.1 ± 0.6 | 31.1 ± 0.6 | 28.2 ± 0.6 |
| LHV [MJ/m ³] | 34,225 | 33,442 | 37,198 |
| Specific heat J/kgK | 2,269 (Santos et al. 2005) | 2,000 (Rakopoulos et al. 2007) | 1,750 (Diesel phys. prop. 2011) |
| Latent heat of evaporation [kJ/kg] | - | 200 (Qi and et al. 2010) | 250 (Qi and et al. 2010) |
| Flash point [°C] | 254 (Misra and Murthy 2010) | 139 (Alptekin and Canakci 2009) | 55 (Alptekin and Canakci 2009) |
| Boiling point [°C] | - | 338-380 (Alptekin and Canakci 2009) | 195-372 (Alptekin and Canakci 2009) |
| Auto-ignition temperature[°C] | 445 (Soybean oil MSDS 2011) | - | 315 (Demirbas 2006) |

| | | | |
|---|----|----|----|
| Predicted Droplet SMD [μm] | | | |
| ALR = 2 | 74 | 33 | 30 |
| ALR = 4 | 54 | 19 | 17 |
| (Rizk and Lefebvre 1984) | | | |

In an AB atomizer, the atomizing air interacts with the fuel jet to disintegrate fuel into droplets. A high relative velocity between the atomizing air and fuel flows results in shear layer instabilities that deform the fuel surface, first into ligaments and then droplets. Shear layer instabilities are suppressed by high kinematic viscosity of the fuel, which limits the ability of the AB injector to produce a spray with fine droplets. The effervescent atomization (EA) process can overcome these inherent limitations of AB atomizers. In the EA process, air is bubbled into the fuel line to form a bubbly two-phase mixture upstream of the atomizer. The two-phase mixture pressure decreases while exiting the atomizer, which causes air bubbles to expand and disintegrate the surrounding fuel mass into a spray with fine droplets. The EA process requires atomizing air at a high supply pressure and the two-phase mixture exhibits flow instabilities under some conditions (Sovani et al. 2001).

The present study employs “Flow-Blurring” (FB) atomization, first described by Gañán-Calvo (2005). Gañán-Calvo (2005) reported that for a set atomizing air flow rate, the FB injection concept created “five to fifty times” more fuel surface area than a plain-jet AB atomizer. The FB atomization is based on a simple geometric concept (illustrated in figure 2.1) to create fine sprays of liquids with a wide range of kinematic viscosity. A liquid tube of diameter “d” encircled by atomizing gas is located some distance away from a disc with an orifice of diameter “d”. As the distance “H” between the liquid tube exit and the disc orifice is varied, a dramatic change in the flow field takes place. For larger distances ($H/d \sim 1$), the liquid and gas interact similar to an AB atomizer. However, for shorter distances ($H/d \sim 0.25$), the

atomizing gas enters a short distance into the liquid tube where it is mixed intensely with the liquid. The resulting bubbly two-phase mixture exits the atomizer, where the gas phase rapidly expands to create fine liquid droplets. FB atomization is similar to the EA process, although the two-phase mixing in a FB atomizer occurs only at the tip of the liquid tube as dictated by the geometry (H/d).

Detailed phase Doppler particle analyzer (PDPA) measurements in water sprays have shown that the FB atomizer produces a spray with finer droplets compared to a commercial AB atomizer operated at identical liquid and gas flow rates (Simmons et al. 2009, Simmons and Agrawal 2010). FB atomizer also incurs a lower pressure drop penalty in the atomizing air line compared to the AB atomizer. Panchasara et al. (2009a) found that the CO and NO_x emissions in diesel and kerosene flames were 3 to 5 times lower with a FB atomizer as compared to an AB atomizer operated at the same fuel, atomizing air, and combustion air flow rates. The present study seeks to investigate FB atomization to cleanly combust high-viscosity, straight bio-oils. Experiments are performed using VO (soybean oil) as the test fuel and biodiesel and diesel as comparison fuels. Visual flame images, CO and NO_x emissions profiles, and pressure drop measurements are presented to characterize the combustion performance with FB atomization of VO, biodiesel, and diesel.

2.2 Experimental Setup

Experiments were conducted in a swirl-stabilized, atmospheric pressure combustor shown schematically in figure 2.2. Combustion air and methane (for startup) enter at the bottom of the setup and flow through the mixing section before entering a swirler followed by a 46 cm long quartz combustion chamber. Atomizing air also enters at the bottom of the setup, flows through a 1.6 cm (5/8 in.) OD concentric pipe within the mixing section, and then reaches the

atomizer assembly aligned with the dump plane of the combustion chamber. Liquid fuel enters the atomizer assembly through the side wall of the mixing chamber. In this study, a commercial atomizer (Delavan model 30609-2 AB) is modified to implement the FB atomization concept with $d = 1.5$ mm and $H = 0.35$ mm.

Air from an adjacent air compressor/storage-tank/dehumidification system is regulated to 4.1 bar (60 psi) before passing through traps and filters to remove remaining moisture. Next, the air flow is split into combustion air and atomizing air lines. Combustion air flow rate is controlled by a needle valve and measured by a laminar flow element (LFE) with an uncertainty of ± 5 slpm. Atomizing air flow rate is metered and controlled by Sierra Instruments Smart-Trak mass flow controller (Model C100L) with an uncertainty of ± 0.5 slpm. Methane is supplied from compressed storage tanks to start and preheat the system before completely switching to liquid fuel. Liquid fuel is delivered by a Cole-Parmer peristaltic metering pump (Model 7523-90) with an accuracy of ± 0.25 % of the reading.

Product gas is sampled continuously using a 7 mm ID quartz tube tapered down to a 1 mm ID tip to quench reactions inside the probe. The gas sample passes through an ice bath and water traps to remove moisture. A Nova model 376WP gas analyzer is used to measure CO, NO_x, oxygen (O₂), and carbon dioxide (CO₂) concentrations in the dry product sample. The measurement accuracy is ± 2 ppm for CO and NO_x emissions and ± 0.1 % for CO₂ and O₂ concentrations. Pressure is measured upstream in the fuel and atomizing air lines at locations shown in figure 2.2 using absolute pressure transducers (Omega model PX303).

The experiment is started by igniting the methane/air mixture, turning on the liquid fuel pump to supply the desired flow, and then gradually decreasing the methane flow rate until the system operates completely on the liquid fuel. Experiments were conducted for total air flow

rate (combustion air plus atomizing air) of 150 standard liters per minute (slpm). For the test sequence designated as “Constant V,” a fixed liquid fuel flow rate of 12 mlpm was used. It resulted in heat release rates (HRR) of 6.8 kW, 6.7 kW and 7.4 kW respectively for VO, biodiesel, and diesel. For the test sequence designated as “Constant Q,” flow rates of VO and biodiesel were adjusted to obtain a constant HRR of 7.4 kW for all three fuels. Experiments were conducted for ALR of 2.0 to 4.0, obtained by varying the atomizing air flow rate.

CHEMKIN software was used to compute equilibrium adiabatic flame temperatures (T_{ad}) for all fuels modeled with multiple components. A five component model presented by Schwab et al. (1998) was used for the VO. Soybean biodiesel composition was taken from gas chromatography-mass spectroscopy measurements of Panchasara et al. (2009b). The diesel fuel was represented by the four component model designated as DF1 by Glaude et al. (2010). Results in figure 2.3 show that the total air to fuel mass ratio required to obtain a given T_{ad} is nearly the same for VO and biodiesel, and it is higher for the diesel fuel presumably because of the absence of oxygen in the fuel. Different test conditions investigated in this study are identified by symbols in figure 2.3. Predicted T_{ad} for “constant Q” cases is nearly the same as expected; within 15 K of each other or 2090 K, 2060 K, and 2070 K, respectively, for VO, biodiesel, and diesel fuels. Predicted T_{ad} for “constant V” cases is 1990 K for VO, 1960 K for biodiesel, and 2070 K for diesel since the low heating value (LHV) of fuels is different. Further insight into the chemical behavior of different fuels could be gained through chemical kinetics analysis. However, detailed reaction mechanisms are available for diesel (Battin-Leclerc 2008) and biodiesel (Fisher et al. 2000, Herbinet et al. 2008 and 2010), but to the best of our knowledge, they do not exist for VO at this time.

2.3 Results and Discussion

2.3.1 Visual Flame Images

Figure 2.4 presents visual flame images to qualitatively assess the atomizer performance. For reference, figure 2.4(a) shows diesel flame images for ALRs of 2.0 to 4.0. The first image at ALR = 2.0, shows a blue-green region signifying C_2 radicals produced in fuel-rich combustion followed by a yellow-orange region indicative of soot formed by droplets burning in non-premixed mode (Turns 2000). Increasing the ALR eliminates burning in non-premixed mode such that a blue flame without soot remains at ALR > 2.5. The light blue color is typical of emissions from CH radicals produced in lean premixed (LPM) combustion (Turns 2000). Higher ALR increases the flow velocity, which shifts the flame in the downstream direction. Figure 2.4(b) shows images of biodiesel flames at the same heat release rate, i.e., “constant Q”. Flames for ALR = 2.0 and 2.5 show a blue LPM combustion region followed by an orange sooty non-premixed reaction zone. Again, as the ALR is increased, only a blue LPM flame remains. Figure 2.4(c) shows images of VO flames for the same heat release rate. Again, two distinct regions similar to diesel and biodiesel flames are observed for VO flame at ALR = 2.0. In this case, VO droplets also impinged on the quartz combustor to create slight soot buildup. However, no charring or soot buildup was observed for ALR > 2.0, whereby images for all three fuels were similar. Figure 2.4 indicates that the VO flame produced by the FB injector is qualitatively similar to biodiesel or diesel flames. Flame images in figure 2.4 also suggest that ALR > 2.0 could result in clean combustion of all three fuels.

2.3.2 Emissions Measurements

Figure 2.5 compares the radial profiles of CO concentration at the combustor exit plane for flames of different fuels at ALR = 2.0. CO concentrations for VO and diesel flames are

similar, and generally within 10 ppm. CO concentrations for the two VO flames vary between 5 and 12 ppm, with slightly higher values obtained for the “constant Q” case because of the higher flame temperature. Radial asymmetry in the profile for the diesel flame is consistent with the image in figure 2.4. Biodiesel flames result in lowest CO emissions, between 2 and 3 ppm. However, considering the instrument uncertainty of ± 2 ppm, CO emissions from flames of different fuels are similar even for a relatively low ALR = 2.0.

Figure 2.6 shows the radial profiles of NO_x emissions for the three fuels at ALR = 2.0. NO_x emissions are highest for the diesel flame (90 to 95 ppm), lowest for the biodiesel flame (20 to 25 ppm) and in-between these limits for the VO flame (60 to 75 ppm). In spite of lower adiabatic flame temperature, the VO flame for “constant V” case produces higher NO_x emissions compared to the “constant Q” case. This result is attributed to poor atomization at the low ALR of 2.0, especially for the higher fuel flow rate of “constant Q” case. In this case, more VO droplets were found to impinge on the quartz enclosure, suggesting that a portion of the fuel remained unburned to decrease the effective overall equivalence ratio.

For all fuels, the CO emissions decreased with increasing ALR. Figure 2.7 shows nearly uniform CO emissions between 2 and 4 ppm for all flames at ALR = 3.0. Figure 2.8 shows that an increase in ALR from 2.0 to 3.0 also decreased NO_x emissions. NO_x emissions from the diesel flame decreased from 95 ppm at ALR = 2.0 to about 15 ppm at ALR = 3.0. Similarly, NO_x emissions from biodiesel flame decreased from 20 ppm at ALR = 2.0 to about 6 and 8 ppm at ALR = 3.0, respectively, for “constant V” and “constant Q” cases. NO_x emissions from VO flames were around 15 and 20 ppm, respectively, for “constant V” and “constant Q” cases. The drastic reduction in NO_x levels is attributed to more efficient atomization at a higher ALR, resulting in smaller droplets which evaporate faster to burn in the premixed mode. Figure 2.9

shows CO emissions between 2 and 5 ppm for all five cases at ALR = 4.0. No meaningful difference from the results of ALR = 3.0 is observed since CO emissions for all cases are very low and within the measurement uncertainty of the gas analyzer. Finally, figure 2.10 shows radial profiles of NO_x emissions for ALR = 4.0. In this case, NO_x levels decrease to around 10 ppm for the diesel flame, between 7 and 11 for VO flames, and around 5 ppm for biodiesel flames. Thus, NO_x emissions from diesel and VO flames are similar, but slightly higher than those from biodiesel flames.

2.3.3 Comparison of FB and AB Atomization

Figure 2.11 shows a comparison of CO emissions from the FB injector (ALR = 2.0) with results from an AB injector published by Panchasara et al. (2009b). The AB study was conducted with different ALRs which are noted in the figure legend. It is quite substantial that the FB injector produces lower CO emissions with all three fuels including highly viscous VO, all while operating at a lower ALR. Figure 2.12 shows the same comparison between AB and FB injectors with NO_x emissions. Again while operating at a lower ALR, the FB injector creates sprays with much lower NO_x emissions, indicating much better atomization. From both of these plots it should be noted that the FB injector operating with VO produces lower emissions than the AB injector operating with biodiesel. This clearly shows that the passive FB technology could be implemented in combustion systems with bio-oil and have better results than the transesterified bio-oil (biodiesel), meaning substantial energy and fuel cost savings.

2.3.4 Pressure Drop Measurements

Emissions measurements substantiate the ability of the FB atomizer to efficiently atomize fuels with a wide range of kinematic viscosities and thermo-physical properties. Power input requirement to achieve this superior performance is investigated next by measuring the pressure

drop in the fuel and atomizing air lines. Figure 2.13 shows that the pressure drop in the atomizing air line increases with increasing atomizing air flow rate, as expected. Atomizing air pressure drop varies from approximately 1.0 to 2.8 bar respectively, for atomizing air flow rates of 16.7 to 33.4 slpm. Interestingly, atomizing air pressure drop is independent of the fuel or the fuel flow rate within the narrow range of 12 to 13 mlpm in the present experiments. Figure 2.13 also shows that the pressure drop in the fuel line increases with increasing atomizing air flow rate. Fuel line pressure drop is the same for different fuels and flow rates (constant V or constant Q). Fuel line pressure drop is also independent of the fuel because most of the pressure drop occurs in the two-phase region near the atomizer exit. Note that the frictional loss in the fuel line is much smaller for the FB atomizer compared to an AB atomizer because of the difference in fuel line diameter (1.5 mm for FB atomizer versus 0.3 mm for AB atomizer).

2.4 Conclusions

In this study, a FB atomizer has been used to achieve clean combustion of straight bio-oil (soybean oil). Biodiesel and diesel flames were also investigated for comparison. Visual images show similar flame structure of all three fuels for ALR > 2.5. CO emissions for all fuels were statistically similar for ALR = 3.0 and higher. For smaller ALR = 2.0, CO emissions from VO and diesel flames were similar, though slightly higher than those from biodiesel flames. NO_x emissions from flames of all fuels were affected significantly by the ALR. For higher ALR, NO_x emissions for VO and diesel flames were similar, while biodiesel flames resulted in the lowest NO_x emissions. Comparisons showed that the FB injector produces lower emissions with VO than the AB injector operating with biodiesel, suggesting that transesterification might be unnecessary in some circumstances. Measurements show that the pressure drop in the atomizing air line and fuel line is independent of the fuel. This study demonstrates that FB atomization can

facilitate low-emission combustion of a range of liquid fuels, including high-viscosity straight bio-oils. Thus, source oil transesterification could be eliminated for some applications, saving cost, energy, and time, while widening the market for liquid biofuels.

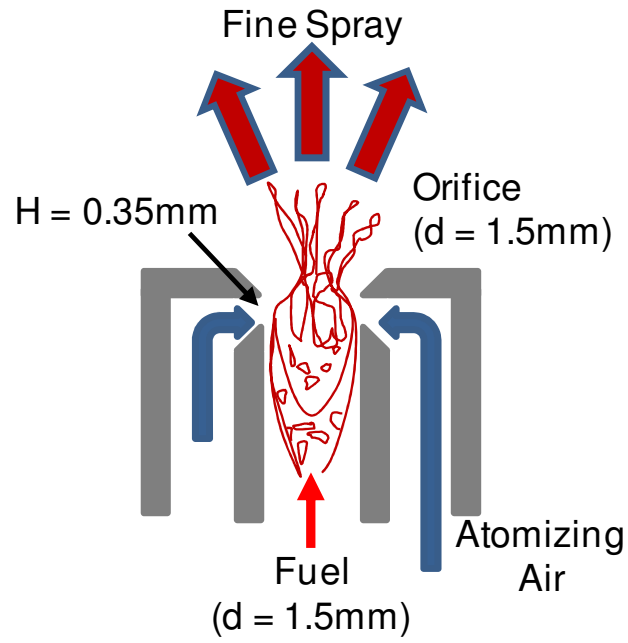


Figure 2.1 Flow Blurring (FB) atomization concept

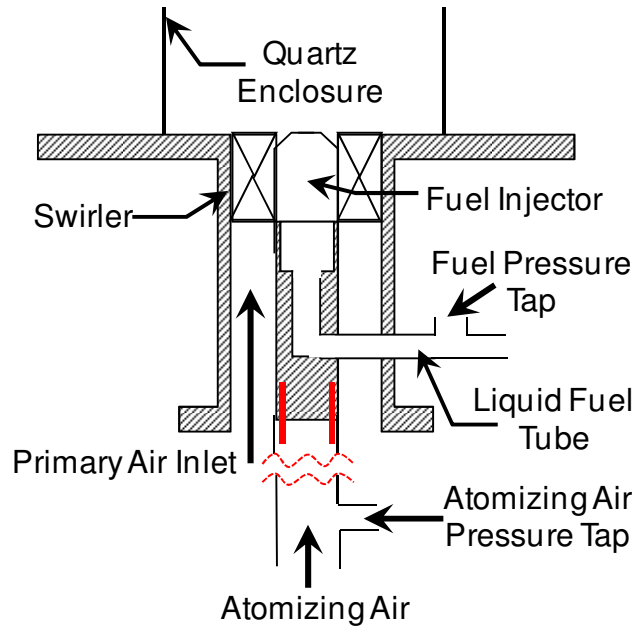


Figure 2.2 Experimental setup

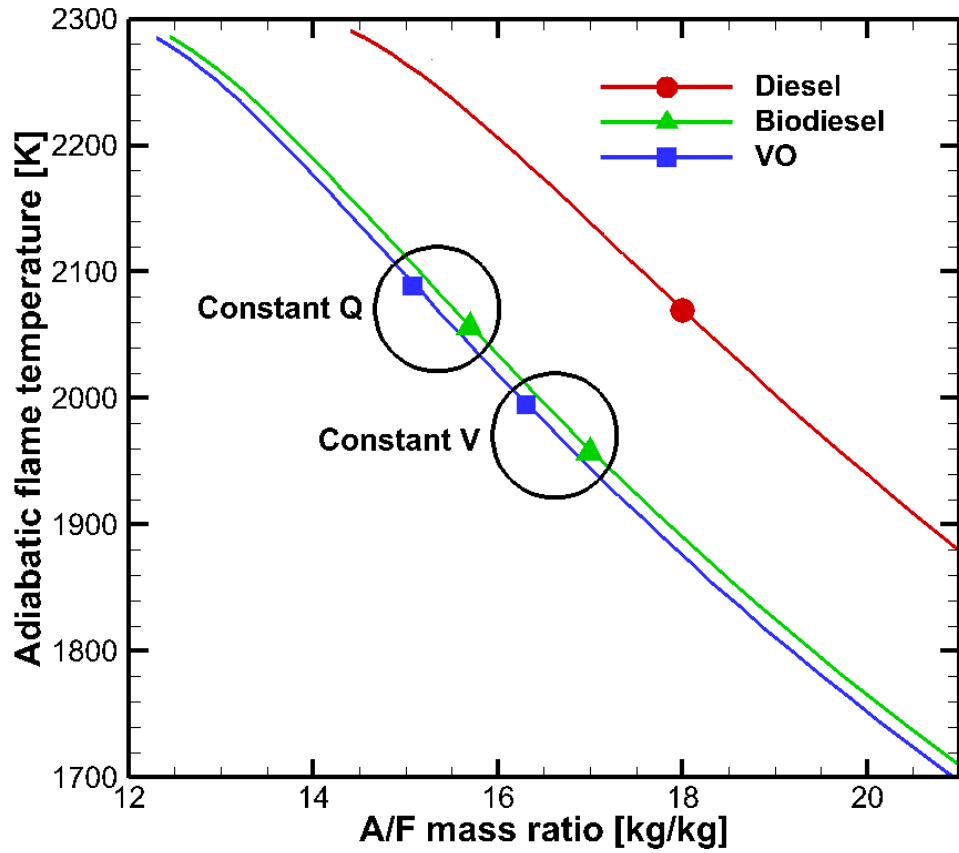


Figure 2.3 Predicted adiabatic flame temperatures

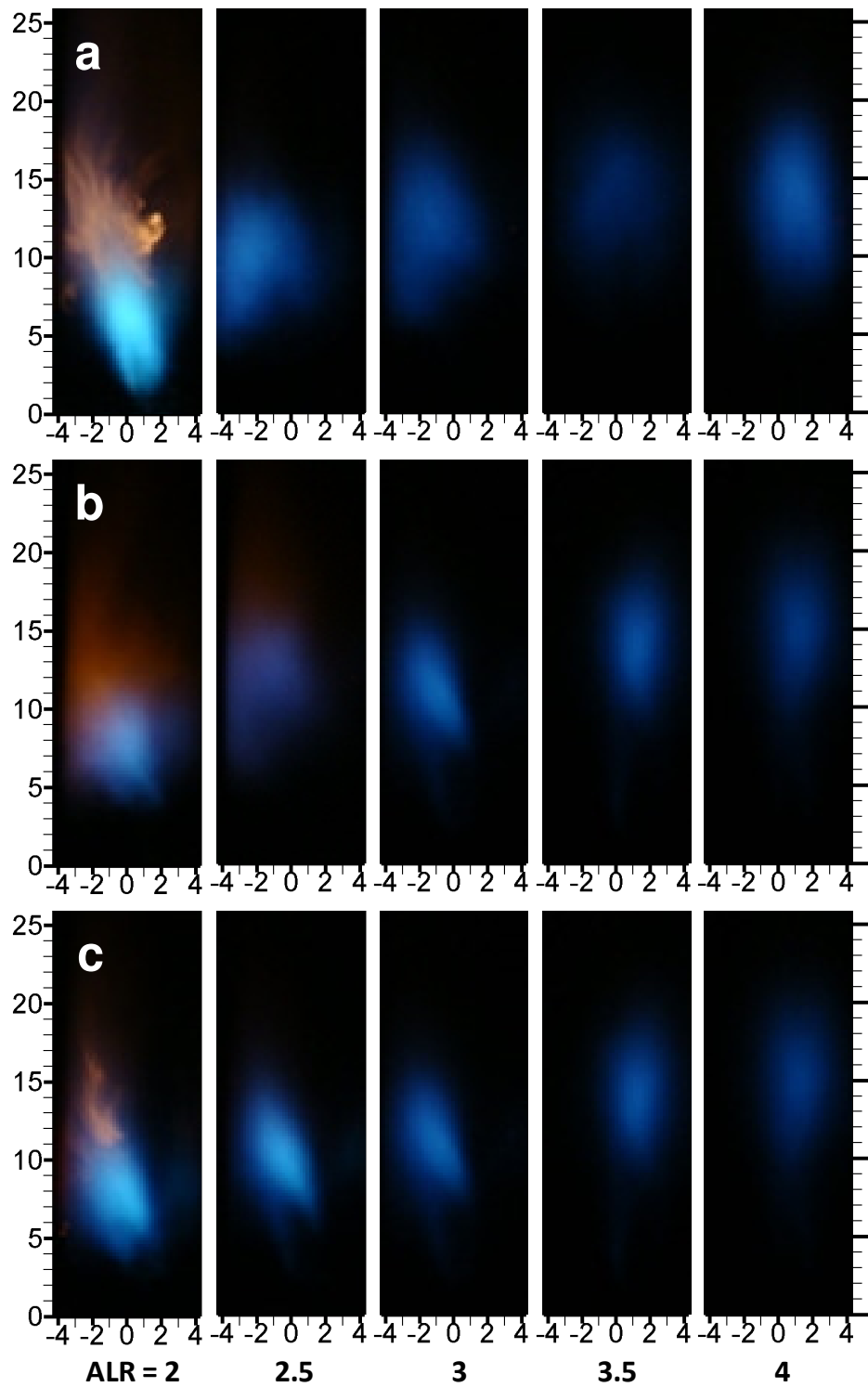


Figure 2.4 Flame images at constant Q (a) diesel, b) biodiesel, (c) VO (scale in cm)

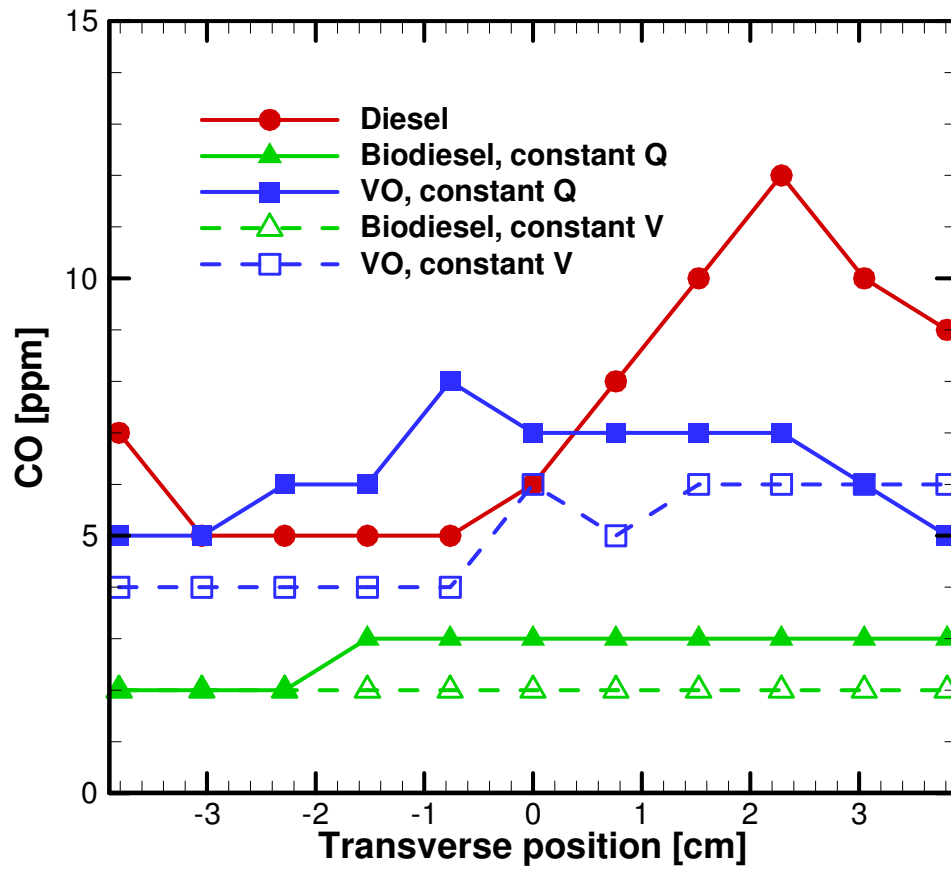


Figure 2.5 CO emissions at combustor exit plane, ALR = 2.0

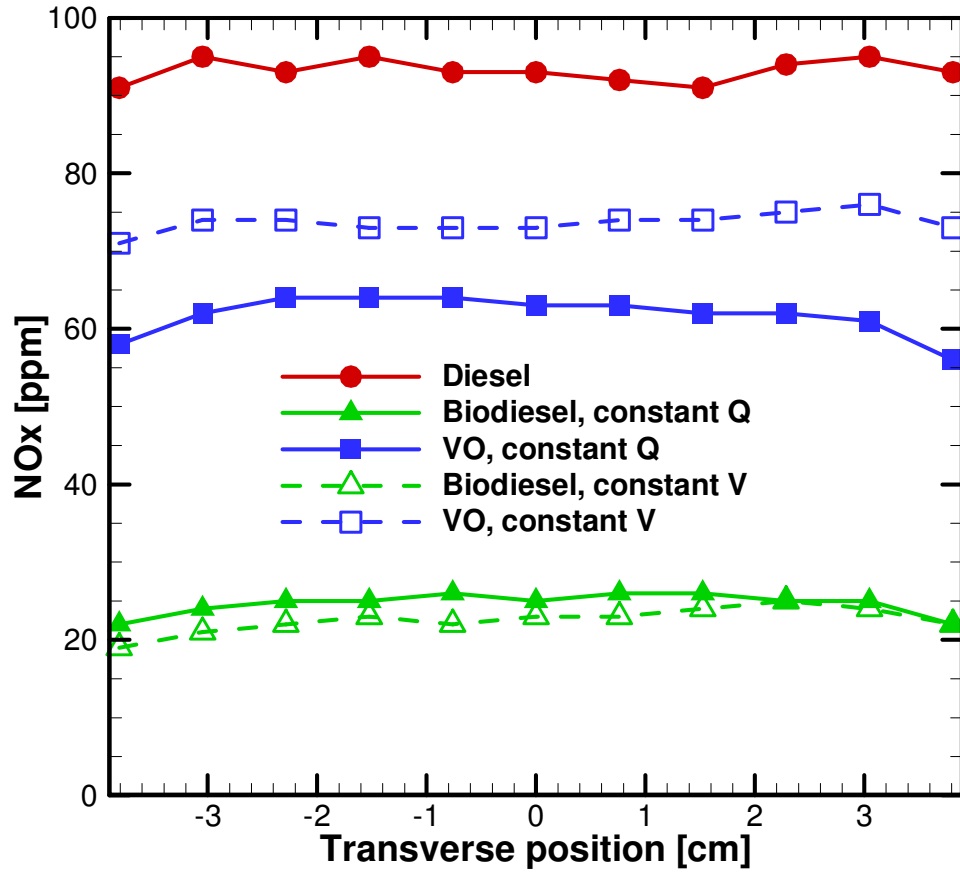


Figure 2.6 NO_x emissions at combustor exit plane, ALR = 2.0

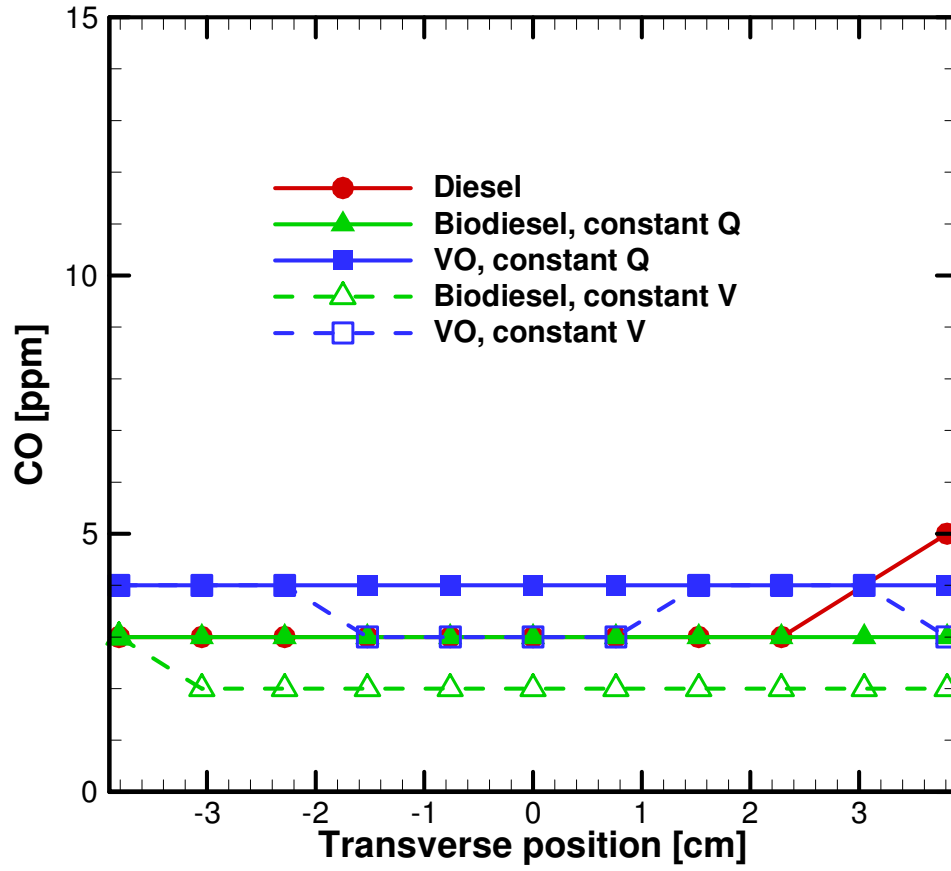


Figure 2.7 CO emissions at combustor exit plane, ALR = 3.0

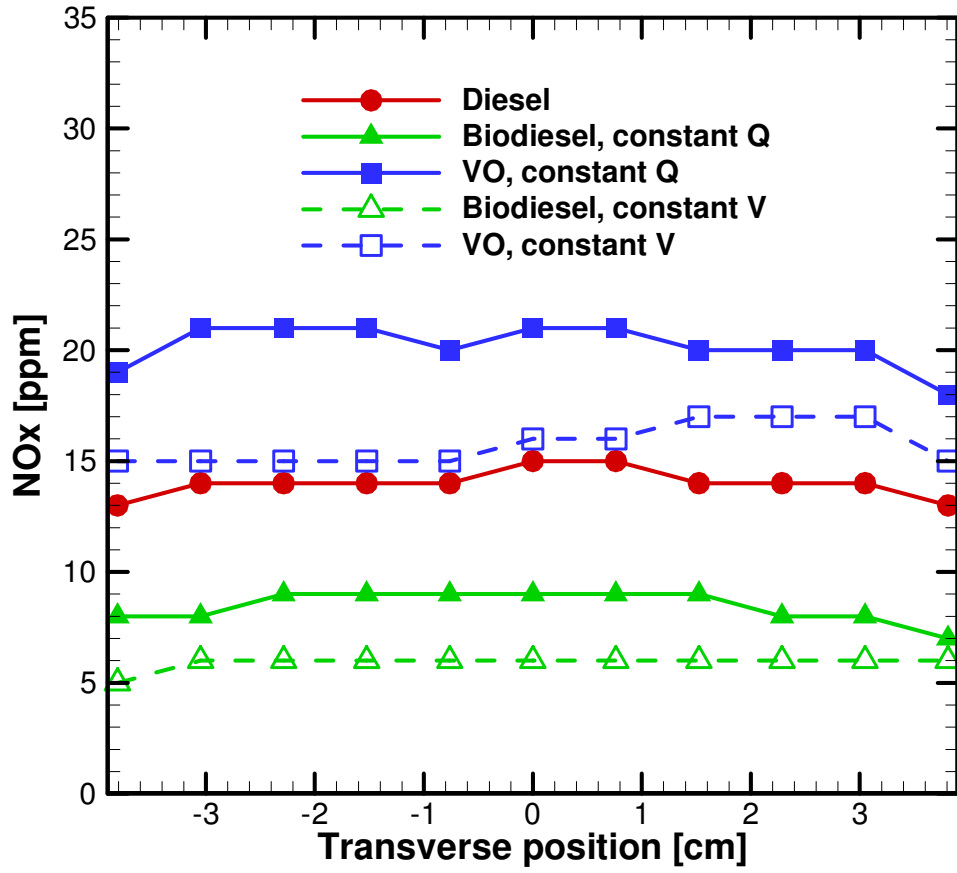


Figure 2.8 NO_x emissions at combustor exit plane, ALR = 3.0

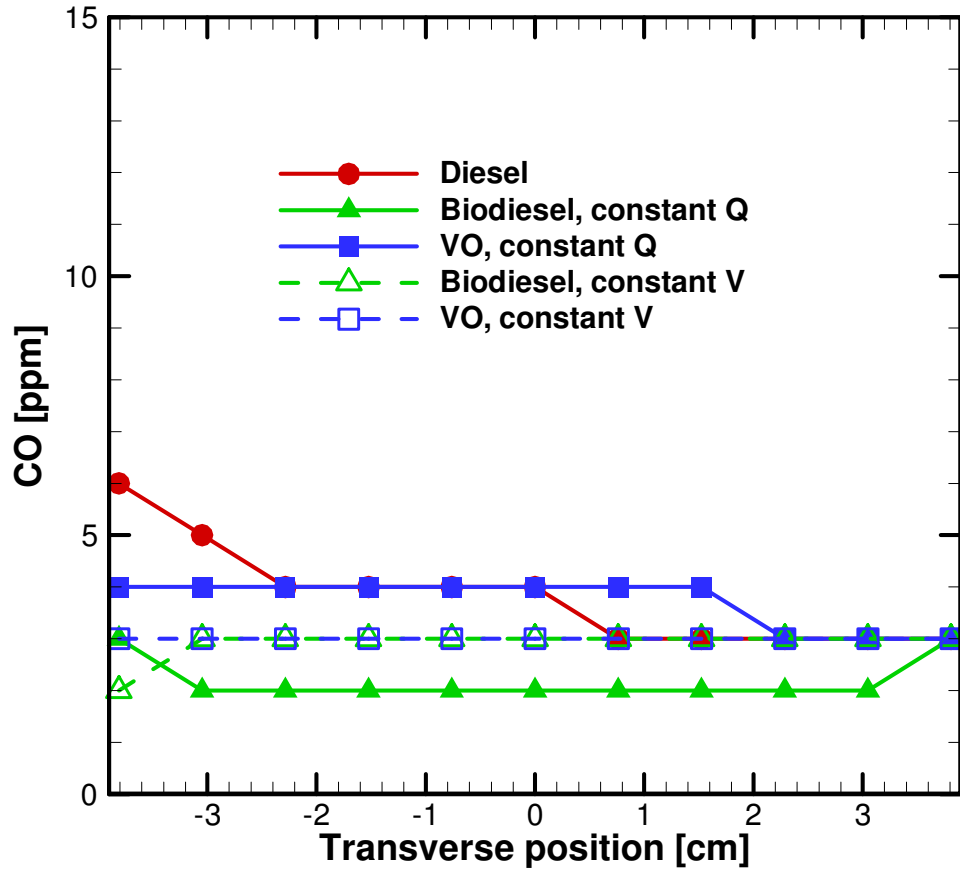


Figure 2.9 CO emissions at combustor exit plane, ALR = 4.0

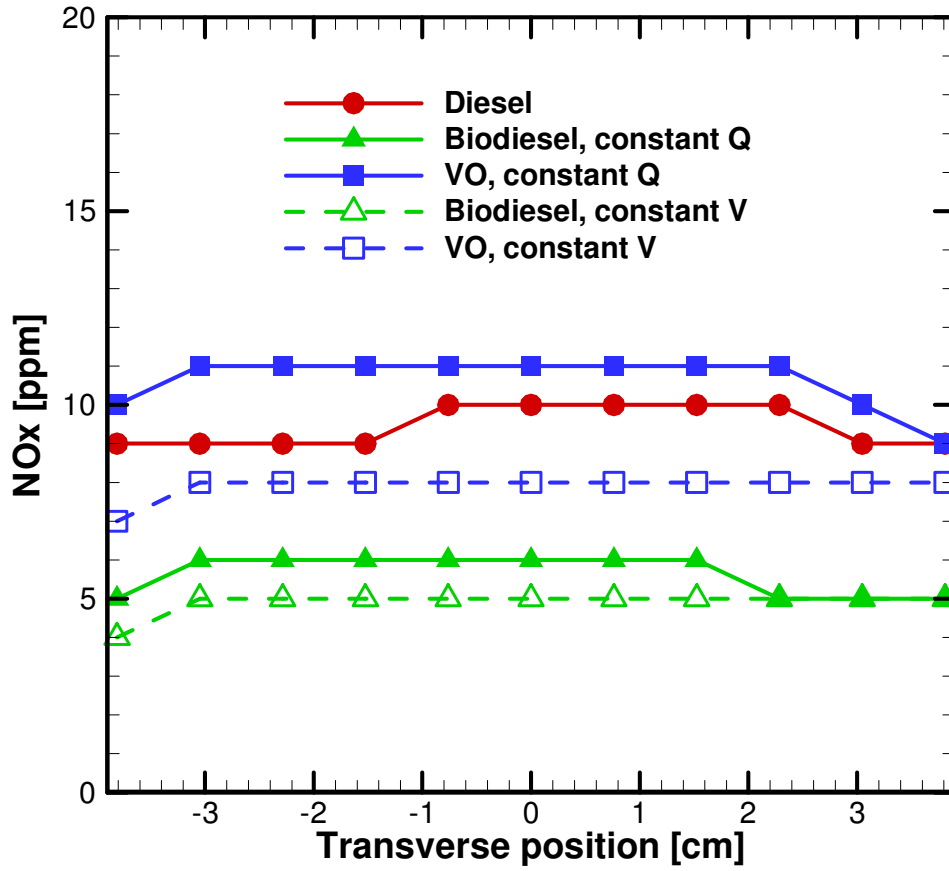


Figure 2.10 NO_x emissions at combustor exit plane, ALR = 4.0

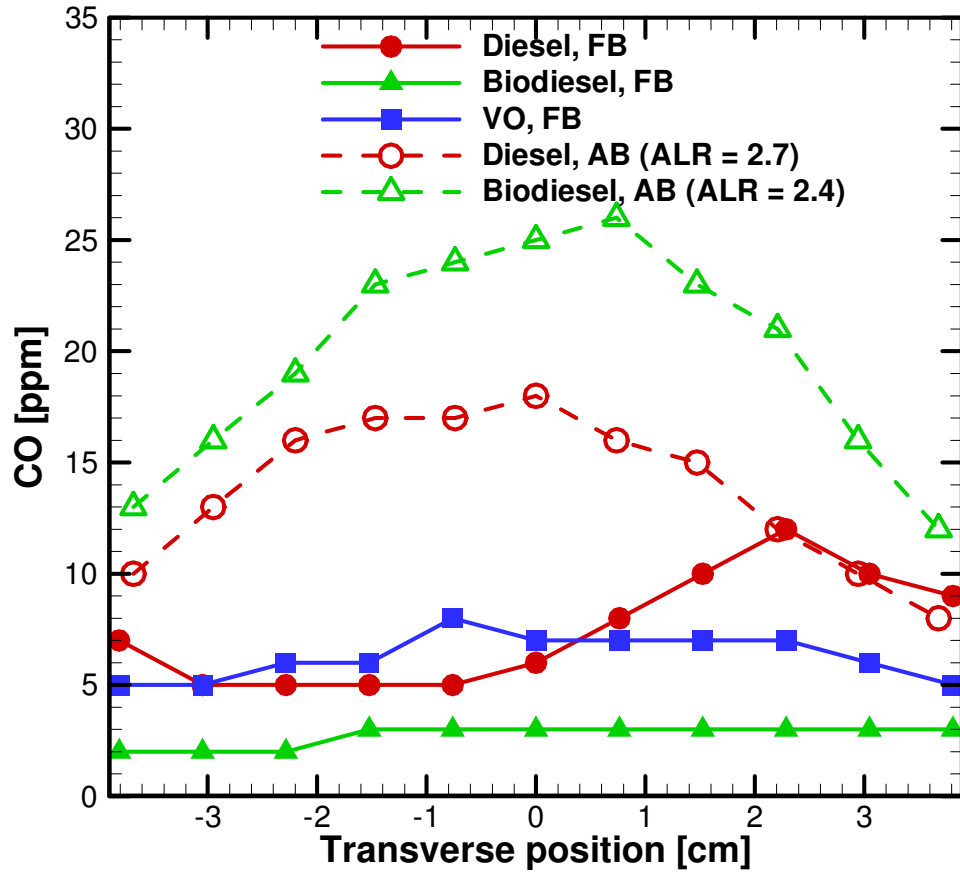


Figure 2.11 Comparison of CO emissions between FB and AB injectors, ALR = 2.0

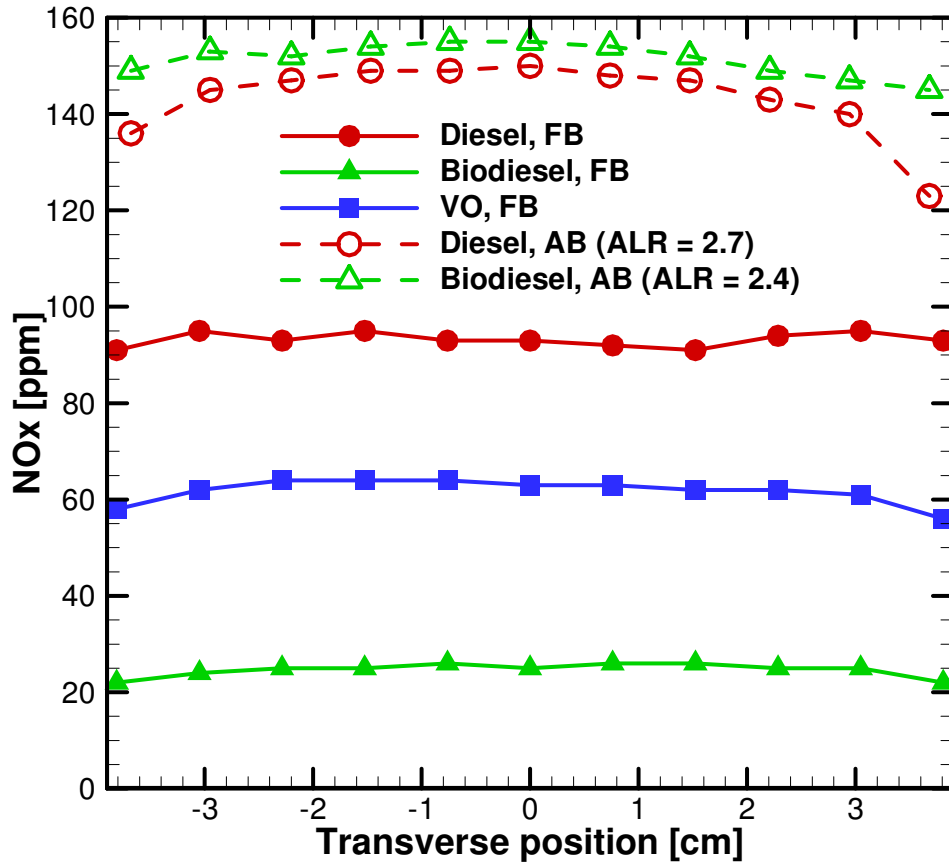


Figure 2.12 Comparison of NO_x emissions between FB and AB injectors, ALR = 2.0

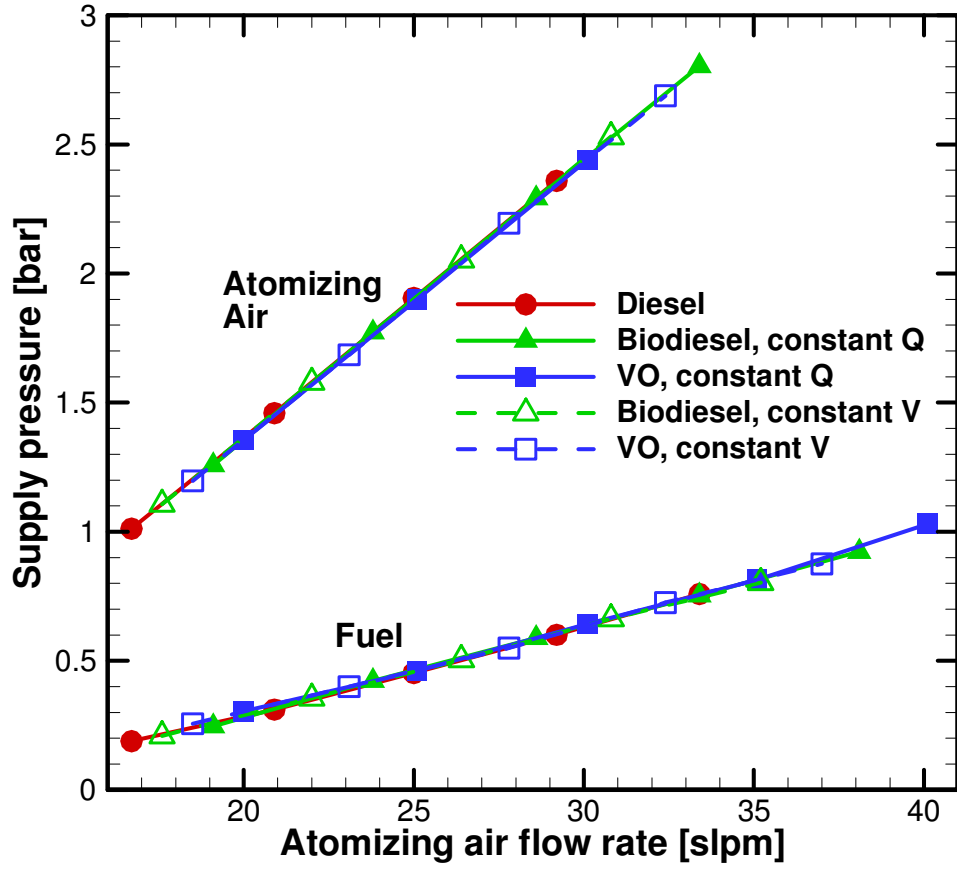


Figure 2.13 Fuel and atomizing air supply pressure

CHAPTER 3

GLYCEROL COMBUSTION USING FLOW-BLURRING ATOMIZATION

3.1 Background

Glycerol is a byproduct of the biodiesel production process, called transesterification. Glycerol is produced at a roughly 10% volumetric rate to that of biodiesel. The National Biodiesel Board has estimated that approximately 498 million gallons of biodiesel will be produced between 2006 and 2015, resulting in large quantities of glycerol [2006]. While there are many uses for glycerol, its production can outstrip demand. In recent years, large biodiesel production has saturated the glycerol market. Therefore, biodiesel companies have incurred a cost penalty to dispose of waste glycerol at times. But glycerol does have energy content that could be recovered on site. When biodiesel production again ramps up, glycerol can prove to be a valuable energy source to biodiesel producers.

Table 3.1 lists physical and chemical properties of glycerol and standard no. 2 diesel [Panchasara et al, 2009b; CRC Handbook, 2010; #2 Diesel MSDS, 2011; Glycerol MSDS, 2011; Sahin and Gurgum, 2007]. The lower heating value of glycerol is only 36% of that of diesel on a mass basis. In comparison to diesel, glycerol has a kinematic viscosity approximately 190 times greater than and over twice the surface tension. Both of these properties affect the instabilities that breakup the fuel supplied by the fuel injector. The glycerol also has higher enthalpy of vaporization and higher vaporization and auto-ignition temperatures than diesel. Thus, significant energy from the flame must be convected or radiated upstream to ensure proper fuel vaporization and low-emission combustion.

Table 3.1 Chemical and physical properties of fuels

| | # 2 Diesel | Glycerol |
|---|-------------|---|
| Chemical Formula | varies | C ₃ H ₅ (OH) ₃ |
| Mol. Weight [kg/kmol] | 142.2 | 92.1 |
| Density @ 25°C [kg/m ³] | 834 | 1260 |
| Kinematic Viscosity @ 25°C [mm ² /s] | 3.88 | 741 |
| Surface Tension @ 25°C (mN/m) | 28.2 | 62.5 |
| Lower Heating Value [MJ/kg] /[MJ/m ³] | 44.6/37,200 | 16.2/20,400 |
| Enthalpy of Vaporization [kJ/kg] | 522 | 662 |
| Auto-Ignition Temperature [°C] | 260 | 370 |
| Vaporization Temperature [°C] | 160-370 | 290 |

Previous studies have shown that glycerol combustion can be achieved successfully with a proper experimental setup. Bohon et al reported on glycerol combustion using insulated 7 and 82 kW combustion systems [2011]. Results showed single digit NO_x and undetectable CO (meaning less than 0.1%) for pure glycerol in the 7 kW system, while the 82 kW system produced much higher NO_x (up to 235 ppm at 0% O₂ for raw glycerol samples). While the 7 kW system operated with unheated glycerol, the 82 kW system utilized an in-barrel heater to preheat the raw glycerol [Bohon et al. 2011]. The present study will demonstrate a simple practical system for the combustion of glycerol based on a novel fuel injection technique that ensures fine sprays and therefore clean combustion without the need for any fuel preheating.

Traditional land based combustion systems generally use Air-Blast (AB) atomization. The AB technique utilizes air and fuel streams interacting at high relative velocity. This high

relative velocity creates shear stresses that cause the growth of instabilities in the fuel stream surface. The instabilities lead to the deformation of the fuel stream surface and cause it to break up into ligaments and droplets. As this mechanism depends highly on the deformation of the fuel surface, fuel properties are important for effective atomization by the AB injector. High kinematic viscosity and/or surface tension tend to suppress flow instabilities. Thus, AB atomization cannot be used with fuels such as unprocessed glycerol. Effervescent atomization (EA) overcomes these limitations of the AB technique. In the EA concept, fuel and air are mixed upstream of the injector orifice to form a bubbly two-phase flow. The flow exits the injector orifice, with a rapid decrease in pressure, causing the gas phase to expand. The expansion causes the gas bubbles to burst and disintegrate the surrounding fuel to create a fine fuel spray. The EA concept has not been widely applied because of its inherent drawbacks, such as two-phase flow instabilities under certain conditions [Sovani et al, 2001].

Flow-Blurring (FB) atomization is an efficient fuel injection concept, first described in the literature by Gañán-Calvo [2005]. The FB technique relies on a simple geometry to create a robust atomization method. The FB concept is illustrated in figure 3.1. A fuel tube (of diameter d) surrounded by atomizing air is kept a distance (H) from an exit orifice of the same diameter (d). As the distance H is varied, a dramatic change occurs in the flow field. For large distances ($H \sim d$), the atomizing air flows around the fuel jet and both exit the orifice, similar to AB injection. As the fuel tube is moved closer ($H \sim 0.25d$), atomizing air flows a short distance up into the fuel tube and mixes intensely with the fuel. This two-phase flow undergoes a negative pressure gradient while exiting the orifice. Thus, the fuel atomization mechanism is similar to the EA process. However, fuel-air mixing occurs only at the fuel tip and is solely based on the FB injector's spacing.

Gañán-Calvo first reported that the FB outperformed the AB concept by creating “five to fifty times” more droplet surface area than a plain-jet AB atomizer [2005]. Another study compared water sprays from FB and AB injectors and concluded that the FB injector produced smaller diameter droplets and incurred a smaller pressure drop in the atomizing air line compared to the AB concept [Simmons and Agrawal, 2011]. Studies have also investigated the effect of the FB concept on combustion systems. Results in diesel and kerosene flames showed that the FB injector reduced carbon monoxide (CO) emissions and nitrogen oxides (NO_x) emissions by three to five times, as compared to an AB atomizer operating at the same conditions [Panchasara et al, 2009a]. Another study has shown that the FB injector is effective for the atomization and combustion of VO [Simmons et al, 2008]. The present study seeks to expand the FB injector’s application to atomize and combust glycerol in a simple reproducible system.

3.2 Experimental Setup

A diagram of the fuel flexible combustion system used in this study can be seen in figure 3.2. Air is split into primary air for combustion and atomizing air for fuel breakup. Primary air enters through the bottom of the combustion system and mixes with methane before passing through a swirler and entering the combustion chamber. The combustor was insulated in some cases to increase thermal feedback to the incoming glycerol. An explanation of the insulation thickness calculations is given in appendix E. Atomizing air travels through a small pipe in the center of the system before entering the injector assembly located in the center of the swirler. Liquid fuel enters the injector assembly through the side of the system. The FB injector used in this study utilized the external hardware of a commercial AB injector (Delevan model 30609-2). The fuel tube and exit orifice diameters were increased to 1.5 mm and an approximately 0.35 mm spacer was placed between the fuel tube and exit orifice to ensure FB atomization.

Methane is supplied from adjacent pressurized cylinders and its flow is metered using Sierra Instruments Smart-Trak mass flow controllers with uncertainty of ± 0.4 slpm. Glycerol fuel is supplied and metered using a Cole-Parmer peristaltic pump with an uncertainty of $\pm 0.25\%$ of the reading. Air is supplied by an adjacent compressor and is filtered to remove moisture before being regulated to a pressure of approximately 60 psi (4.14 bar). Primary air is controlled with a needle valve and is metered by a laminar flow element with an uncertainty of ± 5 standard liters per minute (slpm). Atomizing air flow is set by a Sierra Instruments 810C mass flow controller with an uncertainty of ± 0.5 slpm. Pressure measurements are taken using Omega PX303 pressure transducers at the locations shown in Figure 3.2. Product gases were sampled continuously at the combustor exit plane (45.7 cm from injector exit) and passed through filters and an ice bath to remove any moisture. Emissions measurements were taken using a Nova emissions system with an uncertainty of ± 2 ppm.

Temperature measurements were taken on the inside and outside of the insulation at axial location X (axial distance from the dump plane) = 2.5, 7.6, and 30.5 cm to calculate heat loss through the combustor walls. Type B thermocouples were used on the inside of the insulation due to their high temperature range, while type K thermocouples were used to measure the surface temperatures of the insulation. Each of these pairs of temperature measurements (compiled in Table 3.2) was used to calculate local heat flux through the insulation. The total heat loss was estimated by dividing the combustor into three zones, each with a constant heat flux measured by thermocouples located at mid-length. Thus, zone 1 extended from X = 0 to 5.05 cm, and zones 2 and 3 were 14 cm and 26.7 cm in length, respectively. The total heat loss is the sum of heat loss in the three zones.

Table 3.2 Temperature measurements from insulated combustor

| Conditions | | | Inner insulation temp [K] | | | Outer insulation temp [K] | | |
|------------|---------|------|---------------------------|-------|--------|---------------------------|-------|--------|
| Fuel | HRR[kW] | ALR | 2.5cm | 7.6cm | 30.5cm | 2.5cm | 7.6cm | 30.5cm |
| G00 | 7.0 | 0.95 | 622 | 716 | 1137 | 67 | 81 | 252 |
| G00 | 7.0 | 1.04 | 847 | 904 | 1166 | 74 | 91 | 261 |
| G00 | 7.0 | 1.13 | 881 | 1001 | 1182 | 80 | 94 | 267 |
| G00 | 7.0 | 1.22 | 891 | 1046 | 1200 | 82 | 101 | 284 |
| G00 | 7.0 | 1.32 | 881 | 1054 | 1187 | 75 | 91 | 260 |
| G00 | 7.0 | 1.41 | 880 | 1057 | 1189 | 77 | 94 | 264 |
| G00 | 7.0 | 1.50 | 868 | 1050 | 1175 | 77 | 90 | 257 |
| G00 | 7.0 | 1.59 | 861 | 1050 | 1178 | 75 | 91 | 260 |
| G00 | 7.0 | 1.68 | 861 | 1050 | 1178 | 76 | 89 | 259 |
| G00 | 4.0 | 1.13 | 867 | 1019 | 1124 | 72.2 | 81.8 | 220 |
| G00 | 7.0 | 1.13 | 861 | 980 | 1154 | 73 | 86 | 251 |
| G00 | 11.6 | 1.13 | 414 | 636 | 1036 | 56 | 66 | 231 |
| G100 | 7.0 | - | 861 | 980 | 1154 | 73 | 86 | 251 |
| G90 | 7.0 | - | 920 | 1056 | 1204 | 72.4 | 82.9 | 228 |
| G90-100 | 7.0 | - | 844 | 953 | 1132 | 63 | 75 | 213 |
| G50 | 7.0 | - | 989 | 1130 | 1227 | 69.5 | 84.5 | 186.2 |
| G50-27 | 7.0 | - | 935 | 1083 | 1187 | 75 | 90.5 | 207 |
| G50-55 | 7.0 | - | 876 | 1025 | 1138 | 67.6 | 80.3 | 181 |

Experiments were started by igniting a methane/air flame and then gradually increasing glycerol flow rate while decreasing methane flow rate until the desired conditions are met. Experiments were performed under several sets of operating conditions. First, un-insulated glycerol and methane flames were investigated. Methane was used to enhance combustion of glycerol and also to demonstrate the dual fuel capabilities of the burner. After these initial experiments, the combustion chamber was insulated for the remaining tests. Next, the air to liquid mass ratio (ALR) through the FB injector was varied. For this set of experiments, the total air flow rate and glycerol flow rate were kept constant, respectively at 150 slpm and 21 mlpm. It resulted in an overall equivalence ratio (Φ) of 0.77 and heat release rate (HRR) of 7 kW. Next, ALR = 1.13 and $\Phi = 0.77$ were kept constant, while the HRR was changed by varying the total air and glycerol flow rates. Finally, the effect of co-firing glycerol with methane was investigated. HRR was kept at 7 kW, total air flow rate was kept at 150 slpm, and the atomizing gas flow rate was fixed at 30 g/min. The percentage of total heat release rate from glycerol was varied, with methane flow split between atomizing air and combustion air. G100, G90, and G50 respectively represent 100%, 90%, and 50% of the total heat release rate from glycerol, with the balance from methane. The number after this symbol (i.e. G50-27) represents the percentage of total methane flow rate supplied with the atomizing air.

3.3 Results and Discussion

3.3.1 Un-Insulated Combustion Chamber

Exploratory experiments were performed in an un-insulated quartz chamber co-fired with glycerol and methane. In this fuel flexible, dual-fuel combustor, glycerol represents a high viscosity liquid fuel and methane represents a typical gaseous fuel. Figure 3.3 shows visual flame images for all conditions. G00 (0% glycerol and 100% methane for a fixed heat release

rate) fuel results in a very short intense flame. Increasing the glycerol content increases the flame length and tends to decrease the flame intensity. Figure 3.4 shows chemiluminescence images for various glycerol/methane flames. Chemiluminescence images were acquired by an intensified CCD camera using a filter to capture light in a specific wavelength (that of radicals released during combustion), providing an estimation of the reaction zone. The first image, for G00 shows a short intense reaction zone. With increasing glycerol content, the reaction zone lengthens, presumably to ensure vaporization of liquid fuel, glycerol's higher ignition energy, and slower reactions. For pure glycerol (G100) the reaction zone fills the entire combustor, while the intensity of emission is poor in the downstream region.

Figure 3.5 shows the CO emissions for two of the test fuels (G75 and G50) shown in figure 3.3 and figure 3.4. The G75 flame resulted in CO emissions up to 5000 ppm at the combustor wall and about 300 ppm at the combustor center. For lower glycerol content in G50 flames, CO emissions decreased to around 2000 ppm at the combustor wall and 60 ppm at the combustor center. The high CO emissions at the wall can be attributed to the heat loss at the wall, resulting in lower temperature with significant quenching reactions to prevent complete CO oxidation. In practical burner applications, wall temperatures must be higher to avoid these quenching reactions. The G100 flame was not stable in the un-insulated combustion chamber. Because of glycerol's high enthalpy of vaporization and high ignition temperature, significant energy from the flame must be convected upstream to pre-vaporize and preheat incoming fuel. Large CO emissions arising from diffusion mode burning can be expected in the absence of such thermal feedback. This situation is further exasperated in the wall region of the un-insulated combustor.

Figure 3.6 shows NO_x emissions for G75 and G50 flames. For the G75 flame, NO_x emissions range between 13 to 19 ppm at the combustor wall and only around 4 ppm in the combustor center. Larger droplets tend to migrate to the periphery where they are likely to burn in diffusion mode at high temperature, causing high thermal NO_x [Turns 2000]. Decreasing the glycerol content in the G50 flame reduced NO_x emissions to around 10 ppm at the combustor wall and to 3 ppm at the combustor center. Lower NO_x emissions for the G50 flame can be attributed to greater fuel-air premixing upstream of the flame. Although the quartz combustor facilitated optical observation of the flame, insulating the combustion chamber was deemed necessary in practice to minimize heat loss, increase wall temperature and improve thermal feedback to the incoming fuel. Thus, for all further experiments, the quartz combustor was insulated with a 5 cm thick layer of alumina fiber ($k=0.315 \text{ BTU/hrft}^2\text{°F/inch}$ at 1200°C). The insulated system more accurately represents an industrial burner placed in a heated environment.

3.3.2 Effect of Air to Liquid Mass Ratio (ALR)

Figure 3.7 shows the effect of ALR on the heat loss through the three zones in the insulated combustor wall. At low ALR, the heat loss is smaller since poor atomization resulted in incomplete combustion and thus, lower HRR and wall temperatures. As the ALR increases, the heat loss reaches a nearly steady state value (approximately 0.98 kW total or 14% of HRR) in all zones. The need for insulation is clearly demonstrated since significant heat loss occurs even in an insulated combustor.

Experiments were conducted by varying the ALR in an attempt to determine an optimum ALR. Figure 3.8 shows CO emissions at five radial locations at the combustor exit plane. ALR was varied in an attempt to determine an optimum ALR. At very low ALR (< 1), the FB injector produces large glycerol droplets that burn in diffusion mode. The diffusion mode burning results

in high local temperature, causing higher CO emissions. The large droplets may not fully evaporate and oxidize during the residence time available in the combustor (approximately 0.92 s). As the ALR was increased to 1.13, a minimum in CO emissions (< 130 ppm at wall) was reached. Further increase in ALR increased CO emissions. This result could be attributed to a high velocity region in the center of the combustor, which effectively reduces the residence time for the liquid glycerol. Figure 3.9 shows the effect of ALR on NO_x emissions at the same five radial positions. Increasing ALR results in slight reduction of NO_x emissions from 6 to 11 ppm at ALR = 0.9 to 5 to 6 ppm at ALR = 1.7. NO_x reduction at higher ALR indicates more premixed combustion causing lower local flame temperatures. Based on CO and NO_x emissions depicted in figures 3.8 and 3.9, ALR = 1.13 was deemed the optimum ALR for other experiments.

3.3.3 Effect of Heat Release Rate (HRR)

Figure 3.10 shows the heat loss through the combustor wall for ALR = 1.13, G100 flames at 4, 7, and 11 kW HRRs. The 4 and 7 kW HRR cases result in nearly identical heat loss profiles and total heat loss of approximately 0.95 kW, while the 11.6 kW HRR case results in significantly lower heat loss (total 0.73 kW). Thus, residence time for the 11.6 kW case could be inadequate to ensure complete combustion.

Figure 3.11 shows the effect of HRR on CO emissions. For all cases, CO emissions increase with HRR. CO emissions were 3 to 15 ppm, 20 to 120 ppm, and 80 to 1200 ppm for HRRs of 4, 7, and 11.6 kW, respectively. The difference in emissions could be due to the higher HRRs requiring higher fuel and air flow rates; therefore resulting in shorter residence time for CO oxidation. Calculated residence times were 1.62, 0.92, and 0.55 s for the 4, 7, and 11.6 kW cases, respectively. Slight reductions in CO emissions were possible for the 4 kW case by

increasing ALR to 1.35. Figure 3.12 shows the NO_x emissions for the three HRR cases. All three HRR cases have NO_x emissions between 4 and 8 ppm and are within the instrument uncertainty.

3.3.4 Effect of Methane Addition

Figure 3.13 shows the heat loss profiles for the six cases co-fired with glycerol/methane. Increasing the methane content increased the heat loss, but this trend was suppressed as more methane was supplied through the injector. Methane flow through the injector is likely to create a combustible mixture closer to the injector to improve glycerol vaporization (and the subsequent reactions). Thus, supplying methane through the injector increases local equivalence ratio in the glycerol spray, presumably resulting in higher local temperatures in the center of the combustor as opposed to the walls, resulting in lower heat loss.

Figure 3.14 shows the CO emissions for the six glycerol/ methane cases. The G100 flame resulted in the highest CO emissions with values near 140 ppm at the wall and 20 ppm at the combustor centerline. These results for G100 are significantly lower than the results for G50 in the un-insulated combustor, indicating that the FB injector can successfully atomize pure glycerol in the properly insulated environment. The G90 flame reduced the CO emissions significantly at the wall, especially with the introduction of the methane through the swirler, which creates a more combustible mixture near the wall, aiding in CO oxidation. When G90 methane was passed through the injector, the CO emissions at the wall increased to near the G100 case at the walls, while CO emissions were lower at the combustor center. The G50 flames resulted in CO emissions between 5 and 20 ppm for all cases. Supplying methane through the swirler increases local equivalence ratio near the wall, while injecting methane with the atomizing air increases local equivalence ratio at the combustor centerline. Wherever the

local equivalence ratio was increased CO emissions were reduced. The proposed mechanism is that the increased local equivalence ratio allowed combustion to take place earlier, supplying local heat release to aid in the vaporization of glycerol. Figure 3.15 shows the NO_x emissions for the same six cases. The G100 flame resulted in NO_x emissions of around 4 to 5 ppm. As more methane was introduced, NO_x emissions increased, except when methane was supplied with atomizing air. Splitting methane through the swirler and atomizer results in lower local equivalence ratios (and consequently lower temperatures) than supplying all of the methane through the swirler. These lower temperatures result in lower thermal NO_x formation. Both the CO and NO_x emissions profiles suggest that splitting methane between the swirler and atomizer is an effective means to reduce emissions in G50 flames.

3.4 Conclusions

FB atomization provides a simple, robust method for the utilization of glycerol in continuous flow combustion systems. First, an FB atomizer was integrated into an un-insulated combustor resulting in CO emissions up to 5000 ppm and NO_x emissions below 20 ppm. Next, the FB atomizer was implemented in an insulated combustor to cleanly combust glycerol with no fuel preheating or mixing. The amount of atomizing air used to create the glycerol fuel spray was seen to be critical in the resulting flame emissions. Heat release rate was varied and it was seen that sufficient residence time (>0.92 s) is necessary to completely combust the glycerol fuel. The effect of adding methane to the fuel was seen to dramatically change the flame structure and the resulting emissions. Methane addition seems to be an effective method for optimizing glycerol combustion while effectively reducing emissions. Overall, it was seen that the FB concept has great application in the atomization of highly viscous fuels with minimal or no system modification.

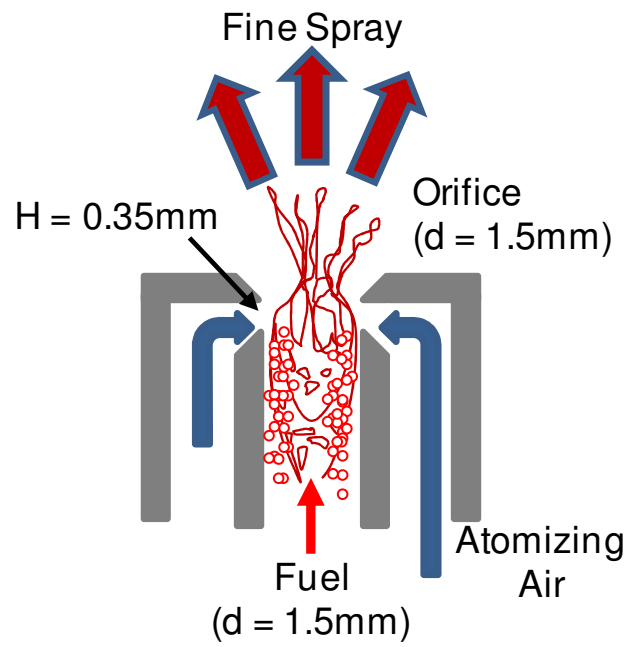


Figure 3.1 FB injection concept

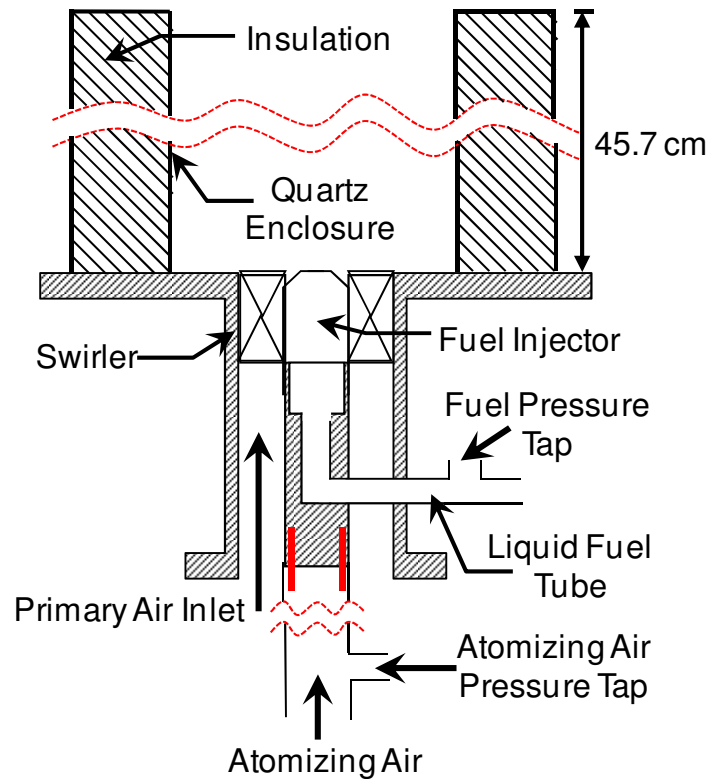


Figure 3.2 Experimental setup

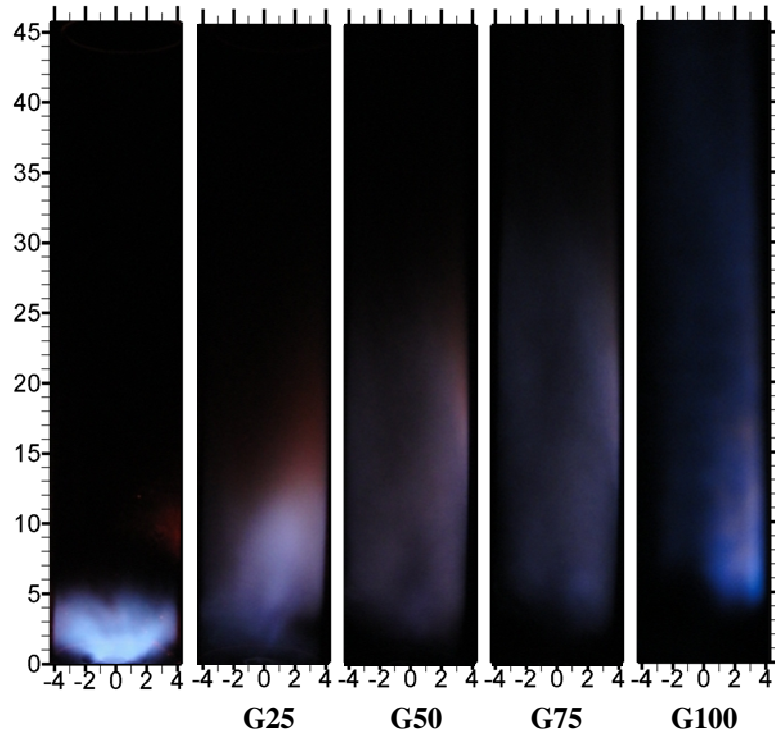


Figure 3.3 Effect of glycerol content on flame images

(HRR = 7 kW, atomizing air flow = 27 slpm)

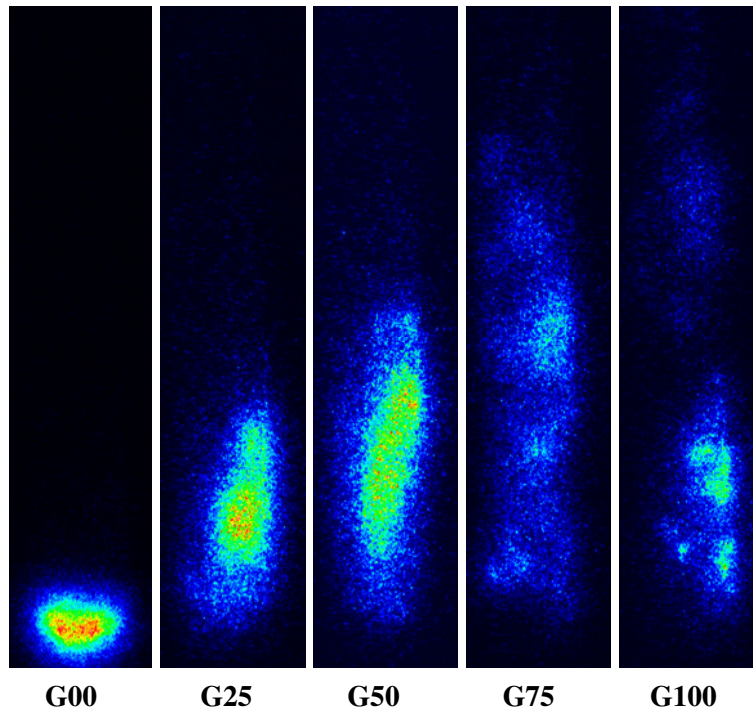


Figure 3.4 Effect of glycerol content on reaction zone from chemiluminescence images. Red areas represent intense reaction zones

(HRR = 7 kW, atomizing air flow = 27 slpm)

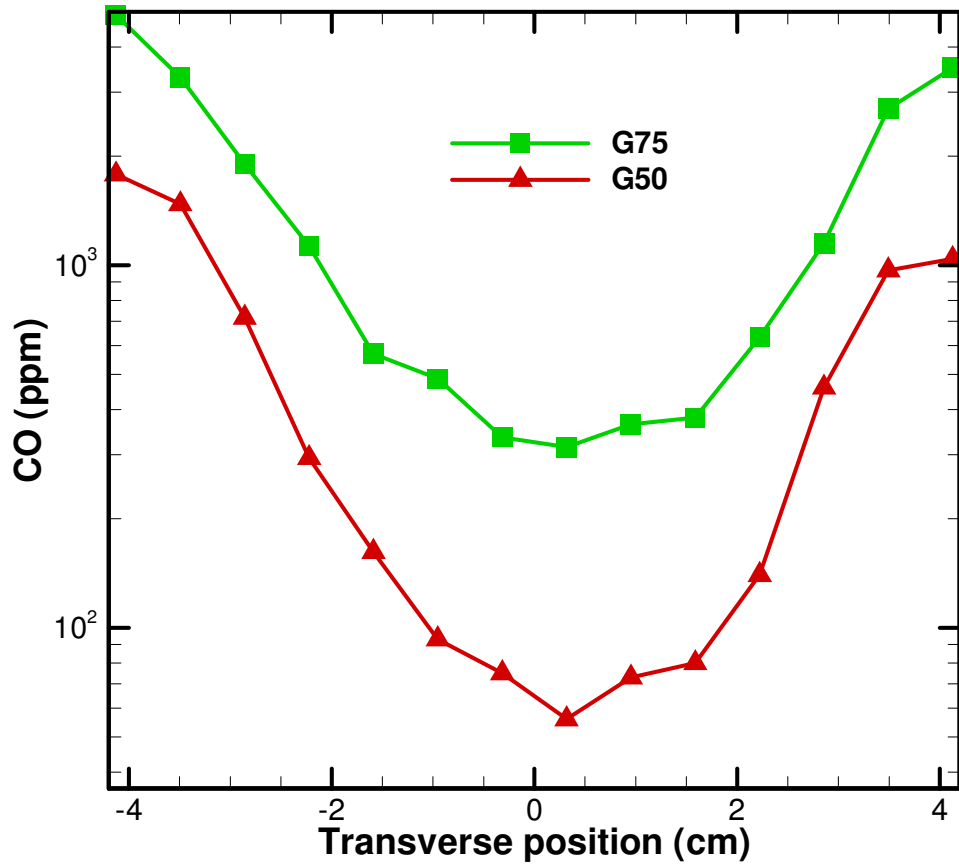


Figure 3.5 CO emissions from un-insulated combustion chamber

(HRR = 7 kW, atomizing air flow = 27 slpm)

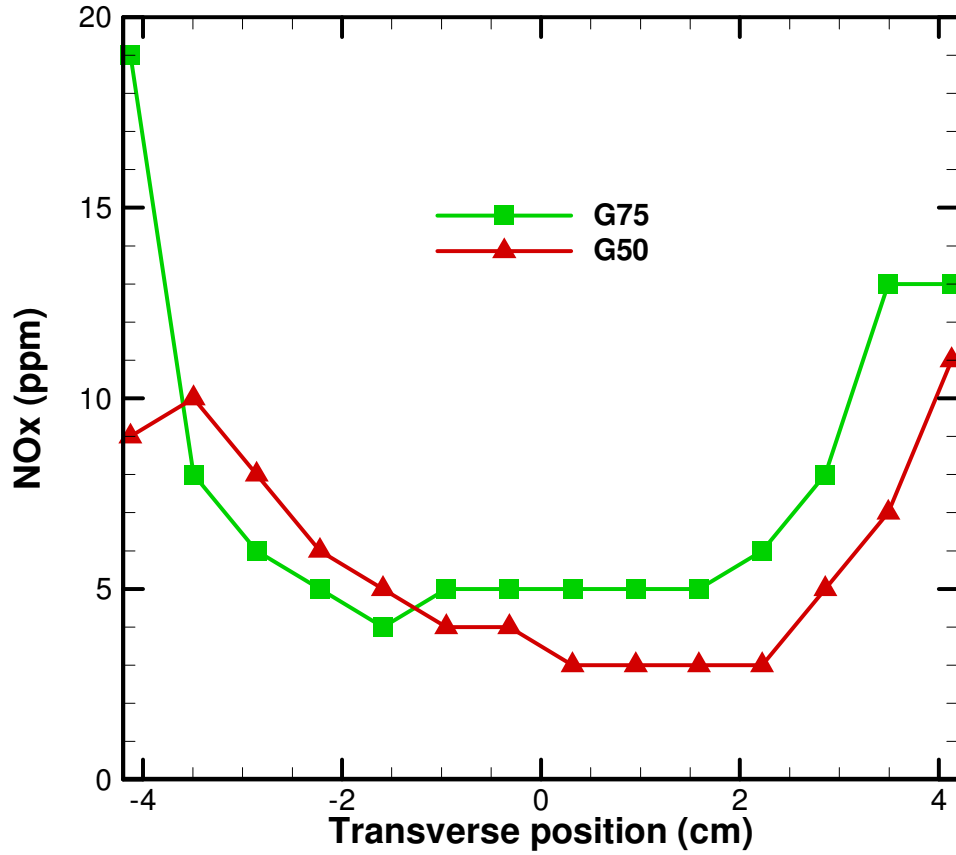


Figure 3.6 NO_x emissions from un-insulated combustion chamber
(HRR = 7 kW, atomizing air flow = 27 slpm)

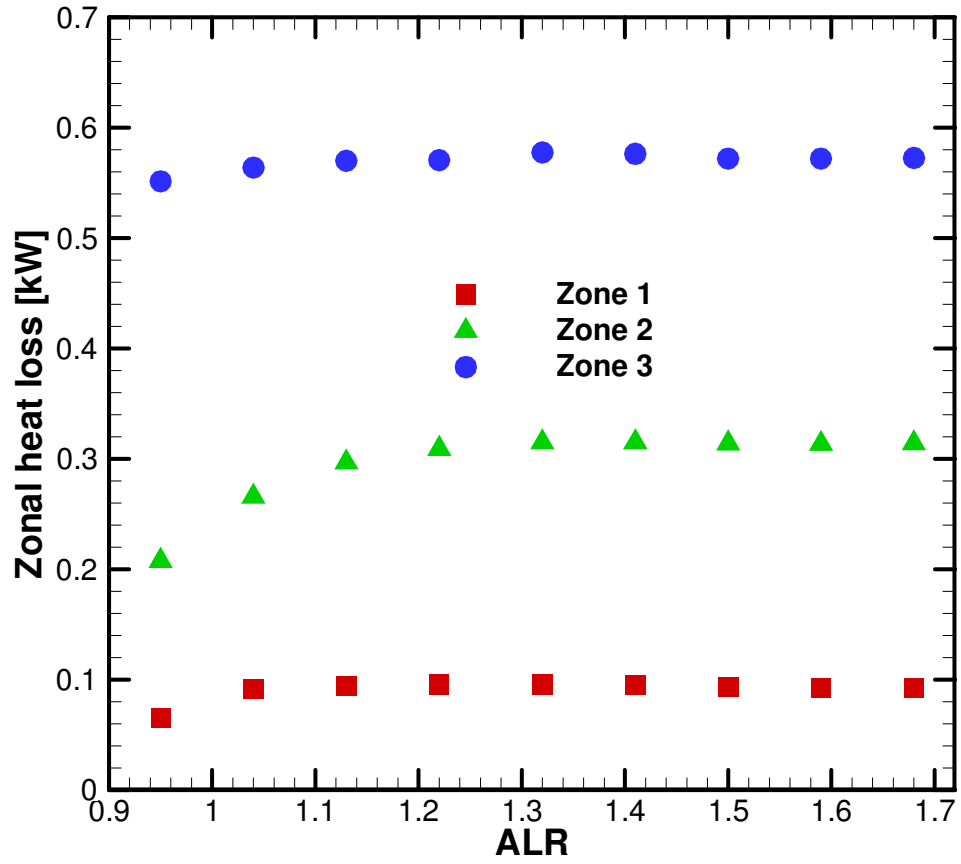


Figure 3.7 Effect of ALR on heat loss through insulated combustor wall
 (HRR = 7 kW, $\Phi = 0.77$)

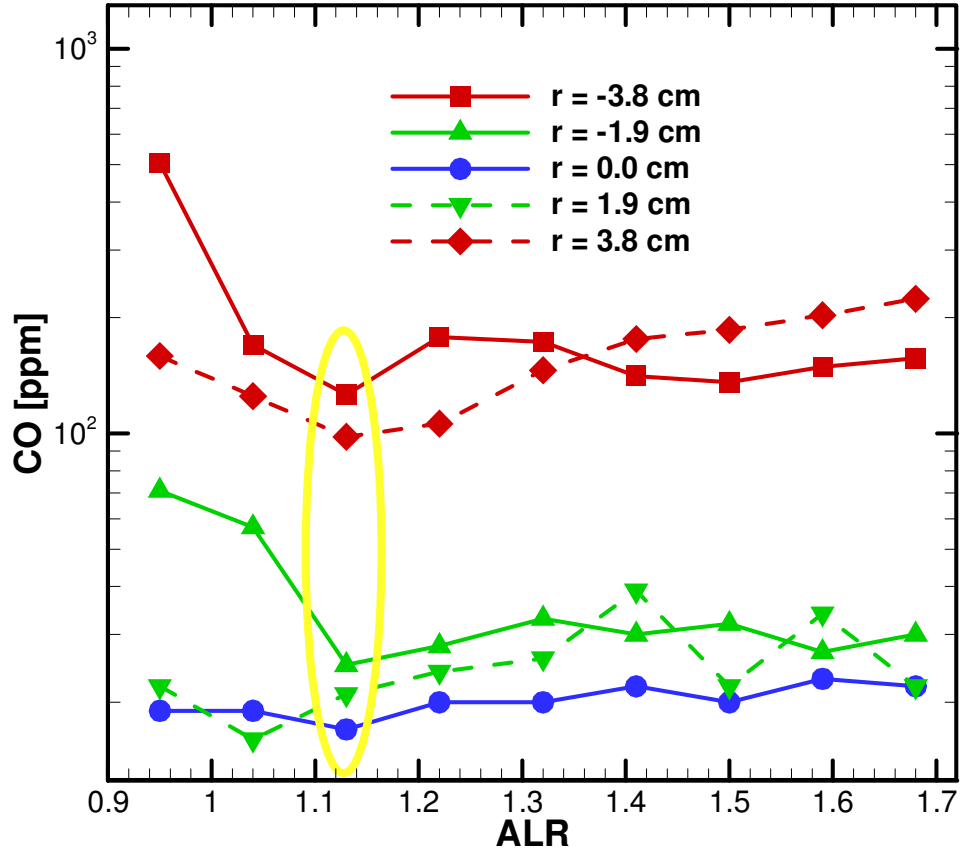


Figure 3.8 Effect of ALR on CO emissions at exit plane of insulated combustor
(HRR = 7 kW, $\Phi = 0.77$)

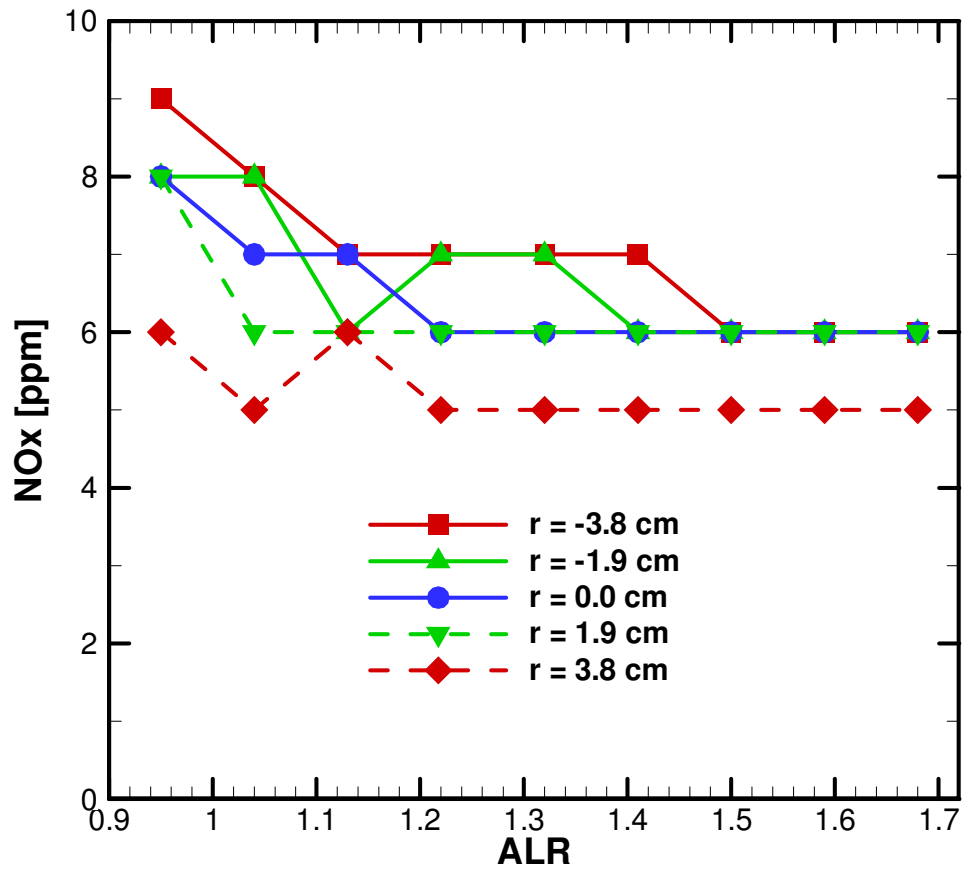


Figure 3.9 Effect of ALR on NO_x emissions at exit plane of insulated combustor
(HRR = 7 kW, $\Phi = 0.77$)

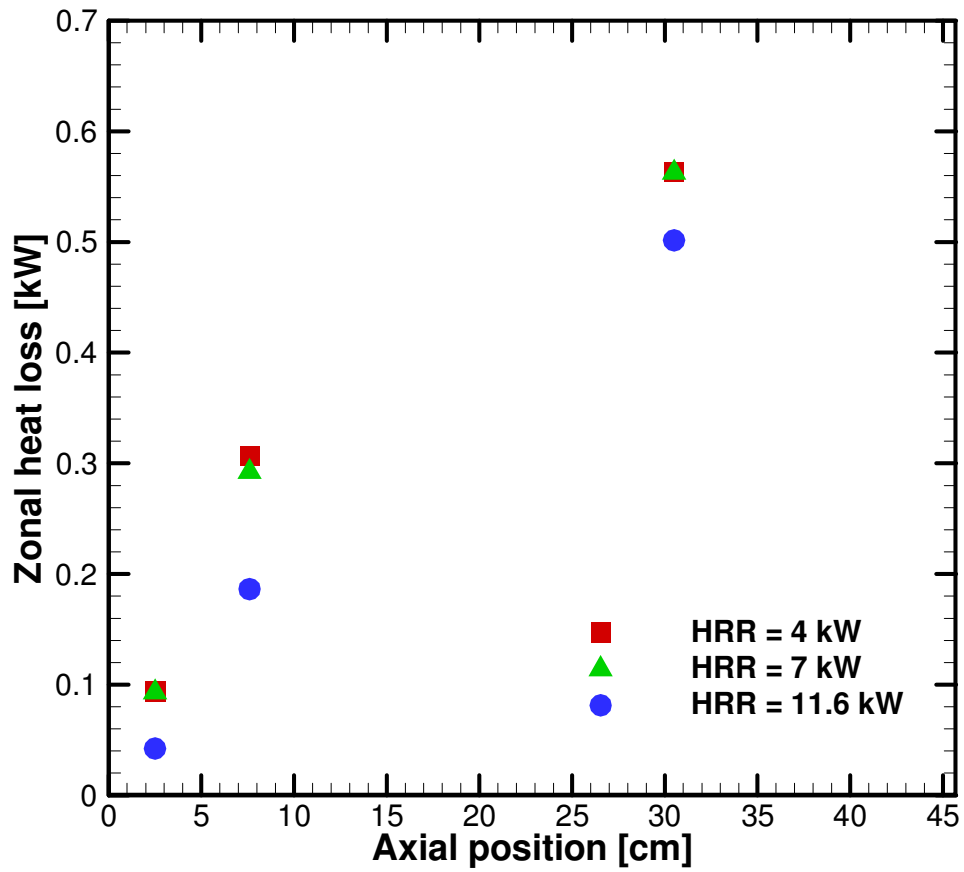


Figure 3.10 Effect of HRR on heat loss through insulated combustor wall

($\Phi = 0.77$, ALR = 1.13)

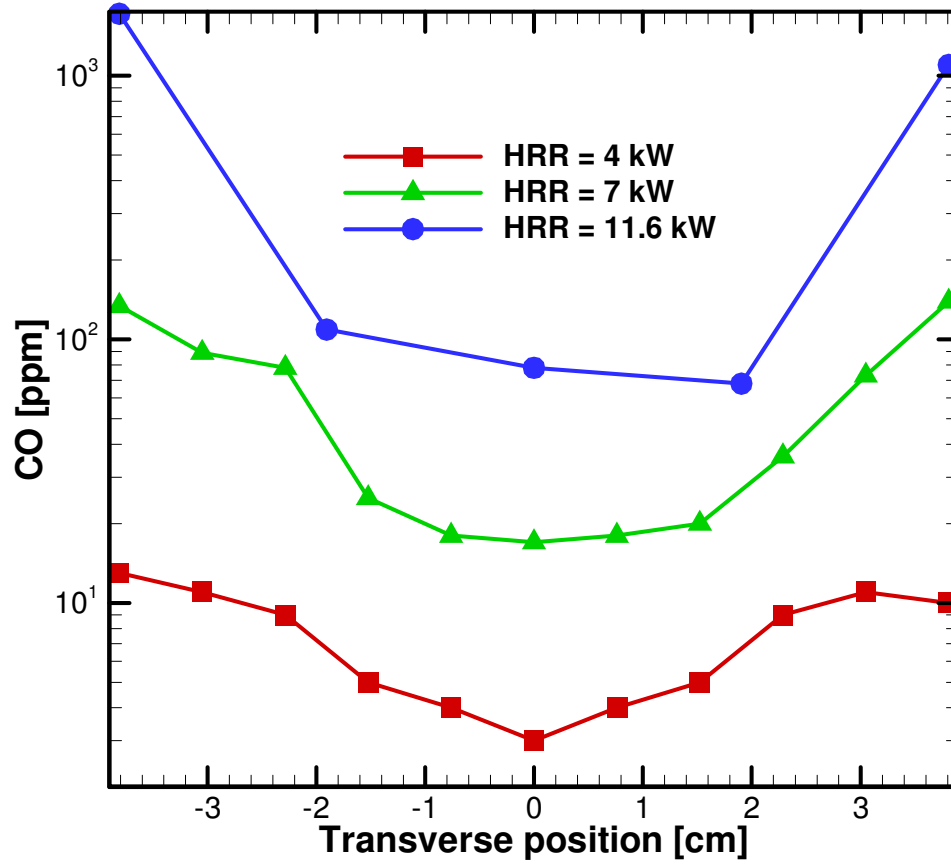


Figure 3.11 Effect of HRR on CO emissions at exit plane of insulated combustor

($\Phi = 0.77$, ALR = 1.13)

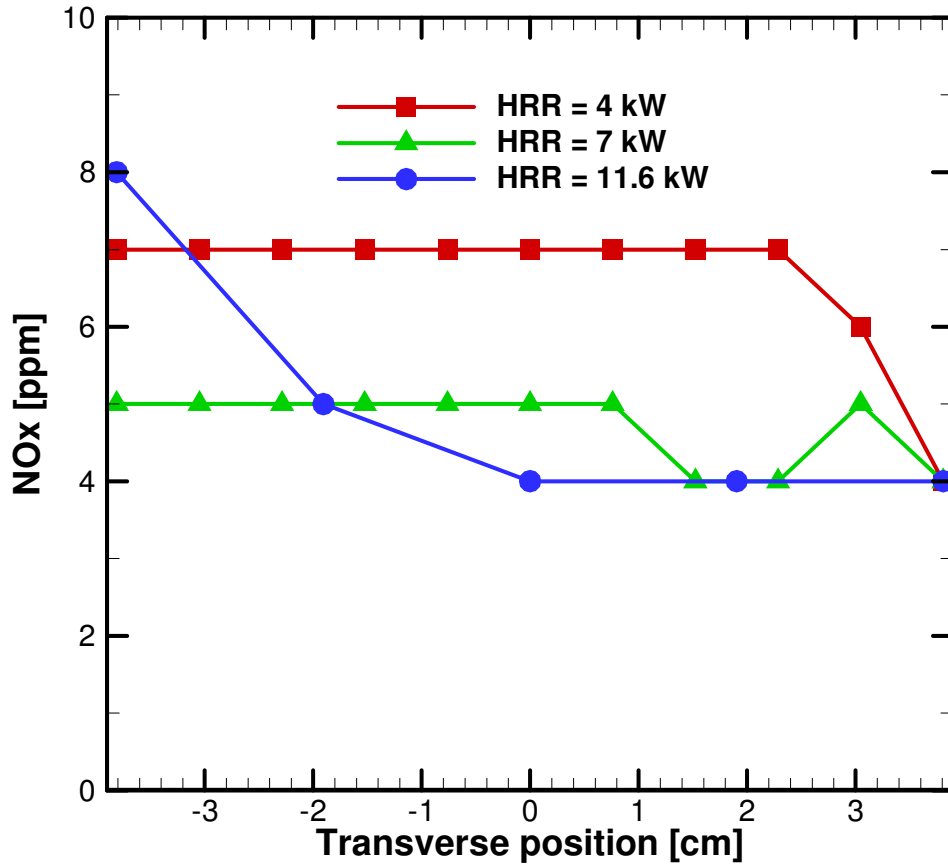


Figure 3.12 Effect of HRR on NO_x emissions at combustor exit plane of insulated combustor

($\Phi = 0.77$, ALR = 1.13)

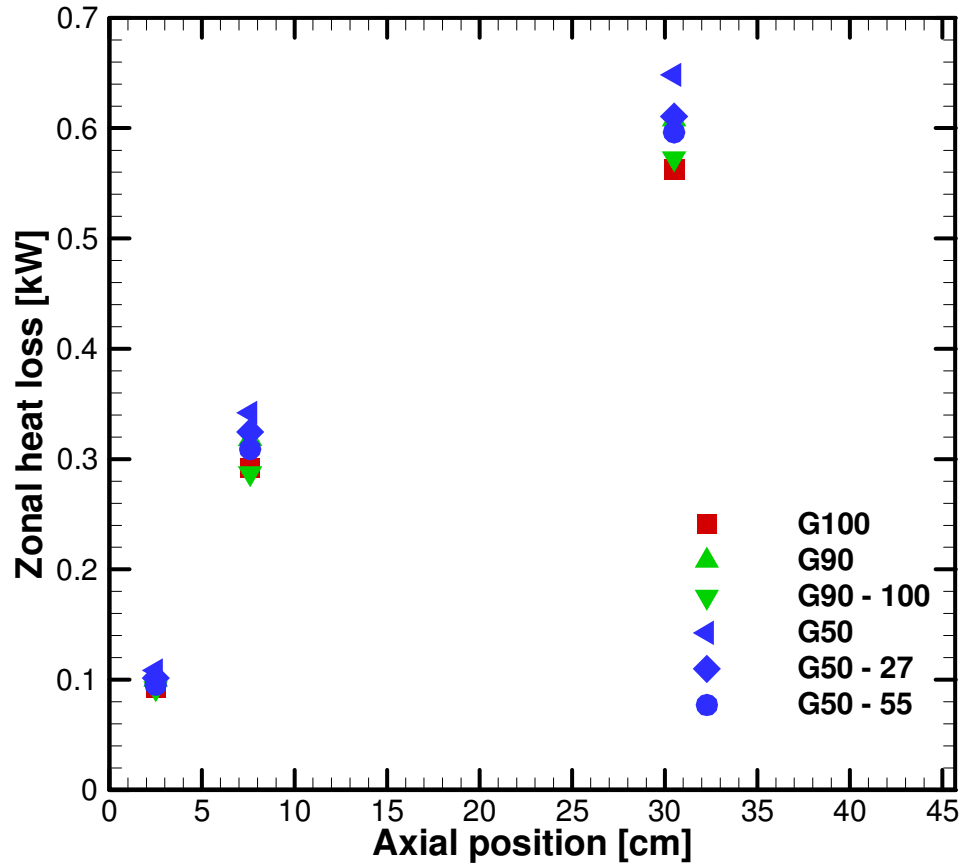


Figure 3.13 Effect of methane addition on heat loss through insulated combustor wall

(HRR = 7 kW, atomizing gas flow = 30 g/min)

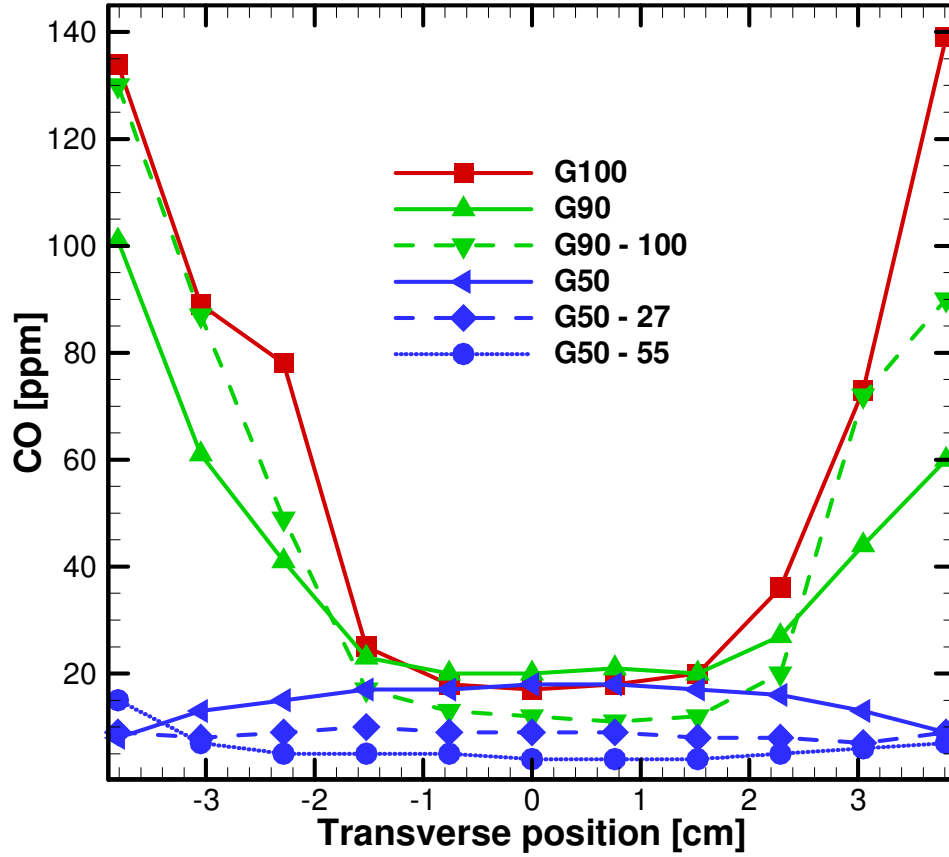


Figure 3.14 Effect of methane addition on CO emissions at exit plane of insulated combustor
(HRR = 7 kW, atomizing gas flow = 30 g/min)

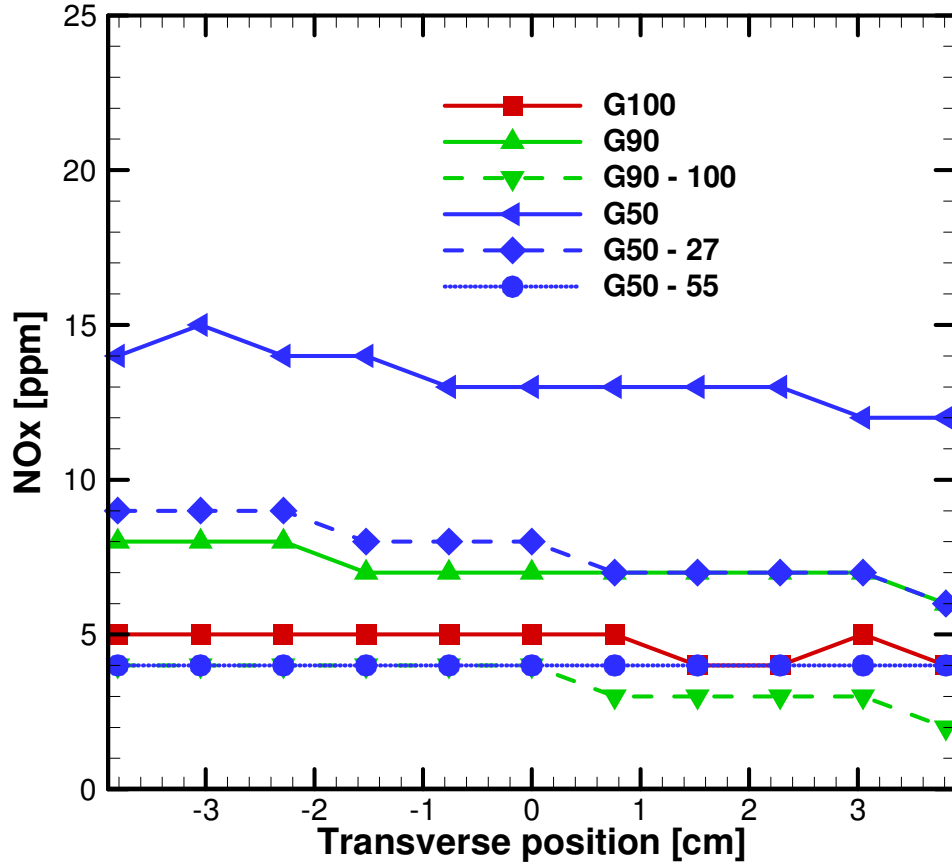


Figure 3.15 Effect of methane addition on NO_x emissions at exit plane of insulated combustor
(HRR = 7 kW, atomizing gas flow = 30 g/min)

CHAPTER 4

FLOW AND DROPSIZE MEASUREMENTS IN WATER SPRAYS

4.1 Background

Clean combustion of liquid fuels is dependent on effective atomization to increase the specific surface area of the fuel. Atomization is a physical process whereby a volume of liquid is converted into a multiplicity of small droplets. Principally, it produces a large droplet surface area-to-mass ratio in the liquid phase, thereby increasing the evaporation rate and fuel-air mixing in the combustor. Effective fuel atomization is essential to minimize emissions of particulate matter (PM), carbon monoxide (CO), and nitric oxides (NO_x). Efficient combustion requires optimal droplet size distribution within the spray for a range of operating conditions to include droplets both large enough to penetrate into the combustion chamber and small enough to vaporize within the short residence time upstream of the reaction zone (Lefebvre, 1989). The atomizer produces a spray in various regimes depending on the liquid's kinetic energy, surface tension, kinematic viscosity, and interactions with the atomizing and/or combustion air. Past efforts have resulted in the development of different atomizer designs (Lefebvre, 1989, 1999) and related optical diagnostics and modeling techniques (Kuo 1996a,b) leading to the understanding of the structure and breakup properties of sprays (Faeth et al., 1995; Sirignano and Mehring, 2000; Sirignano, 2005) and single and/or group droplet evaporation processes (Law 1982; Chiu, 2000; Birouk and Gokalp, 2006).

The air-blast (AB) atomizer is one of the configurations to break up the fuel jet using atomizing air and has been widely described in the literature (Karl et al., 1996; Clack et al.,

2004; Hoeg et al., 2008; Bolszo and Mc-Donell, 2009). The AB atomizer delivers air at a relatively large velocity to destabilize the fuel jet and to disperse the resulting spray into the reaction zone. The transfer of energy occurs by shear interaction resulting from the large velocity gradient between the two phases. The AB atomizer produces finer droplets as the supply pressure or mass flow rate of the atomizing air is increased, which also increases the power requirement of the atomizer (Lefebvre, 1992). However, the AB atomizer performs poorly with fuels of high kinematic viscosity, creating large droplets that burn in diffusion mode to result in high PM, CO, and NO_x emissions.

Another process known as effervescent atomization (EA) injects high-pressure gas directly into the liquid in a mixing chamber upstream of the discharge orifice. The injected gas forms bubbles to produce a two-phase mixture that flows through the orifice, and on exiting the orifice, the gas bubbles expand rapidly to break up the surrounding liquid into droplets. The liquid breakdown mechanism with EA is fundamentally different from that found in pressure, air-assist, or AB atomizers. The EA process offers several benefits over the AB atomizer, i.e., it produces a spray with finer droplets, the atomizer performance is relatively insensitive to the liquid's kinematic viscosity, and the larger diameter of the orifice alleviates clogging problems and simplifies fabrication (Sovani et al., 2001). However, in the EA process, the spray angle is small, air must be pressurized to the liquid's pumping level, and the spray produced can exhibit unsteadiness related to the two-phase flow in the injector orifice.

Recently, Gañán-Calvo (2005) reported the discovery of a simple, reproducible atomizer configuration, the so-called flow-blurring (FB) atomizer, with gas-liquid interactions that yield very high atomization efficiency. For a specified liquid flow rate and total energy input, Gañán-Calvo (2005) claims that the FB atomizer creates about 5–50 times more droplet surface area

than any other pneumatic atomizer of the “plain-jet airblast” type. Figure 4.1 illustrates the operating principle of the FB atomizer. The atomizing air is supplied through a small gap between the exit of the liquid supply tube of inside diameter d and a coaxial orifice of the same diameter. As the liquid supply tube is moved closer to the orifice plate, a bifurcation in the flow field takes place inside the atomizer. When the axial distance H between the liquid supply tube exit and orifice plate is small, i.e., $H/d < 0.25$, some of the atomizing air is forced a short distance into the liquid supply tube. The backflow of atomizing air increases the local pressure and results in intense two-phase mixing at the tip of the liquid supply tube. Subsequently, the pressure decreases as the two-phase mixture discharges through the orifice plate. This results in rapid expansion of air bubbles to break down the surrounding liquid into fine droplets. Since the two-phase mixing occurs at the tip of the liquid supply tube, the FB atomization overcomes drawbacks of the EA process such as the flow unsteadiness and the need for high-pressure atomizing air. The flow-blurring effect is not observed for $H/d > 0.25$, whereby symmetric and/or asymmetric disturbances cause the jet breakup similar to an AB atomizer.

The FB atomizer has been found to provide superior combustion performance in terms of (i) the reduced emissions in diesel and kerosene flames (Panchasara et al., 2009a), (ii) its ability to effectively atomize (and cleanly combust) liquid biofuels with kinematic viscosity nearly 15 times that of diesel (Simmons et al., 2008), and (iii) its ability to atomize liquid fuel in a miniature combustor with a combustor volume of only 2 cm^3 (Sadasivuni and Agrawal, 2009). For example, Panchasara et al. (2009a) compared diesel and kerosene flame emissions from FB and AB atomizers using a swirl-stabilized combustor operated at atmospheric pressure. Results provided evidence that for given fuel and atomizing airflow rates, the FB atomizer produces up to three times lower NO_x and CO emissions compared to the AB atomizer. Reduction in

emissions was attributed to smaller droplets produced by the FB atomizer. Combustion experiments by Simmons et al. (2008) demonstrated that the FB atomizer can atomize high-viscosity vegetable oil.

The FB atomizer produces smaller droplets (Rosell-Llompart and Gañán-Calvo, 2008) although, to the best of the authors' knowledge, detailed spray measurements for this configuration have not been reported in the literature. Thus, the objective of the present study is to document the spray characteristics of an FB atomizer. Measurements in an AB atomizer are also obtained as a baseline for comparison. Experiments are conducted for different atomizing air-to-liquid mass ratios (ALRs) at ambient conditions of temperature and pressure using water as the working liquid. Water was chosen for this study because it greatly simplifies the experimental setup for cold spray studies, as there is no need to worry about fuel cleanup. Thus, this study does not consider fuel-air mixing by combustion air or fuel evaporation by thermal feedback from the flame. First, pressure measurements through both injectors are presented. Next, qualitative spray images acquired by a laser sheet visualization system are presented. Finally, quantitative data on droplet size distributions, mean velocity, and RMS velocity, acquired using a two-component phase Doppler particle analyzer (PDPA) system, are reported. The following sections provide details of the experimental setup, results, and discussions.

4.2 Experimental Setup

Figure 4.2 shows a schematic diagram of the experimental setup. Distilled water was delivered to the test setup using a peristaltic metering pump with an uncertainty of $\pm 0.25\%$ of the reading. The water passed through a pulse dampener before entering the atomizer. Atomizing air at room temperature was delivered from a compressed air supply, metered by a needle valve, and measured by a calibrated mass flow meter with an uncertainty of ± 1.5 standard liters per minute

(slpm) or $\pm 3.0 \times 10^{-5}$ kg/s. A flow-straightening channel was placed downstream of the spray to prevent flow recirculation and to collect the water spray. The water flow rate was kept constant at 12.0 milliliters per minute (mlpm) (2.0×10^{-4} kg/s) to match the volumetric fuel flow rate used in the combustion experiments (Simmons et al., 2008). The airflow rate was varied to obtain ALRs of 1.0–4.0 to concur with prior combustion studies (Simmons et al., 2008; Panchasara et al., 2009a,b).

Figure 4.3 depicts the interior flow paths for the two atomizers. The AB atomizer is a commercially available model (Delavan model 30609-2). The liquid and atomizing airflow rates in this study are within the working range of the AB atomizer as specified by the manufacturer, i.e., liquid flow rate of 5–35 mlpm (8.3×10^{-5} – 5.8×10^{-4} kg/s) and airflow rate of 10–59 lpm (2.0×10^{-4} – 1.2×10^{-3} kg/s). In the AB atomizer, a stream of swirling atomizing air breaks down the central liquid jet of inside diameter, $d = 0.3$ mm. Presumably, the AB atomizer has been optimized by the manufacturer. The AB atomizer body was retrofitted in-house to implement the FB atomizer concept, which required hardware changes only to the internal flow path. The FB atomizer consisted of a central liquid tube ($d = 1.5$ mm) and a co-annular atomizing air passage. The two-phase mixture exits through the orifice of diameter $d = 1.5$ mm in the discharge plate located such that $H = 0.35$ mm. As discussed above, this geometry creates a two-phase mixture at the tip of the liquid supply tube to produce a fine spray.

A laser sheet visualization system was employed to acquire images of the spray produced at different operating conditions. The laser sheet was created by a 200 mW diode-pumped solid state laser producing a 532 nm green laser beam. The laser beam passed through a 12.5 mm diameter cylindrical lens with a 12.5 mm effective focal length, and a 25 mm diameter spherical lens with an effective focal length of 750 mm to form an approximately 1.5 mm thick laser sheet

to illuminate the spray. Spray images were taken by a digital camera, set for an exposure time of 1/8 s, and mounted on a fixed tripod to ensure a consistent field of view for different atomizers and operating conditions.

A 2D PDPA system from TSI Inc. was used to measure the flow velocities and droplet diameters. The PDPA is a point sampling device based on the principles of light scattering interferometry. The laser beams of the analyzer intersect at the sample volume location. The droplets, assumed to be spherical, pass through the intersection region of the laser beams to scatter light and form an interference fringe pattern. For a moving droplet, the scattered interference pattern sweeps past the receiver aperture at the Doppler difference frequency, which is proportional to the droplet velocity. The spatial frequency of the fringe pattern is inversely proportional to the droplet diameter. The phase shift between the Doppler burst signals from different detectors is proportional to droplet diameter assuming a spherical shape. The PDPA technique requires no calibration because the measured droplet diameter and flow velocities are dependent only on the laser wavelength and optics used.

The laser beam is created by a 2 W water-cooled argon-ion laser and then separated into a pair of 514.5 nm green beams and a pair of 488 nm blue beams using a beam separator assembly. One beam of each pair is shifted by 40 MHz using a Bragg cell. Each beam is focused onto a fiber-optic cable, which delivers the beams to the 250 mm focal length PDPA transmitter. The PDPA receiver was set at an angle of 150° from the transmitter to collect the refracted light intensities from the spray. The detected signals were acquired by the data acquisition system (TSI PDM 1000 photo detector module and FSA 4000 multibit digital processor), and analyzed by the TSI software, FlowSizer version 2.0.4. The minimum droplet diameter detected by the system was approximately 3.5 μm . Further details of the PDPA system are given in appendix F.

Experiments were conducted with the atomizer attached to a 3D traverse system via a customized bracket, while the PDPA system was held stationary. Radial profiles were taken at axial distance Y of 1.0, 2.0, and 3.0 cm from the atomizer exit. The peak axial velocity was used to locate the center of the spray. Data rates of up to 40 kHz were obtained near the center of the spray. Data rates and axial velocities decreased nearly to zero as the detection volume reached the outer edge of the spray cone. Each data point represents approximately 10,000 valid measurements.

4.3 Results and Discussion

In this section, pressure measurements are reported to explain the operating principle of the FB atomizer. Next, a qualitative description of the spray is provided by direct images acquired at different ALRs. Finally, the flow characteristics of the spray are quantified by Sauter mean diameter (SMD), and mean and RMS velocities.

4.3.1 Pressure Measurements

The operational efficiency of the atomizer was determined by the pressure drop in the atomizing air line. Thus, the air supply pressure was measured by a pressure transducer (0–350,000 Pa range) installed upstream of the atomizer using a T-junction. The measured pressure was effectively the pressure drop in the air line because the atomizer was open to the ambient. Measurements were taken for different airflow rates without and with the liquid flow rate (m_l) of 12.0 mlpm (2.0×10^{-4} kg/s). Results in figure 4.4a show that the atomizing air pressure drop in the FB atomizer increases with increasing airflow rate. The liquid flow through the FB atomizer had virtually no effect on the atomizing air pressure drop. Figure 4.4a also presents data for the AB atomizer and shows that the AB atomizer incurs a slightly higher (about 10,000 Pa) atomizing air pressure drop at any given airflow rate. The liquid flow in the AB atomizer also

increased the atomizing air pressure drop. The smaller atomizing air pressure drop in the FB atomizer compared to that in the AB atomizer is notable, especially since, unlike the AB atomizer, the FB atomizer geometry has not been optimized.

The liquid supply pressure upstream of the atomizer was also measured to estimate the pressure drop in the liquid line. Figure 4.4b presents the measurements obtained without the atomizing airflow in the atomizer. Evidently, the liquid pressure drop in the FB injector varies between 0 and 370 Pa for the liquid flow rate of 0–50 mlpm (8.3×10^{-4} kg/s), respectively. The liquid pressure drop in the AB atomizer is significantly higher, i.e., between 0 and 17,000 Pa. This result can be explained by the difference in diameters of the liquid supply tubes, i.e., 1.5 mm for the FB atomizer versus 0.3 mm for the AB atomizer. Measurements in figure 4.4b represent only the frictional pressure drop in the liquid supply tube, without accounting for the interactions with the atomizing air. The liquid supply pressure was also measured for $m_1 = 12.0$ mlpm (2.0×10^{-4} kg/s) while the atomizing airflow rate was varied between 0.0 and approximately 40.0 slpm (8.0×10^{-4} kg/s). Data presented in figure 4.4c show some interesting trends. In the FB atomizer, the atomizing airflow raises the liquid supply pressure, which increases as the atomizing airflow rate is increased. In contrast, in the AB atomizer, the atomizing airflow decreases the liquid supply pressure to below the ambient value. Moreover, the liquid supply pressure is nearly independent of the atomizing airflow rate. These results indicate that the interactions of atomizing air and liquid flows at the exit of the liquid supply tube are fundamentally different in the FB and AB atomizers. Because the atomizing airflow increases the pressure at the tip of the liquid supply tube, the FB injector requires a higher liquid supply pressure as compared to the AB atomizer.

Next, the pressure at the exit of the liquid supply tube was estimated from Bernoulli's equation to understand how atomizing airflow interacted with the liquid flow. The pressure loss in the liquid supply tube was taken from figure 4.4b for $m_1 = 12.0$ mlpm (2.0×10^{-4} kg/s), the flow velocity at the tube exit was found as $u = m_1 / (\pi d^2 / 4)$, and the flow velocity upstream of the atomizer was neglected. Results presented in figure 4.4c show that the pressure at the exit of the liquid supply tube is above ambient (positive) in the FB atomizer and below ambient (negative) in the AB atomizer. Therefore, in the FB atomizer, the pressure of the two-phase mixture decreases as it exits through the orifice plate. Consequently, the air bubbles in the mixture expand to breakdown the surrounding liquid to form the spray. In contrast, in the AB atomizer, the pressure of the atomizing air increases as it exits through the orifice to form the spray by destabilizing the liquid jet.

4.3.2 Spray Images

Spray images for different ALRs presented in figure 4.5 provide a qualitative assessment of the FB injector. Results show a cone angle of approximately 25° with maximum radial penetration of about 15 mm. Interestingly, the spray image appears to be nearly independent of the ALR ranging from 1.0 to 4.0. Low sensitivity of the FB atomizer to the ALR is notable since it indicates that the atomizer could be effective at a lower ALR to incur a smaller pressure drop. For comparison, figure 4.6 shows the corresponding spray images for the AB atomizer. In this case, the ALR has a significant effect on the width or cone angle of the spray. For a smaller ALR, large droplets are produced that travel farther to widen the spray or increase the cone angle. The spray width decreases as the ALR increases, indicating that smaller droplets are produced at higher ALRs. The spray image at the highest ALR for the AB atomizer resembles that at the lowest ALR for the FB atomizer, indicating the superiority of the latter.

4.3.3 Sauter Mean Diameter

A quantitative description of the spray quality is given by radial profiles of SMD at different axial locations in the spray as shown in figure 4.6 for ALR = 2.5 taken as the baseline case. Figure 4.7a shows the SMD profiles of the two atomizers at $Y = 1.0$ cm, the axial distance from the atomizer exit. For the FB atomizer, the peak SMD of $13 \mu\text{m}$ at the center of the spray decreases with increasing radius until a minimum of about $9 \mu\text{m}$ occurs at a radial distance of $r = 4$ mm. Thereafter, the SMD increases to reach a value of about $12 \mu\text{m}$ near the periphery of the spray located at $r = 8$ mm. An important observation is that the FB atomizer produces droplets of $9\text{--}13 \mu\text{m}$ or within the narrow range of $4 \mu\text{m}$. For the AB atomizer, the minimum SMD of $7 \mu\text{m}$ at the center increases gradually to about $20\text{--}25 \mu\text{m}$ at the periphery of the spray at $r = 12$ mm. Thus, the droplet SMD range is much wider ($>15 \mu\text{m}$), and the larger droplets penetrate farther to produce a wider spray as evidenced by the images presented in figure 4.6. Clearly, the FB atomizer offers unique features to distinguish it from the AB atomizer.

Figure 4.7b shows the SMD profiles for the two atomizers at a downstream location, $Y = 2.0$ cm. Results show trends similar to those observed at $Y = 1.0$ cm. The SMD profile of the FB atomizer no longer has a peak at the center indicating that this region undergoes significant interaction with the surrounding flow between $Y = 1.0$ and 2.0 cm to break down the larger droplets. The SMD still varies over a narrow range of $9\text{--}13 \mu\text{m}$ while the spray width increases to about $r = 10$ mm. The AB atomizer still demonstrates a wide range of SMDs, from around 6 to over $20 \mu\text{m}$, with the smallest droplets contained in the center of the spray, and the largest droplets confined to the periphery. Figure 4.7c shows that the SMD profile for the FB atomizer at $Y = 3.0$ cm flattens out even more than that at $Y = 2.0$ cm. The SMD profile for the AB atomizer at $Y = 3.0$ cm shows little to no difference from the profile at $Y = 2.0$ cm, i.e., smallest SMD at

the center, highest SMD in the periphery, and a wide range of SMDs varying from 6 μm to over 20 μm . Results show that the FB atomizer produces a spray with smaller droplets compared to the AB atomizer, except for the center region. Furthermore, the spray produced by the FB atomizer has smaller variations in SMD compared to those in the spray produced by the AB atomizer.

4.3.4 Droplet Diameter Distributions

Droplet diameter distributions at selected points are shown in figure 4.8 for ALR = 2.5. Figure 4.8a shows the droplet diameter distribution at $Y = 1.0$ cm, $r = 0.7$ cm, or toward the edge of the spray for the FB atomizer. The FB and AB atomizers produce, respectively, SMDs of 9.8 μm and 17.4 μm at this position. The FB atomizer shows a smaller range of droplet diameters, with the largest droplet diameter of about 30 μm for this case. However, the AB atomizer produces larger droplets with diameter up to 80 μm , resulting in a high SMD. Figure 4.8b shows the droplet distribution at the center of the spray at $Y = 3.0$ cm. At this position, the SMD for the FB atomizer is 9.2 μm while that for the AB atomizer is 6.6 μm . The FB atomizer's droplet distribution shows a higher percentage of larger droplets, and the maximum droplet diameter of 33 μm , compared with 25 μm for the AB atomizer. Figure 4.8c shows the droplet diameter distribution at $Y = 3.0$ cm, $r = 0.5$ cm. The SMD at this position was 9.3 μm for the FB atomizer and 10.3 μm for the AB atomizer. The profiles for both atomizers are very similar, but the AB atomizer produces more droplets of larger diameters.

Data presented in figure 4.8 are plotted in figure 4.9 in terms of cumulative mass fraction versus droplet diameter. Figure 9a shows that toward the edge of the spray, $Y = 1.0$ cm, $r = 0.7$ cm, droplets smaller than 30 μm comprise 100% of the liquid mass in the FB spray, but only 70% of the liquid mass in the AB spray, where the remaining mass is contained in larger (30–75

μm) droplets. Figure 4.9b shows that at the center of the spray at $Y = 3.0$ cm, a greater percentage of smaller droplets are produced by the AB atomizer. At $Y = 3.0$ cm, $r = 0.5$ cm, figure 4.9c shows that droplets smaller than $20 \mu\text{m}$ contain 95% of the liquid mass in the FB spray as compared to 85% of the liquid mass in the AB spray. These results demonstrate the superiority of the FB atomizer, especially in the outer regions of the spray.

4.3.5 Mean and RMS Velocities

Figure 4.10 shows the radial profiles of axial velocity for the two atomizers at $Y = 1.0$ cm, 2.0 cm, and 3.0 cm for $\text{ALR} = 2.5$. For the FB atomizer, the peak axial velocity at the center of the spray is 110 m/s in the near-field region ($Y = 1.0$ cm) as shown in figure 4.10a. In contrast, the AB atomizer shows a peak value of around 40 m/s at the spray center. This large difference in the peak axial velocity can be credited to the narrow spray produced by the FB atomizer, as discussed previously. Furthermore, the FB atomizer produces a dominantly axial flow, while the air swirler in the AB atomizer also transfers liquid momentum in the radial and tangential directions. Figure 4.10b shows the radial profiles of axial velocity for the two atomizers at $Y = 2.0$ cm. The peak axial velocity has decreased to 80 m/s and 35 m/s, respectively, for the FB and AB atomizers. These decreases in axial velocity are accompanied by the spray extending over a wider region at downstream locations. Figure 4.10c shows that at $Y = 3.0$ cm, the FB atomizer's peak axial velocity decreases to around 50 m/s, while that for the AB atomizer reduces to 30 m/s because of the radial growth of the spray.

Figure 4.11 shows the radial profiles of the RMS axial velocity at the aforementioned axial locations for $\text{ALR} = 2.5$. Figure 4.11a shows the peak RMS axial velocity of around 30 m/s for the FB atomizer, and 15 m/s for the AB atomizer. In both cases, the RMS axial velocity decreases slightly at the spray center such that the peak occurs close to the center. This result can

be explained by the isolation of the liquid jet's central region from the shear interaction with the gaseous phase in the near field of the atomizer exit. The RMS axial velocity for both atomizers decreases in the radial direction. The FB atomizer's higher RMS axial velocity can be attributed to the vigorous turbulent mixing inside the atomizer, expansion of air bubbles in the accelerating two-phase flow exiting the orifice, and higher axial velocity at the center. Figure 4.11b shows the radial profiles of the RMS axial velocity of the two atomizers at $Y = 2.0$ cm. The FB atomizer exhibits a peak RMS axial velocity of about 25 m/s, while the peak value for the AB atomizer is around 10 m/s. The dip in RMS axial velocity at the spray center is smaller at this axial location compared to that at $Y = 1.0$ cm. Further downstream at $Y = 3.0$ cm, figure 4.11c shows that the peak RMS axial velocity for the FB atomizer decreases to 16 m/s, while that for the AB atomizer reduces to 8 m/s. The FB atomizer no longer has a dip at the center, while this feature is still observed for the AB atomizer.

4.3.6 Effect of Air-to-Liquid Mass Ratio

Figure 4.12 shows the effect of ALR on the SMD, axial velocity, and RMS axial velocity for the FB atomizer. Although experiments were conducted for ALRs between 1.0 and 4.0 at intervals of 0.5, data in figure 12 are shown only for ALRs of 1.0, 2.5, and 4.0 to discuss the major trends. The radial profile of SMDs at $Y = 1.0$ cm in figure 4.12a show that the SMD decreases with increasing ALR. The SMD for the smallest ALR of 1.0 varies between 15 and 21 μm , while that for the highest ALR of 4.0 varies between 5 and 9 μm . All ALR values result in the W-shaped SMD radial profile, with higher values at the center and edges of the spray. Figure 4.12b shows that the SMD decreases at the downstream location of $Y = 3.0$ cm where the profile has changed to the U shape.

Figure 4.12c shows the radial profile of the axial velocity at $Y = 1.0$ cm. As expected, an increase in ALR or atomizing airflow rate increases the axial velocity, including the peak value at the spray center. For example, the peak axial velocity is 50 m/s for $ALR = 1.0$, and 120 m/s for $ALR = 4.0$. Figure 4.12d shows that the axial velocity decreases at the downstream location of $Y = 3.0$ cm because of the radial growth of the spray. At $Y = 3.0$ cm, the peak axial velocity decreases to 25 m/s for $ALR = 1.0$, and to 80 m/s for $ALR = 4.0$. All profiles show an increase in axial velocity with increasing ALR. Figure 4.12e shows the effect of ALR on the RMS axial velocity at $Y = 1.0$ cm. The RMS axial velocity increases with increasing ALR, with the peak RMS value varying from 15 to 35 m/s for ALRs of 1.0–4.0. A dip in the RMS axial velocity is observed at the center of the spray. Figure 4.12f shows the RMS axial velocity profiles at $Y = 3.0$ cm. The peak RMS axial velocity is about 24 m/s for $ALR = 4.0$, and it reduces to 8 m/s for $ALR = 1.0$. The RMS axial velocity increases with increasing ALR.

For comparison, figure 4.13 shows the effect of the ALR on the SMD, axial velocity, and RMS axial velocity of the AB atomizer at $Y = 1.0$ cm and 3.0 cm. Figure 4.13a shows that the SMD decreases with increasing ALR. The highest SMD of about 35 μm was measured at the periphery of the spray for $ALR = 1.0$. At an ALR of 4.0, although the profile is flatter than that at lower ALRs, a central area of higher SMDs is observed, indicating that the air has not fully penetrated the liquid core this close to the atomizer exit. The SMD profiles in figure 4.13b for $Y = 3.0$ cm show a clear trend of decreasing SMD with increasing ALR. Large SMDs of up to 40 μm are measured at the periphery of the spray for $ALR = 1.0$. All ALRs show SMDs of less than 10 μm at the center of the spray, and a wide range of droplet diameters in the transverse direction.

Figure 4.13c shows the effect of ALR on the axial velocity for the AB atomizer at $Y = 1.0$ cm. The axial velocity increases with increasing ALR, with a central peak of around 70 m/s for $ALR = 4.0$, and a central peak of 20 m/s for $ALR = 1.0$. The axial velocity decreases monotonically to zero toward the edge of the spray. At the downstream location of $Y = 3.0$ cm, the axial velocity profiles in figure 4.13d show a central peak of 20 m/s for $ALR = 1.0$, and 45 m/s for $ALR = 4.0$. Figure 4.13e shows the radial profiles of RMS axial velocity at $Y = 1.0$ cm. The peak value is 9 m/s for $ALR = 1.0$, and 25 m/s for $ALR = 4.0$. These profiles exhibit peak RMS axial velocities in the region of intense shear interaction and a depressed central region as noted previously. Increasing the ALR increases turbulence in the shear layer, and hence the peak RMS axial velocity. Profiles in figure 4.13f for $Y = 3.0$ cm show that the RMS axial velocity increases with an increase in ALR. These profiles exhibit a slight dip at the spray center, although the trend is less pronounced than that at $Y = 1.0$ cm.

4.4. Conclusions

Spray characteristics of a novel FB atomizer using water as the test fluid are presented and compared with a commercial AB atomizer. The spray characteristics were determined using laser sheet visualization and a 2D PDPA system. The FB atomizer produced a spray with both smaller droplets and a narrower range of droplet diameters. For the studied operating conditions, the SMD ranged between 7 to 25 μm for the FB atomizer, compared to 7–45 μm for the AB atomizer. The droplet diameter decreased with increasing ALR, but with a trend of diminishing returns. The peak axial velocity increased with increasing ALR, as expected. However, the peak axial velocity for the FB atomizer was much higher (because of the narrow spray) compared to that for the AB atomizer. The RMS axial velocities for the FB atomizer were also higher than those for the AB atomizer, indicating greater turbulence created by the former concept. These

favorable results with the FB atomizer were obtained with a lower pressure drop in the atomizing air line as compared to the AB atomizer. The superior performance of the FB atomizer results from the intense two-phase flow mixing at the tip of the liquid supply tube followed by the expansion of the gas at the atomizer exit causing breakdown of the surrounding liquid.

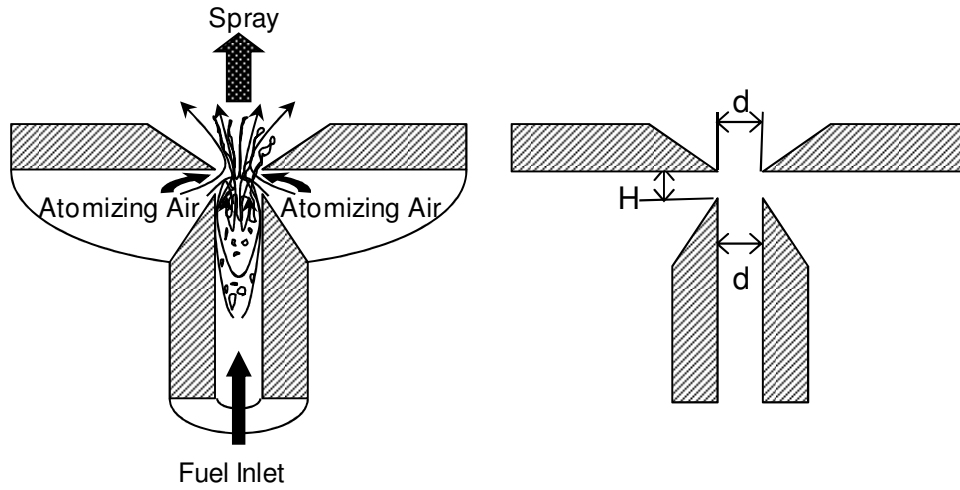


Figure 4.1 Flow Blurring (FB) injection concept

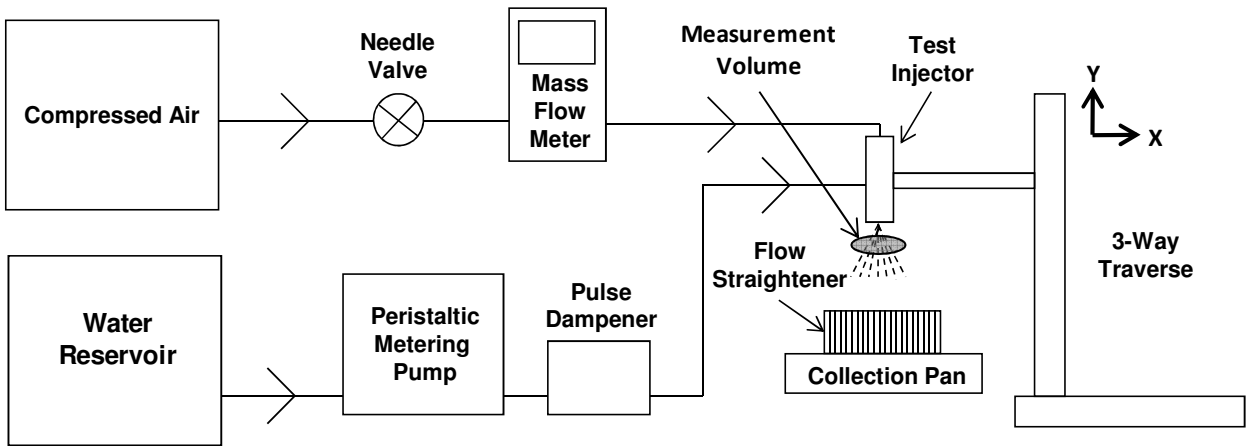


Figure 4.2 Spray setup schematic

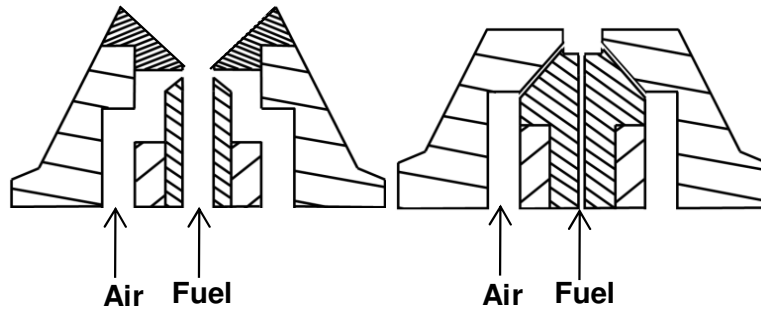
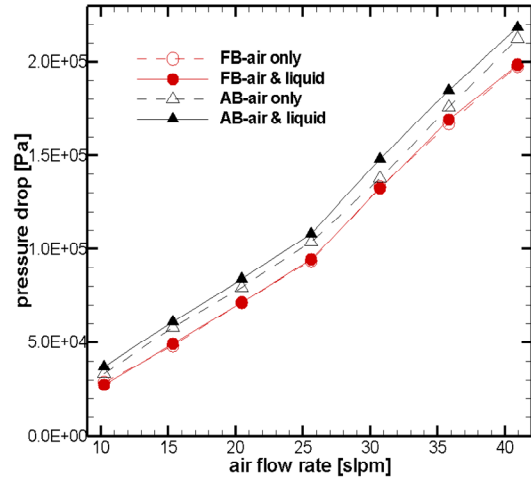
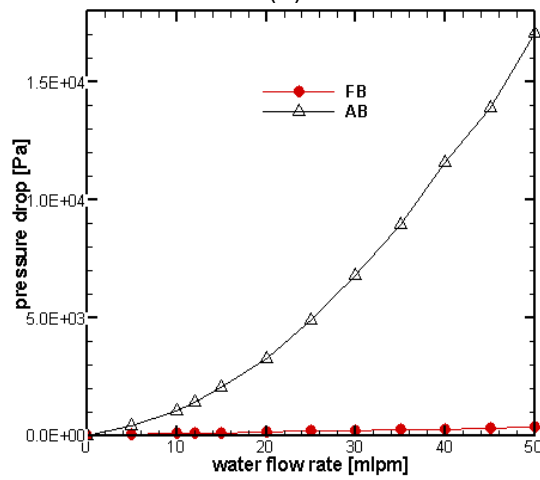


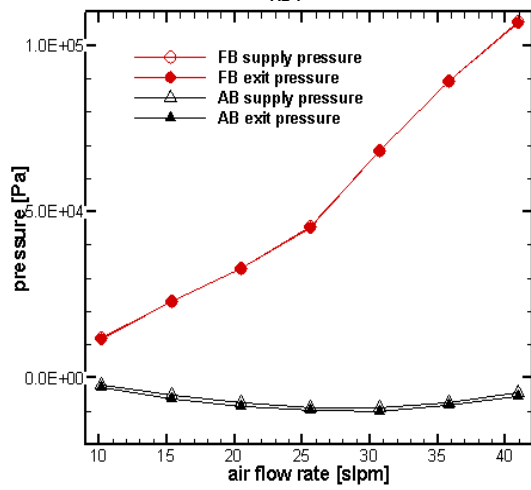
Figure 4.3 Detailed view of fluid path in: (a) Flow-Blurring (FB) injector; (b) Air-Blast (AB) injector



(a)



(b)



(c)

Figure 4.4 Pressure data: (a) atomizing air pressure drop; (b) liquid pressure drop without atomizing airflow; (c) liquid supply and exit pressures

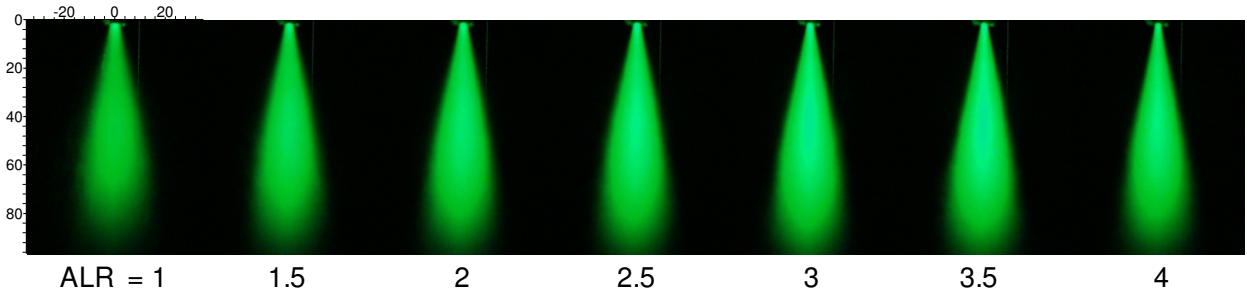


Figure 4.5 Laser sheet spray images for FB atomizer (water, 12.0 mlpm) for ALRs ranging from 1.0 to 4.0 (dimensions in mm)

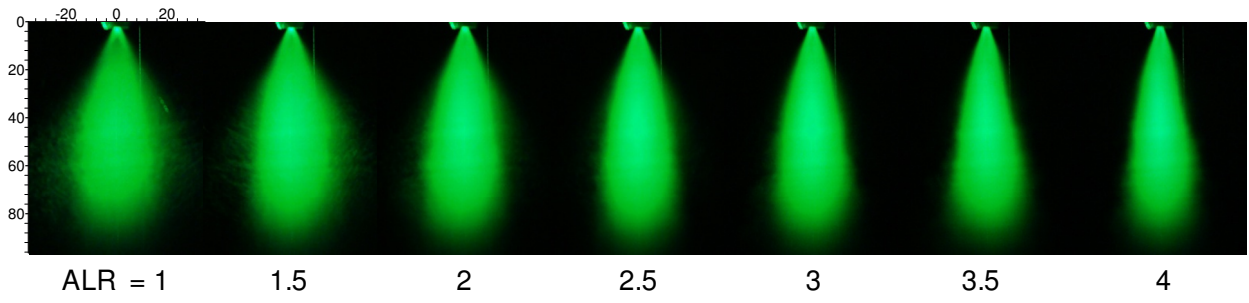
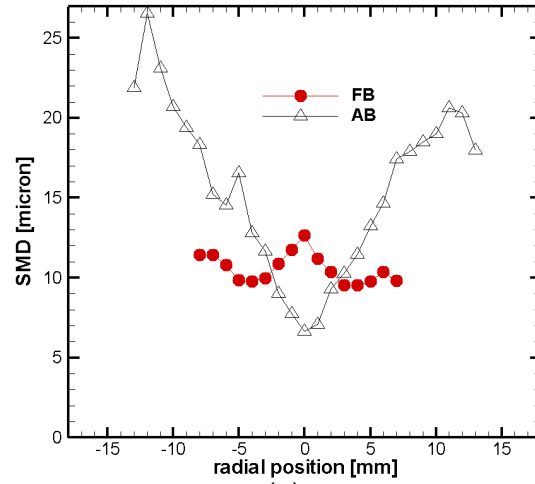
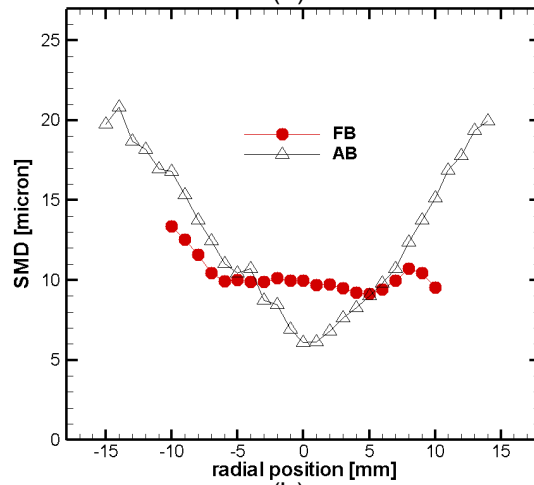


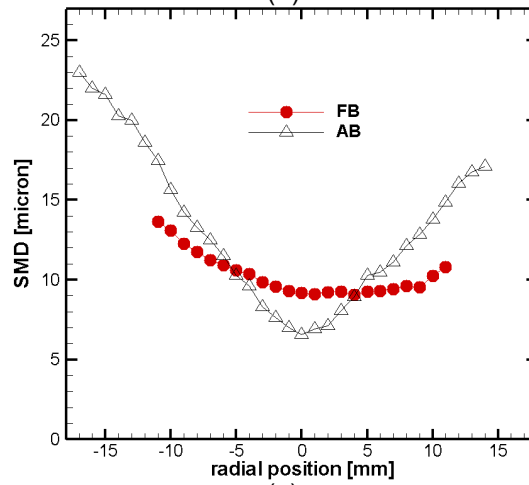
Figure 4.6 Laser sheet spray images for AB atomizer (water, 12.0 mlpm) for ALRs ranging from 1.0 to 4.0 (dimensions in mm)



(a)

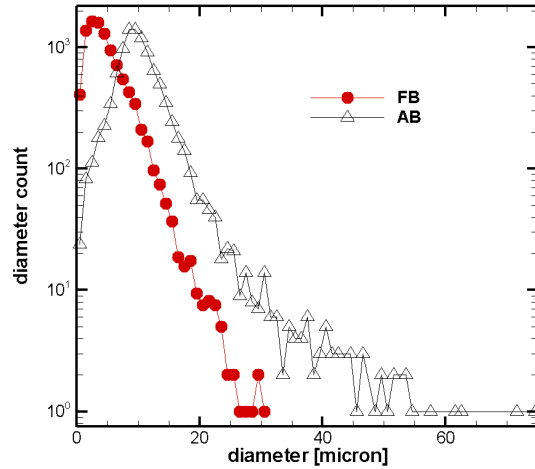


(b)

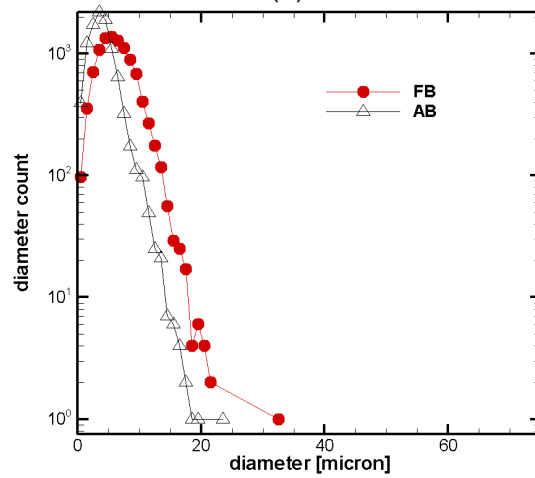


(c)

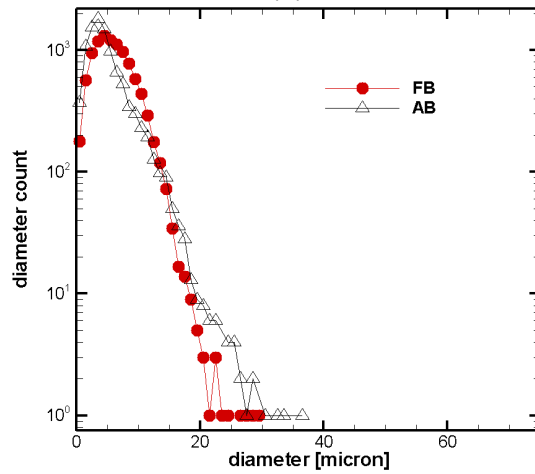
Figure 4.7 SMD for FB and AB atomizers: (a) $Y = 1.0$ cm; (b) $Y = 2.0$ cm; (c) $Y = 3.0$ cm



(a)



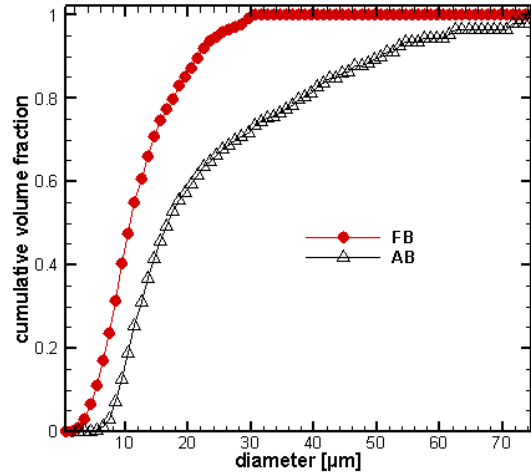
(b)



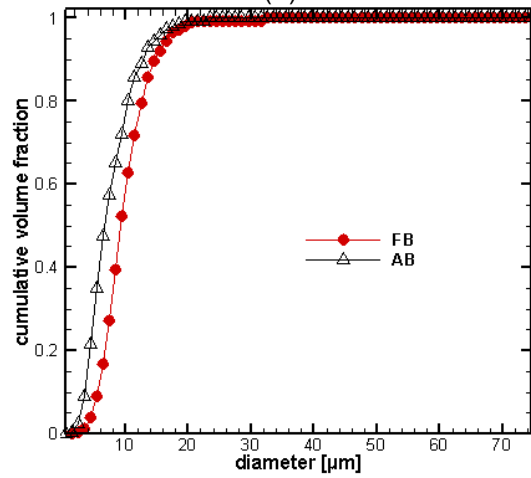
(c)

Figure 4.8 Droplet diameter distributions for FB and AB atomizers: (a) $Y = 1.0$ cm, $r = 0.7$ cm;

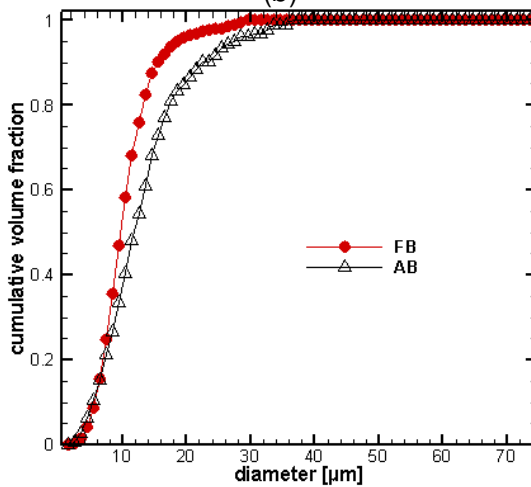
(b) $Y = 3.0$ cm, $r = 0.0$ cm; (c) $Y = 3.0$ cm, $r = 0.5$ cm



(a)

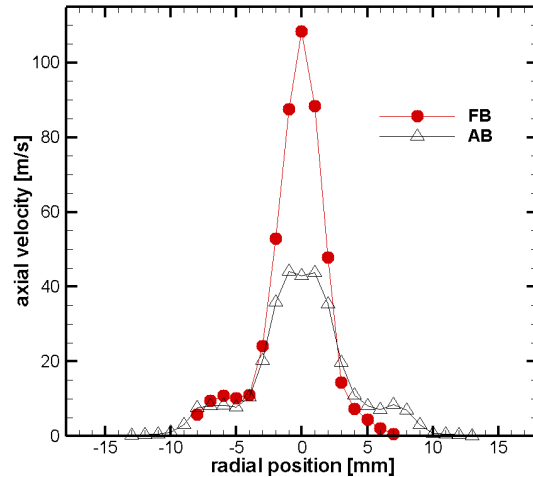


(b)

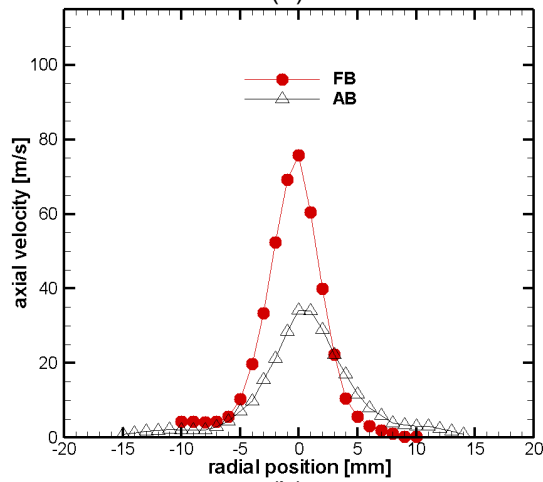


(c)

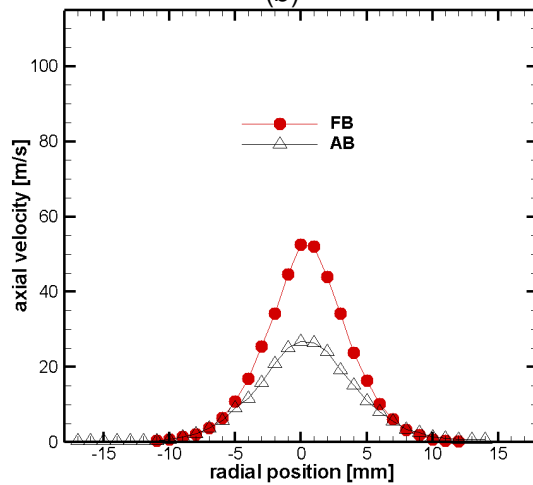
Figure 4.9 Cumulative volume fraction distributions for FB and AB atomizers: (a) $Y = 1.0$ cm, $r = 0.7$ cm; (b) $Y = 3.0$ cm, $r = 0.0$ cm; (c) $Y = 3.0$ cm, $r = 0.5$ cm



(a)



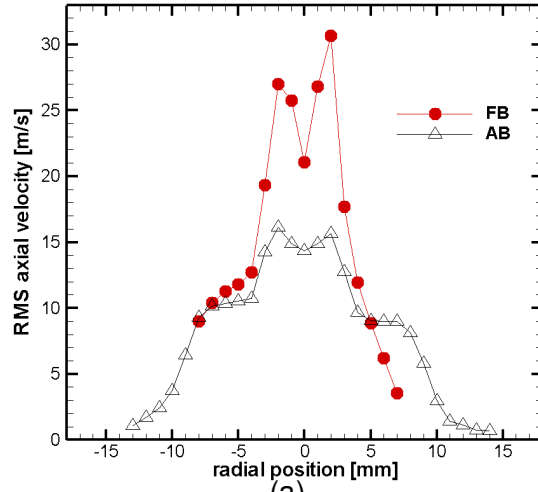
(b)



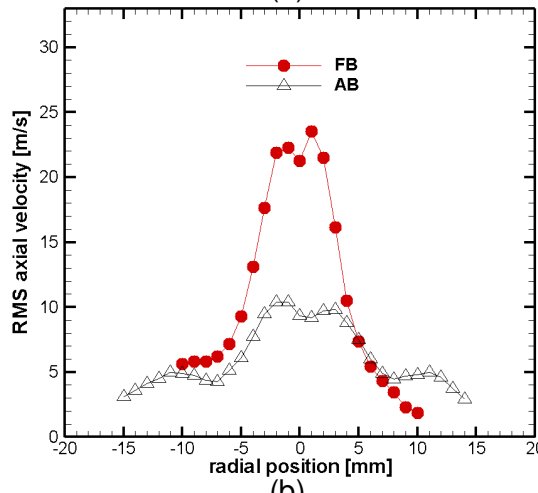
(c)

Figure 4.10 Axial velocity profiles for FB and AB atomizers: (a) $Y = 1.0$ cm; (b) $Y = 2.0$ cm; (c)

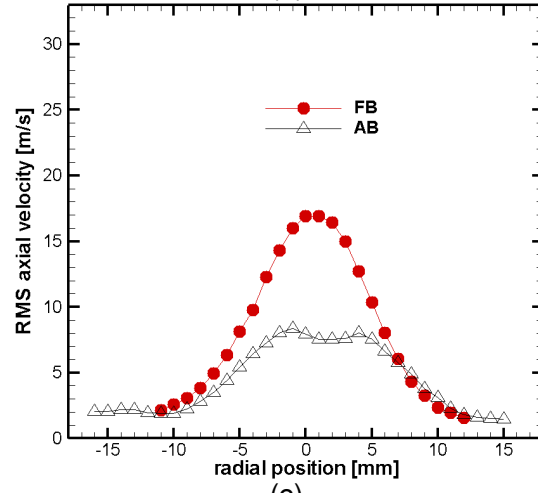
$Y = 3.0$ cm



(a)



(b)



(c)

Figure 4.11 RMS Axial velocity profiles for FB and AB atomizers: (a) $Y = 1.0$ cm; (b) $Y = 2.0$ cm; (c) $Y = 3.0$ cm

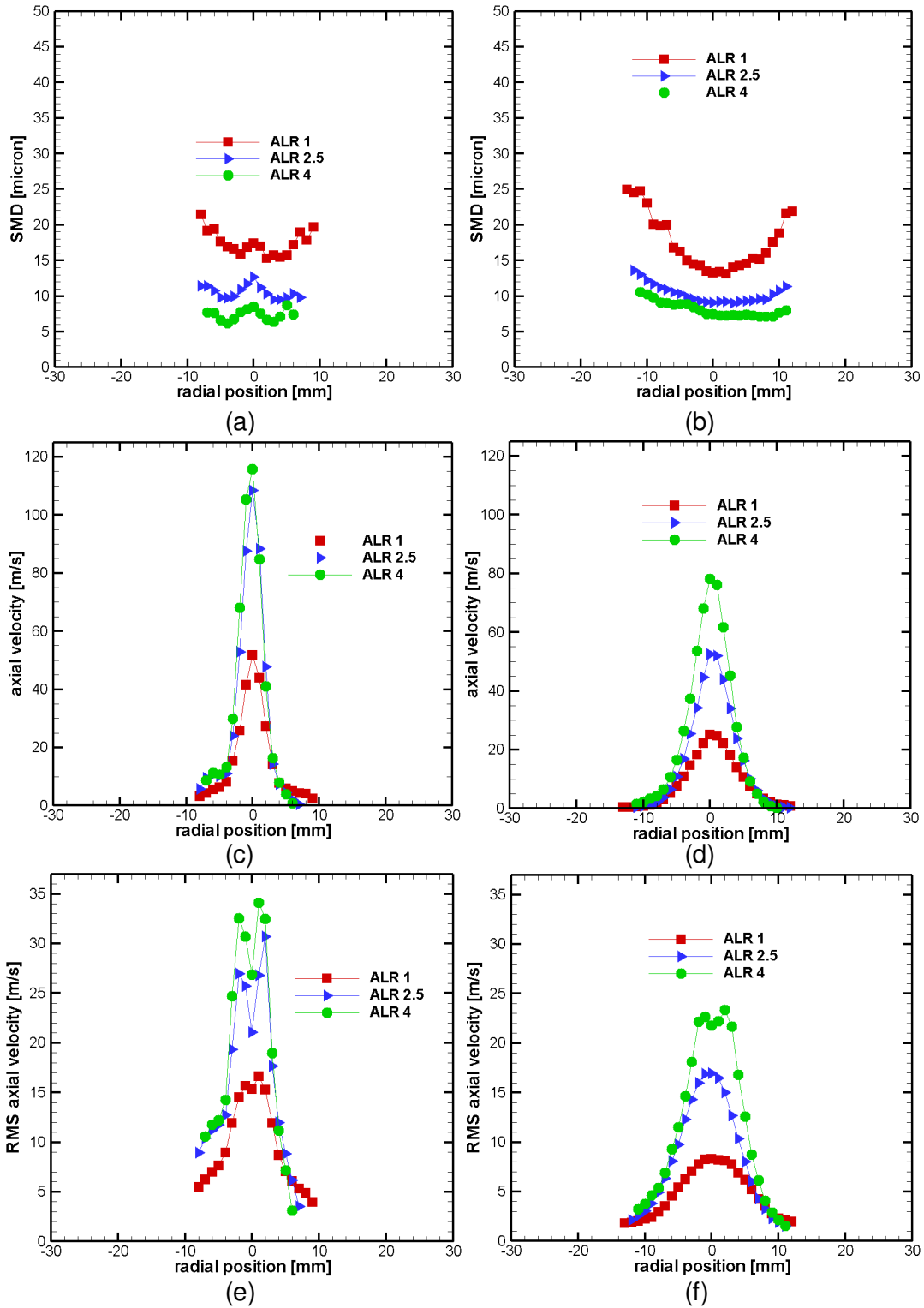


Figure 4.12 Effect of ALR on SMD, axial velocity, and RMS axial velocity for FB injector: (a), (c), (e) $Y = 1.0$ cm; (b), (d), (e) $Y = 3.0$ cm

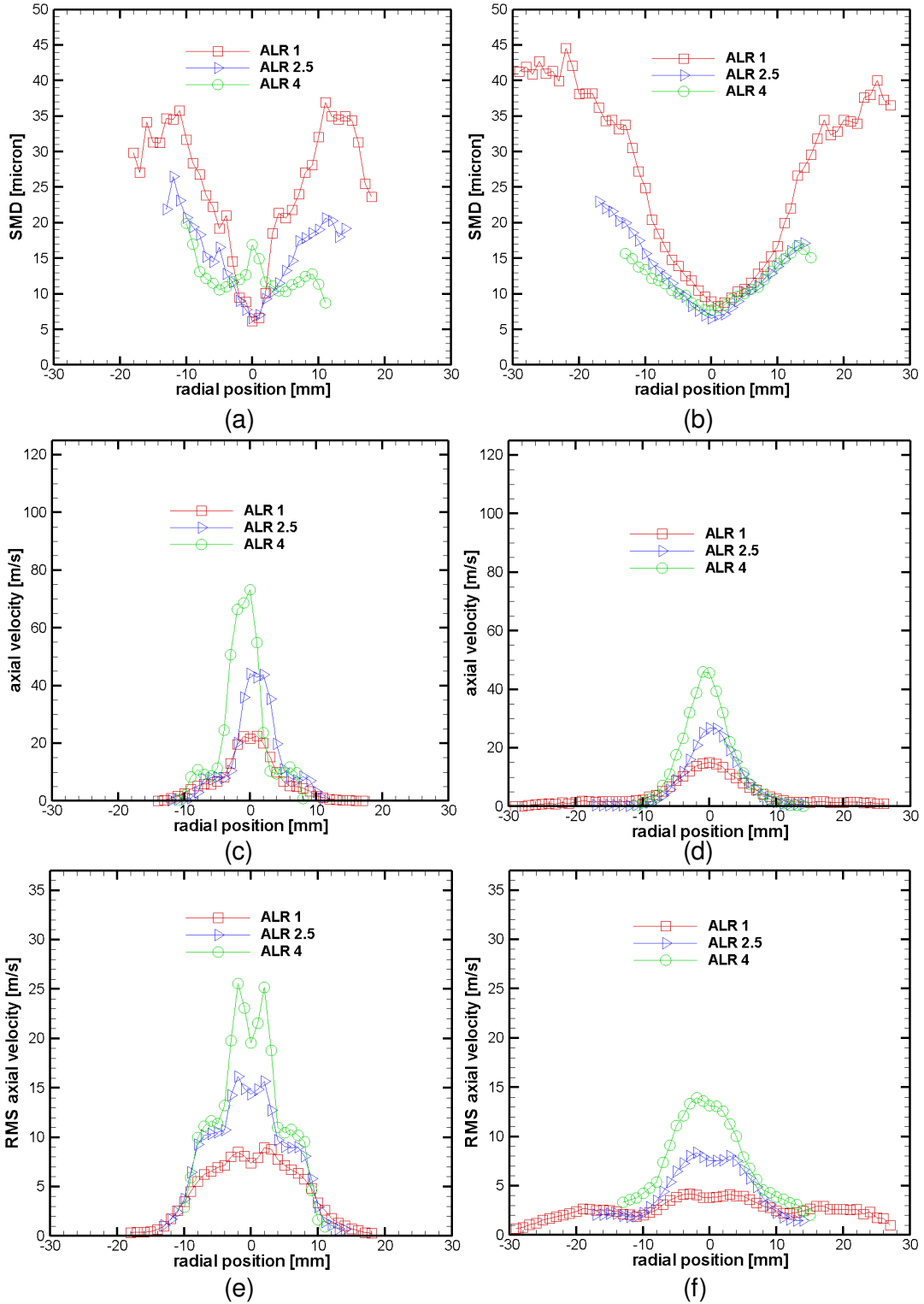


Figure 4.13 Effect of ALR on SMD, axial velocity, and RMS axial velocity for AB injector: (a), (c), (e) $Y = 1.0$ cm; (b), (d), (e) $Y = 3.0$ cm

CHAPTER 5

FLOW AND DROPSIZE MEASUREMENTS IN NON-REACTING BIODIESEL AND VEGETABLE OIL SPRAYS

5.1 Background

Biofuels are expected to play an increasingly important role in meeting future energy needs of the world [Tyner, 2008, Balat, 2007; Duncan, 2003]. Effective utilization of biofuels requires the fundamental understanding of biofuel combustion. Although biofuels exist in all phases, combustion of liquid biofuels, such as biodiesel, Fischer-Tropsch (FT) fuels, and bio-oils is pertinent to power generation and propulsion systems [Moliere, 2005; Lefebvre and Ballal, 2010; Bolszo and McDonnell, 2009]. Bio-oils from plant or animal matter are processed to produce biodiesels or FT fuels to meet the requirements of the combustion system. For example, long chain bio-oils undergo transesterification to produce biodiesels that are easier to atomize in the combustor. Typical fuel injectors are constrained by the high viscosity and unfavorable physical properties (e.g., volatility and surface tension) of bio-oils. Since production of biodiesels and FT fuels incurs processing costs, the direct combustion of the source fuel offers significant economic benefits. Fuel atomization can be improved by heating bio-oils or blending them with low viscosity fuels, but these techniques also require additional energy input, raising the fuel cost. Fuel injectors allowing clean combustion of the source fuel are therefore desirable to reduce the cost associated with biofuel utilization.

Gas turbine combustion systems generally utilize an air-blast (AB) or air-assist injector to break up the fuel jet into a spray by a co-flow of atomizing air [Rizk and Lefebvre, 1984; Han et

al, 2001; Tsai and Viers, 1992; Lefebvre, 1989; Rizk and Mongia, 1992; Zheng et al, 1997]. The high relative velocity between the two phases creates shear layer instabilities that grow to deform the liquid phase, causing fuel ligaments to break-off and disintegrate into droplets. High fuel viscosity and/or surface tension suppresses the instabilities, which results in large droplets that burn in diffusion mode to produce high concentrations of carbon monoxide (CO), nitric oxides (NO_x), and soot. Effervescent atomization (EA) has been proposed to overcome limitations resulting from variations in the physical properties of different fuels. In EA, fuel and air are mixed to form a two-phase flow upstream of the injector orifice. As this mixture passes through the injector orifice, the pressure decreases rapidly to cause bubbles in the gas phase to expand. Breakup of expanding gas bubbles destabilizes the surrounding liquid phase, creating a spray with fine fuel droplets. However, the EA process has not been adopted in the gas turbine industry because of several drawbacks: (1) the atomizing air must be supplied at a high pressure to match the fuel supply pressure in the mixing chamber, and (2) the two-phase flow in the channel leading to the injector orifice can cause detrimental flow instabilities [Sovani et al, 2001].

Recently, we have introduced the novel Flow-Blurring (FB) atomization technique, first reported by Gañán-Calvo, for liquid fuel combustion systems [2005, Rossell-Llompart and Gañán-Calvo 2008]. Gañán-Calvo reported that, for a given energy input, the FB technique results in “five to fifty times” more droplet surface area as compared to a plain jet AB atomizer [2005]. In a laboratory scale combustion study, for a given atomizing airflow rate, the FB injector decreased NO_x and CO emissions in kerosene and diesel flames by 3 to 5 times as compared to those from a commercial AB injector [Panchasara et al 2009a]. Measurements in a water spray by a Phase Doppler Particle Analyzer (PDPA) system showed that the FB injector

produces finer droplets with a narrow range of droplet diameters as compared to the AB injector [Simmons et al, 2009; Simmons and Agrawal, 2011]. Moreover, the FB injector required a lower atomizing air supply pressure than the AB injector. Emissions measurements (uncertainty of ± 2 ppm) in figure 5.1 demonstrate that the FB injector also facilitates clean combustion of high viscosity bio-oils [Simmons et al, 2008]. Legends in figure 5.1 show the heat release rate and calculated adiabatic flame temperature (T_{ad}) for each test condition. Note that the data in Fig. 1 were acquired at the exit plane of an approximately 46 cm long quartz combustion chamber, with a volume of about 2300 cm³ and residence time of 0.92s for the conditions tested. Diesel and soybean oil (vegetable oil or VO) flames (shown in Simmons et al, 2008) were similar in appearance and, as figure 5.1 shows, they also resulted in comparable NO_x and CO emissions.

The superior performance of the FB injector stems from the two-phase mixture based atomization, similar to the EA process but without its inherent drawbacks. Figure 5.2 illustrates the working principle of the FB injector consisting of a fuel tube of inside diameter 'd' separated by distance 'H' from the injector orifice, also of diameter 'd'. For large separation distances ($H \sim d$), the atomizing air co-flows around the fuel jet, similar to that in an AB injector. However, for $H < d/4$, the atomizing air flow penetrates a short distance upstream into the fuel tube to create a two-phase mixture at the tip of the fuel tube. This two-phase mixture undergoes sudden decrease in pressure while exiting through the injector orifice. Consequently, air bubbles in the flow expand and eventually collapse to breakdown the surrounding fuel into a spray of fine droplets. The FB atomization is similar to the EA process, but the two-phase mixing occurs at the tip of the fuel tube, which requires a lower supply pressure for the atomizing air flow and prevents two-phase flow instabilities.

In this study, the cold spray of VO (soybean oil representing bio-oils) produced by the FB injector is characterized for the first time. Cold spray is considered as the first step to understand the injector performance, and also to obtain baseline data necessary to develop and validate computational models of the FB injector. Present study can also lead to future research to ascertain how fuel's physical properties affect reacting sprays by using a combination of experimental and computational studies. For reference, Table 1 lists the key physical properties of VO and diesel fuel at ambient conditions [Panchasara et al, 2009b; Schwab et al, 1988; fuel table, 2011; specific heat table, 2011]. The kinematic viscosity of VO is nearly 13 times that of the diesel. The VO also has higher density and surface tension compared to the diesel. For a given heat release rate, VO requires greater mass flow rate because of its lower heating value compared to the diesel. The specific heat for VO is lower than that of the diesel. The two fuels also have significantly different volatility curve as discussed in Panchasara et al, 2009b. In this study, the flow field and droplet diameter distributions at various radial locations are measured in cold VO and diesel sprays. Description of the experimental setup, results and discussions, and conclusions of the study are presented in the following sections.

Table 5.1 Physical properties of fuels

| Property | Diesel | VO |
|--|---------------|----------------|
| Molecular Weight [kg/kmol] | 142.2 | 277.9 |
| Density at 25°C [kg/m ³] | 834.0 ± 8.3 | 925.0 ± 9.2 |
| Viscosity at 25°C [mm ² /sec] | 3.88 ± 0.02 | 53.74 ± 0.22 |
| Surface Tension at 25°C [mN/m] | 28.2 ± 0.6 | 30.1 ± 0.6 |
| Specific Heat at 15.6°C [kJ/kgK] | 1.800 | 1.005 to 1.382 |
| LHV [MJ/m ³] | 37,198 | 34,225 |

5.2 Experimental Setup

Figure 5.3 shows a schematic diagram of the experimental setup consisting of a swirl-stabilized combustor operated at atmospheric pressure. The test apparatus in figure 5.3 replicates the key features of gas turbine combustion systems, although present measurements were taken at ambient temperature and pressure. A commercial AB injector (Delavan Model 30609-2) was retrofitted to create the FB injector with fuel tube ID, $d = 1.5$ mm and $H = 0.35$ mm. Liquid fuel enters the injector assembly through a supply tube perpendicular to another tube providing the atomizing air flow. Primary air enters the apparatus through a plenum filled with marbles to breakdown vortical structures. Then, the primary air flows through an annulus around the injector assembly, before passing through a swirler located upstream of the measurement volume. Flow streams were vertically oriented, and thus, safely discarding the fuel in the cold spray was a major challenge. In this study, a custom-designed, methane-based flare system was placed downstream of the spray to burn the majority of the fuel spray. The combustion products were discarded to the ambient through an exhaust duct.

Compressed air from an air compressor was regulated to a supply pressure of around 4 bar, filtered to remove any moisture, and then split into primary and atomizing air lines. Primary air was controlled by a needle valve and measured by a laminar flow element with an uncertainty of ± 5 standard liters per minute (slpm). The atomizing air flow rate was controlled and metered by a Sierra Instrument Smart-Trak mass flow controller with an uncertainty of ± 0.5 slpm. Liquid fuel was supplied by high performance metering pump (Cole-Parmer Model EW-77250-62) with an uncertainty of ± 0.25 % of the reading. Supply pressure in the fuel and atomizing air lines was measured using Omega model PX303 pressure transducers at locations depicted in figure 5.3.

Measurements of droplet diameter and velocity were acquired by the calibration free PDPA technique. Two pairs of beams, at 488 nm and 514.5 nm wavelength, intersect at the measurement volume. A Bragg cell is used to frequency shift one of the beams in each pair, to create a moving fringe pattern at the beam crossing. A droplet passing through the measurement volume scatters light to form an interference fringe pattern, which is detected by the receiver probe oriented at 135° angle from the transmission probe. Acquired signal is processed by fast Fourier transform (FFT) algorithm to obtain the dominant frequency, which is proportional to the droplet velocity. The droplet diameter is determined from the phase shift obtained by comparing signals from two detectors.

All of the experiments were conducted for a total air flow rate of 150 slpm. The split of total air flow rate into primary air and atomizing air flow rates was manipulated to vary the Air-to-Liquid mass Ratio (ALR) through the injector. Experiments with diesel were performed with a fixed fuel flow rate of 12 milliliters per minute (mlpm), providing heat release rate of approximately 7.4 kW. Since the heating values of diesel and VO are different, experiments with VO were conducted with (1) fuel flow rate of 12 mlpm (same as diesel) denoted as “VO, constant V,” and (2) heat release rate of 7.4 kW (same as diesel) denoted as “VO, constant Q.” Experiments with VO were conducted for ALR of 2.0 and 4.0. The coordinate system in figure 5.3 pinpoints the origin at the center of the injector exit. The coordinate Z represents the axial distance from the injector exit, and the coordinate R represents the transverse distance from the injector centerline. All measurements in the paper are presented at axial location, $Z = 20$ mm. Previous studies in cold sprays using water as the injected liquid have shown similar trends in the axial direction because of the absence of the heat release [Simmons et al, 2008; Simmons and Agrawal, 2011].

5.3 Results and Discussion

5.3.1 Pressure Measurements

Pressure drop in the atomizing air and fuel supply lines is important for practical operation of the injector. Figure 5.4 shows that the pressure drop in the fuel and atomizing air lines is independent of the fuel (diesel or VO). The pressure drop for the two VO cases is also the same. An increase in the atomizing air flow rate increases the pressure drop in fuel and atomizing air lines, as expected. Increasing the atomizing air flow rate increases the flow resistance in the fuel-air mixing process at the tip of the fuel tube. Evidently, the pressure drop in the two-phase mixing region is much greater than the frictional loss in the fuel supply tube since the total pressure drop is independent of the physical properties of the fuel.

5.3.2 PDPA Measurements

Figure 5.5 shows the radial profiles of Sauter Mean Diameter (SMD) for VO and diesel sprays at $ALR = 2.0$. For both fuels, the SMD is the highest at the center and it decreases gradually towards the edge of the spray. Both VO sprays exhibit an increase in the droplet diameter at the periphery of the spray. The droplet diameter in the VO sprays varies between 32 and 55 μm . Both VO sprays produce similar SMD profiles, indicating negligible effect of the fuel flow rate within the narrow range considered. The diesel spray contains finer droplets with diameter varying approximately from 25 to 40 μm . Clearly, the cold spray produced by the FB injector is affected by the fuel properties, especially in the center region. The relative insensitivity of fuel properties on flame emissions presented in figure 5.1 therefore points to the importance of the heat release in the reacting spray.

Each data point in figure 5.5 represents a droplet diameter distribution shown, for example, in figure 5.6 for spray center ($R = 0.0$ mm) at $Z = 20$ mm. The SMD for the two VO

sprays is nearly the same (54.5 and 54.2 μm), while the SMD for the diesel spray is 39.0 μm . Both VO sprays produce similar droplet diameter distributions, with peak diameter of about 160 μm . The number count of larger droplets is small, but the greater liquid mass contained in these droplets significantly increases the SMD. The two VO distributions are similar, indicating that the atomization process is dependent mainly upon the ALR, rather than the total flow rate through the injector. Figure 5.6 shows that the largest droplet diameter in the diesel spray is about 125 μm , and the number count of larger droplets in the diesel spray is smaller than that in VO sprays. Figure 5.7 compares droplet diameter distributions for different test cases near the edge of the spray, i.e., $R = 8.0$ mm, and $Z = 20.0$ mm. At this location, SMD for VO sprays is about 36 μm and that for diesel spray is 32 μm . Interestingly, droplet diameter distributions for both fuels are similar at this location.

Results in figures 5.6 and 5.7 are re-plotted in terms of cumulative fuel volume distributions and shown, respectively, in figures 5.8 and 5.9. The fuel volume distributions for the two VO sprays are nearly identical. At $R = 0$ mm, $Z = 20$ mm, droplets under 50 μm contain about 30% of the total mass in the VO spray but nearly 70% of the total mass in the diesel spray. The difference between fuels is much smaller at the edge of the spray, where droplets under 50 μm contain about 65% and 80% of the total mass, respectively, in VO and diesel sprays. These results show that the VO spray resembles the diesel spray, although larger droplets are also produced in case of the former. Heat release in a reacting spray can be expected to pre-vaporize these large droplets to limit the diffusion mode burning responsible for high NO_x and CO emissions.

Next, the flow field measurements are presented to discern the relationship with droplet diameter distributions in the spray. Measurements assume equilibrium between the gas and

liquid phases, which may not be valid in regions with large diameter droplets. Figure 5.10 shows the radial profiles of the mean axial velocity at $Z = 20$ mm for different sprays with $ALR = 2.0$. The profiles depict a jet-like distribution, with axial velocity peaking at the center and decreasing in the transverse direction to reach nearly zero value around $R = 10$ mm. For $ALR = 2.0$, the total flow rate (fuel plus atomizing air) for the two VO experiments is different, which results in peak axial velocity of 70 and 85 m/s, respectively, for constant V and constant Q cases. The peak axial velocity in the diesel spray is 50 m/s since, in this case, a smaller atomizing air flow rate is required to obtain $ALR = 2.0$. The high velocity center region of the spray results in droplets of larger SMD, as shown in figure 5.5. Thus, higher axial flow velocity results in poor two-phase mixing at the center of the fuel tube tip. Conversely, the low-velocity, boundary layer region of the fuel tube can be expected to produce an annular region of intense two-phase mixing. Radial profiles of turbulence intensity, defined as the ratio of RMS and mean axial velocities (of fuel droplets), in figure 5.11 support this hypothesis. For all cases, the turbulent intensity is minimum at the center and it peaks to a large value of about 4.0 at $R = 10$ mm, where the SMD in VO sprays is the minimum. Turbulence intensity profiles for both fuels nearly overlap each other. These results suggest that the two-phase mixing at the tip of fuel tube is confined to an annular region, which eventually results in high turbulence to produce small droplets in the spray.

In the present study, the primary air passes through a swirler to introduce the swirling flow around the FB injector. Radial profiles of swirl velocity for both fuels are shown in figure 5.12 for $ALR = 2.0$. The swirl velocity is nearly zero at the spray center and it peaks to about 5 m/s at $R = 5$ mm, although profiles also show a slight asymmetry. Since the primary air flow introduces the swirl, the swirl velocity is nearly independent of the fuel properties. Primary air

flow is also responsible for turbulence in the swirl flow, which is depicted by the RMS swirl velocity profiles in figure 5.13. The RMS swirl velocity peaks at the center and decreases gradually in the transverse direction. These trends pertained to a nearly constant turbulence intensity profile across the spray (not shown here), except at the center. The swirl flow is expected to introduce secondary atomization to further disintegrate the fuel droplets produced by the FB injector. This statement is substantiated by figure 5.5 showing droplets of smaller SMDs in the regions of large swirl velocity.

Droplet diameter and axial velocity measurements were used to obtain the radial profile of fuel flow rate according to equation 5.1:

$$\text{flow}_R = \text{flux}_R * \pi * R * \Delta R \quad (5.1)$$

where flow_R is the fuel volume flow rate through the represented annular space, flux_R is the measured volume flux at radial location R , and ΔR is radial separation between measurement points. Note that the term flux_R is derived from many experimental parameters containing large uncertainty, especially the measurement of the probe volume. Thus, the results presented next must be interpreted only qualitatively. Figure 5.14 shows several interesting trends: (1) the fuel flow rate through the center of the spray containing the largest droplets is nearly negligible, (2) most of the fuel flows through the annular region between $R = 5$ and 10 mm, where the SMD of fuel droplets is smaller, and (3) the fuel flow rate in the outer region of the spray ($R > 10$ mm) is rather small. Even though the FB injector produces fuel dependent SMD profiles (see Fig. 5), the spray region with the majority of the fuel flow rate has nearly the same SMD for both fuels. This result is expressed quantitatively in terms of the average SMD (weighted by fuel flow rate) calculated using equation 5.2:

$$\text{average SMD} = \Sigma (\text{SMD}_R * \text{flow}_R / \text{total flow}) \quad (5.2)$$

where the subscript R pertains to the transverse location and the ‘total flow’ is the total volumetric fuel flow rate at the axial plane. Equation 5.2 results in average SMD of 34, 40, and 38 μm , respectively, for diesel, VO constant V, and VO constant Q sprays. Thus, the average SMD in the spray produced by the FB injector is relatively independent of the fuel, which clarifies the similarity between the emissions profiles of VO and diesel flames in figure 5.1.

5.3.3 Effect of ALR

Since droplet diameter in the spray is affected by the atomizing air flow rate, measurements were also obtained for ALR = 4.0. However, detection in the diesel spray was impaired because of the very fine droplets produced. The optical components of the PDPA system resulted in the lowest detectable droplet diameter of about 4 μm . It is believed that a very significant portion of droplets in diesel spray at ALR = 4.0 are smaller than this threshold because of the improved atomization. Radial profiles of SMD for VO sprays at ALR = 2.0 and 4.0 are compared in figure 5.15. Data are presented for VO ‘constant Q’ case only since ‘constant V’ and ‘constant Q’ VO cases produced similar results, as shown in the previous section. Results show that the droplet diameter in the center region of the spray ($R < 5.0$ mm) is nearly independent of the ALR. This finding is attributed to the poor two-phase mixing at the center of the fuel tube, where the fuel jet velocity is the highest. Figure 5.15 shows that the SMD decreases significantly in the outer region of the spray for the higher ALR.

The effect of ALR on the mean axial velocity in VO sprays is shown in figure 5.16. The peak mean axial velocity of 80 m/s for ALR = 2.0 increases to 120 m/s for ALR = 4.0. The mean axial velocity increases with increase in the atomizing air flow rate through the injector. Figure 5.17 shows the radial profiles of turbulence intensity for ALR = 2.0 and 4.0. The two profiles nearly overlap each other in the center region, where two-phase mixing is minimal.

However, towards the edge of the spray ($R > 8$ mm) the turbulence intensity is higher for the higher atomizing air flow rate, i.e. $ALR = 4.0$.

Radial profiles in figure 5.18 show that increasing the ALR increases the swirl velocity with peak values of about 9 m/s for $ALR = 4.0$. The RMS swirl velocity also increases as ALR is increased from 2.0 to 4.0 (see figure 5.19). The RMS swirl velocity peaks to over 7 m/s at the center of the spray. Finally, figure 5.20 shows the axial volume flow rate of VO for $ALR = 2.0$ and $ALR = 4.0$, estimated using equation 5.1. The center region of the spray contains negligible fuel flow rate, while the peak fuel flow rate occurs at nearly the same transverse location for $ALR = 2.0$ and 4.0. Higher ALR results in a smaller peak, signifying improved atomization with a greater fraction of small droplets below the detection limit of the PDPA. Using equation 5.2, the average SMD for $ALR = 4.0$ was approximately 33 μm compared to that of 38 to 40 μm for $ALR = 2.0$.

5.4 Conclusions

Recent experiments have shown that the FB atomizer results in clean combustion of straight VO with CO and NO_x emissions similar to the diesel fuel [Simmons et al, 2008]. In support of these results, the present study at non-reacting conditions found that the FB injector produces VO spray with weighted SMD at an axial plane similar to that of the diesel spray. For $ALR = 2.0$, the weighted SMD for diesel and VO sprays was, respectively, 34 μm and 38 μm . The weighted SMD for VO spray at $ALR = 4.0$ decreased to 33 μm . The larger droplets in the VO sprays are confined to the center region where the fuel flow rate is very small. These regions are also expected to benefit the most from thermal feedback from the flame under reacting conditions. This study shows that the pressure drop in the atomizing air and liquid fuel lines of

the FB injector is the same for VO and diesel fuels. Cold spray data presented in this study can be used to develop and validate computational models of the FB injector using alternative fuels.

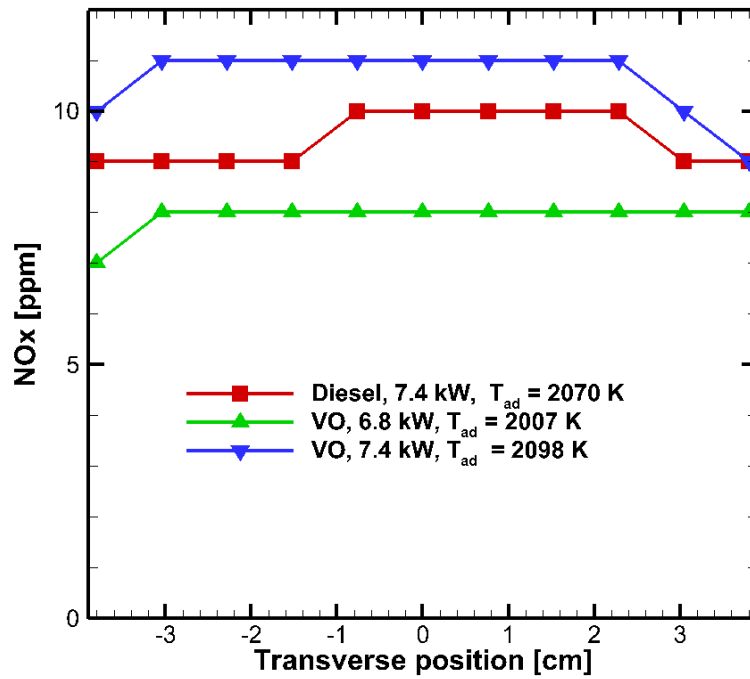
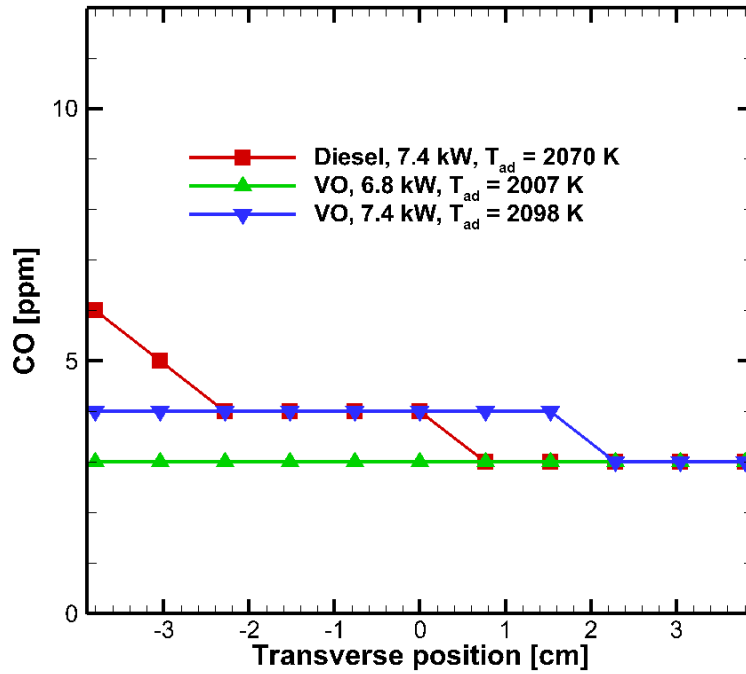


Figure 5.1 VO and diesel CO and NO_x emissions

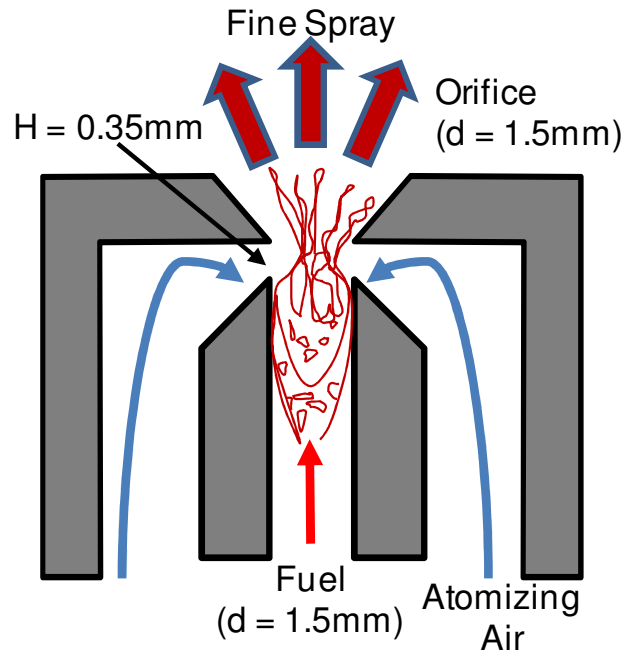


Figure 5.2 FB injection concept

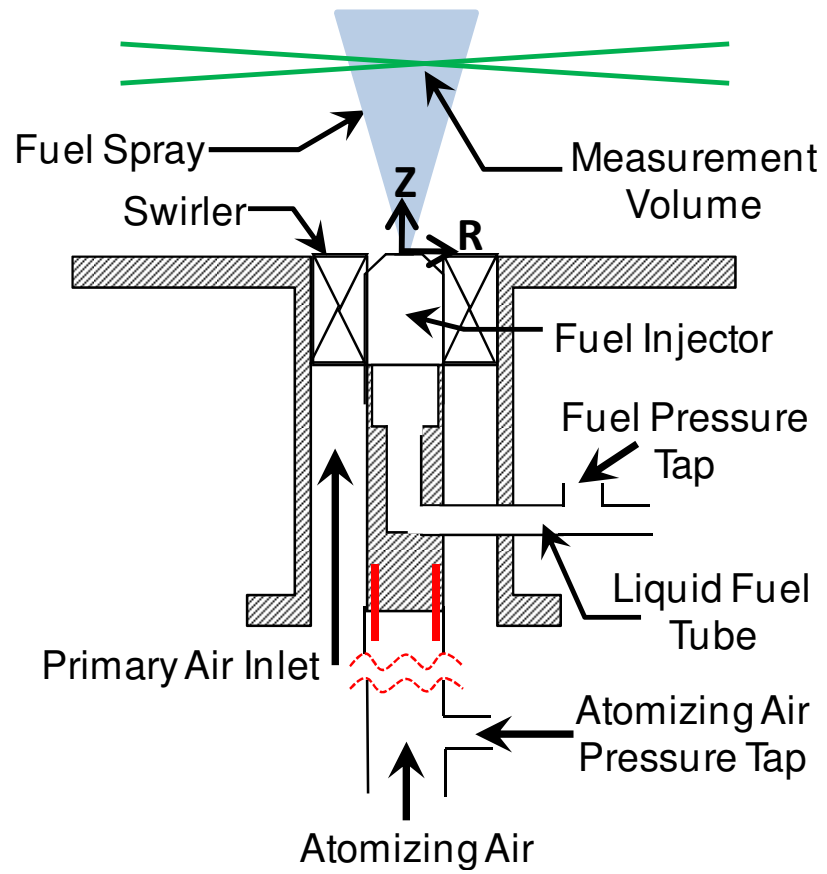


Figure 5.3 Experimental setup

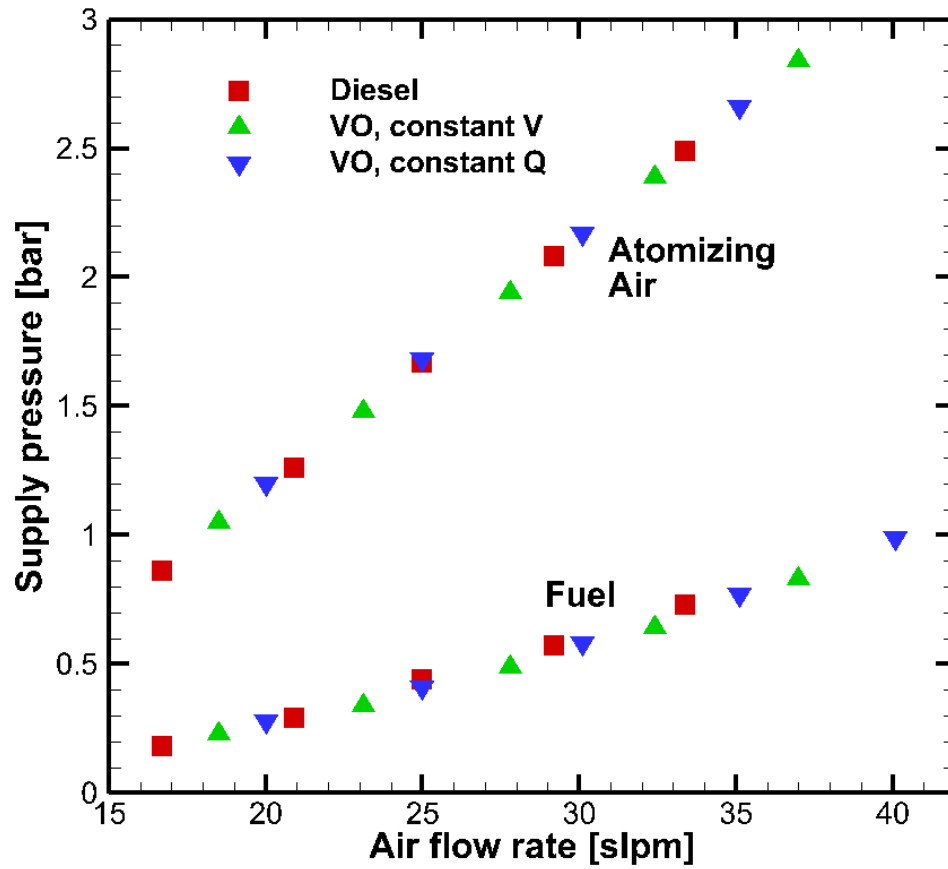


Figure 5.4 Fuel and atomizing air supply pressure

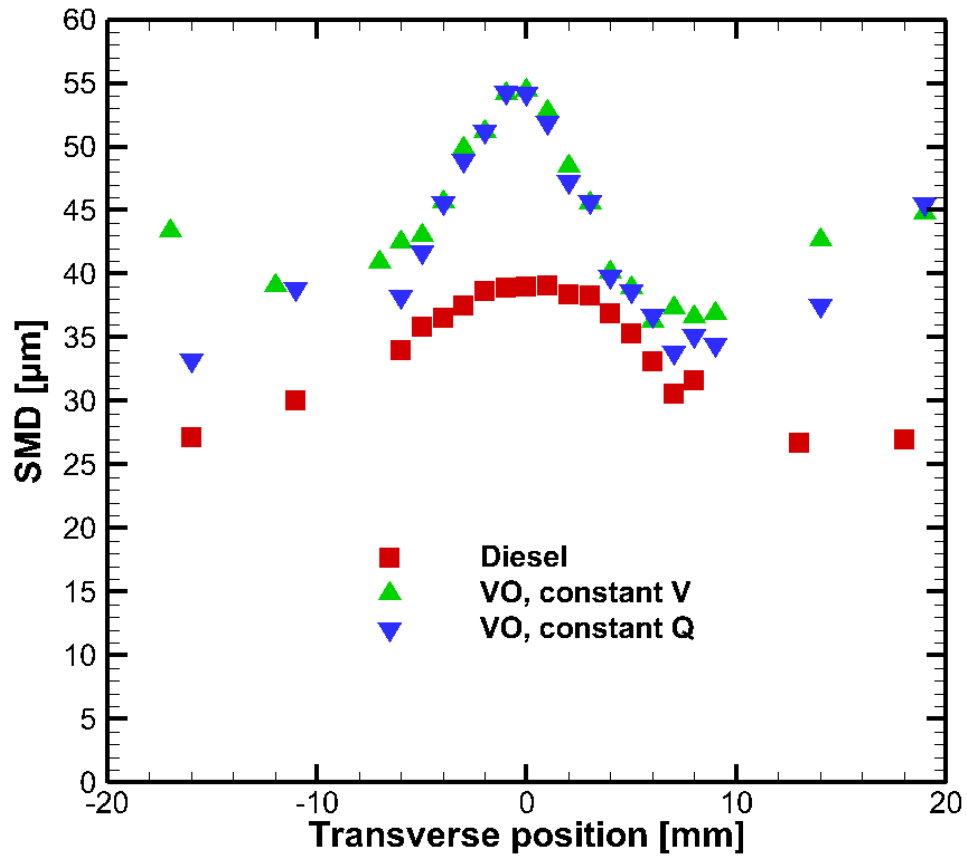


Figure 5.5 SMD profiles, ALR = 2

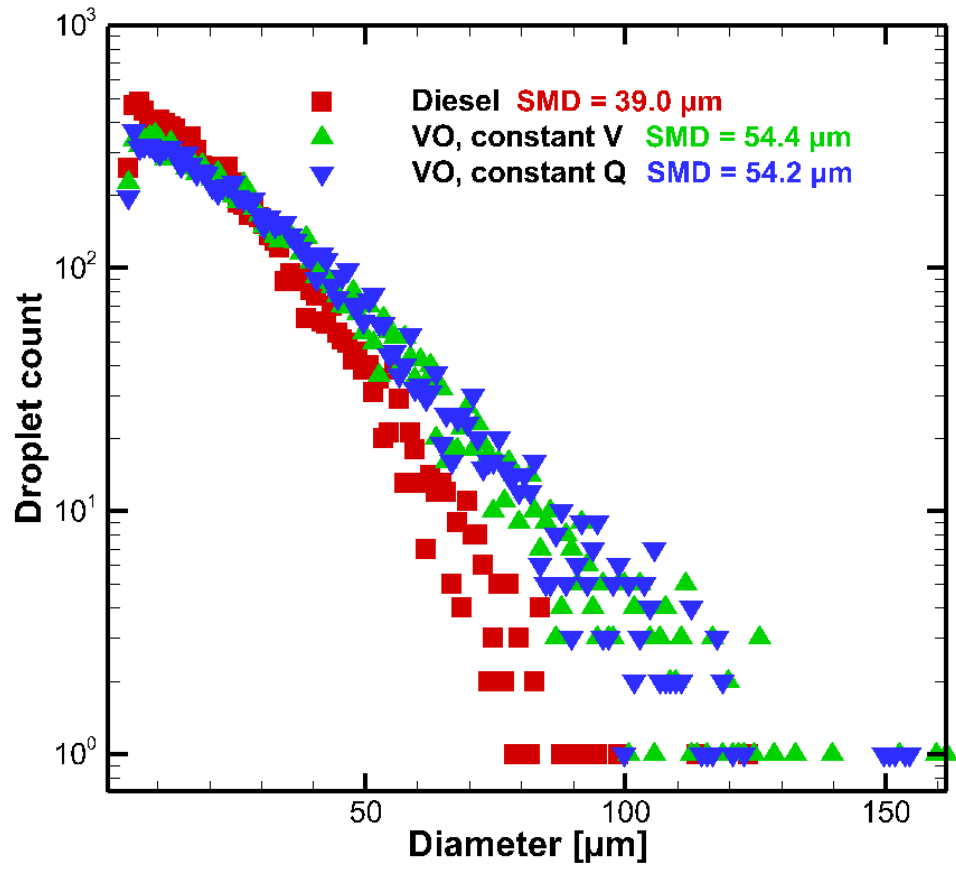


Figure 5.6 Droplet distribution at Z = 20 mm, R = 0 mm

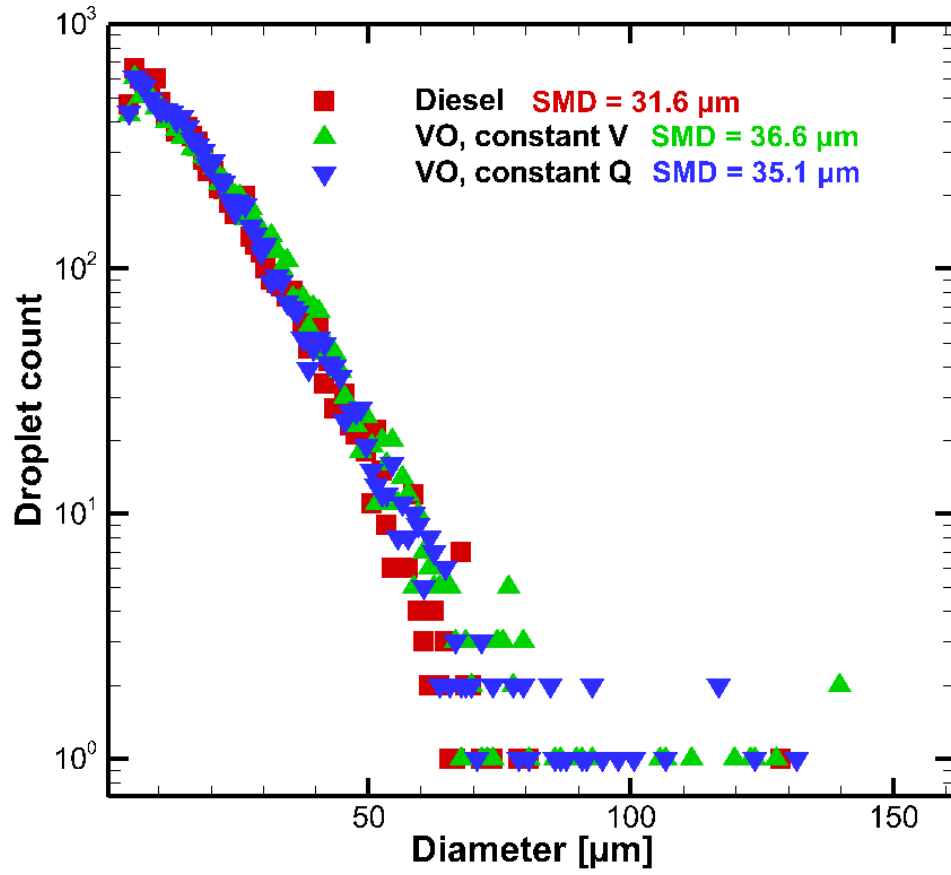


Figure 5.7 Droplet distribution at Z = 20 mm, R = 8 mm

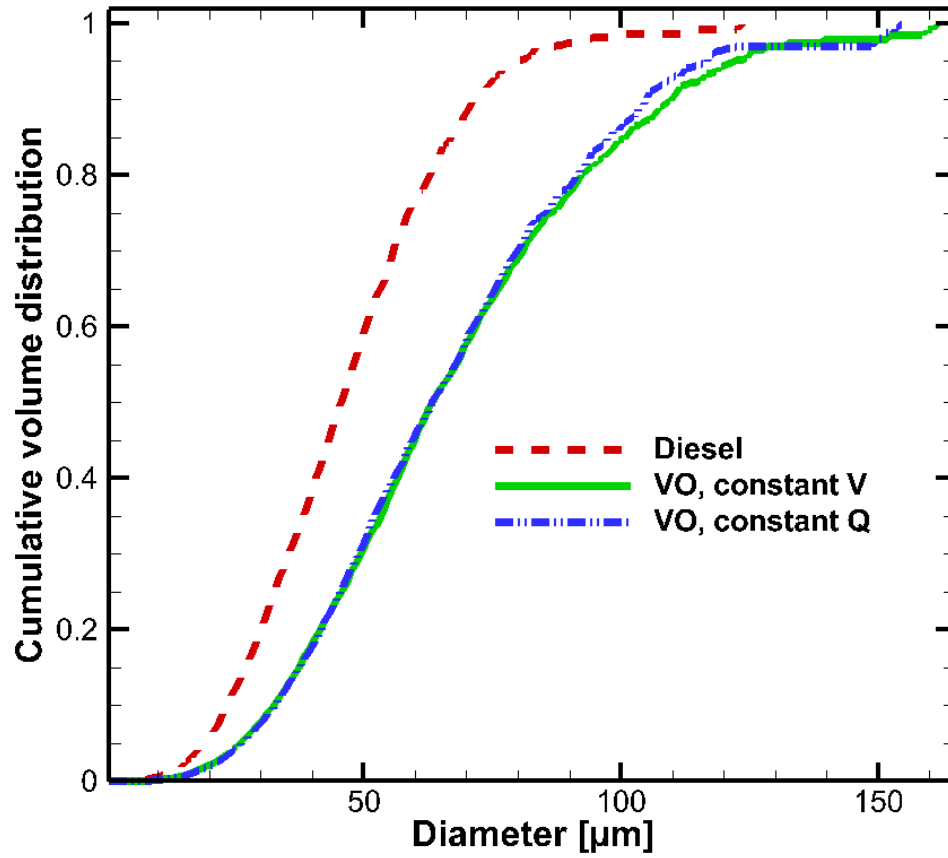


Figure 5.8 Cumulative volume distribution at $Z = 20$ mm, $R = 0$ mm

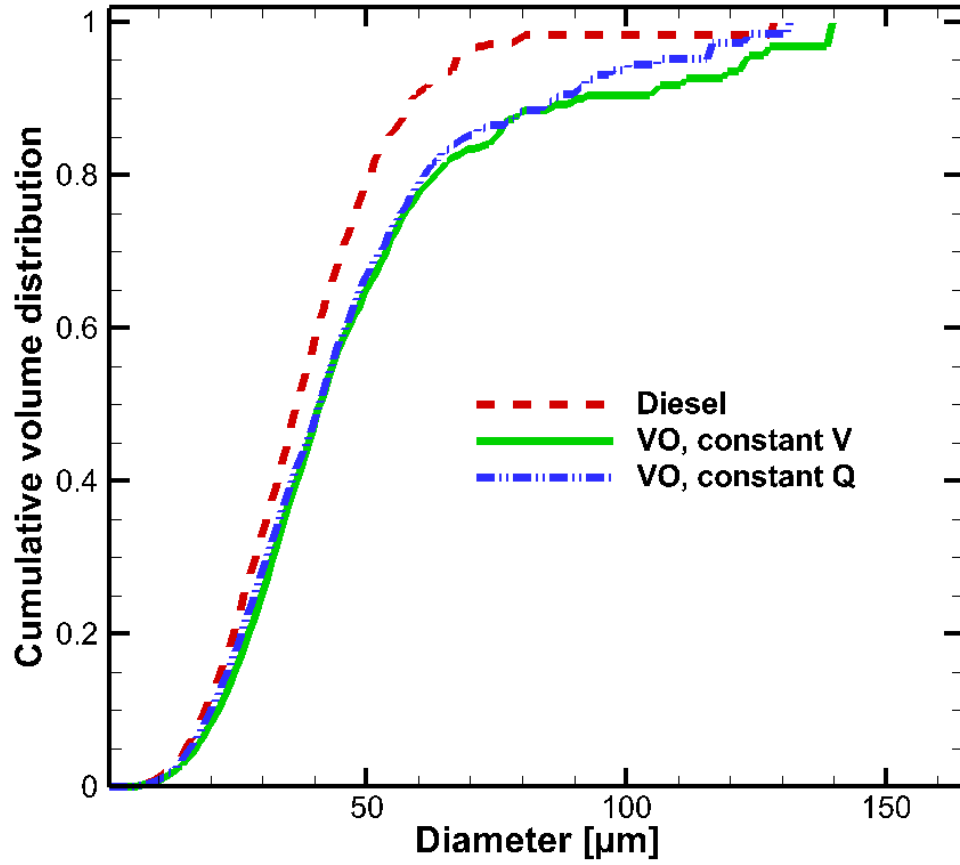


Figure 5.9 Cumulative volume distribution at Z = 20 mm, R = 8 mm

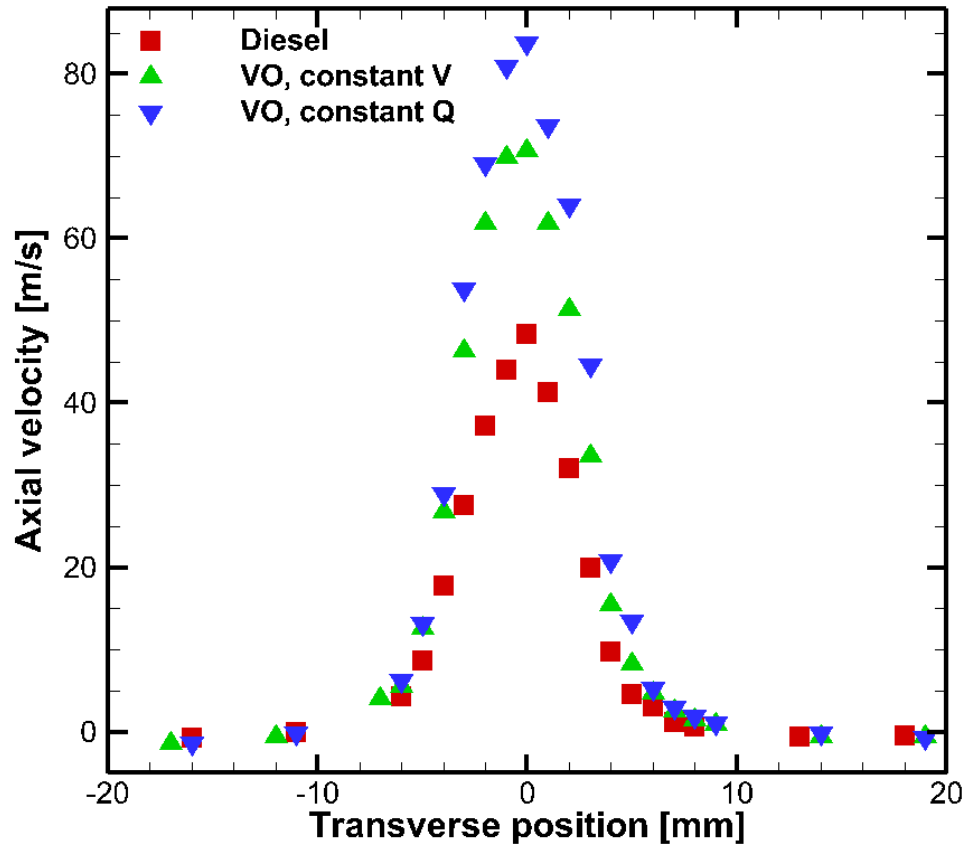


Figure 5.10 Axial velocity, ALR = 2

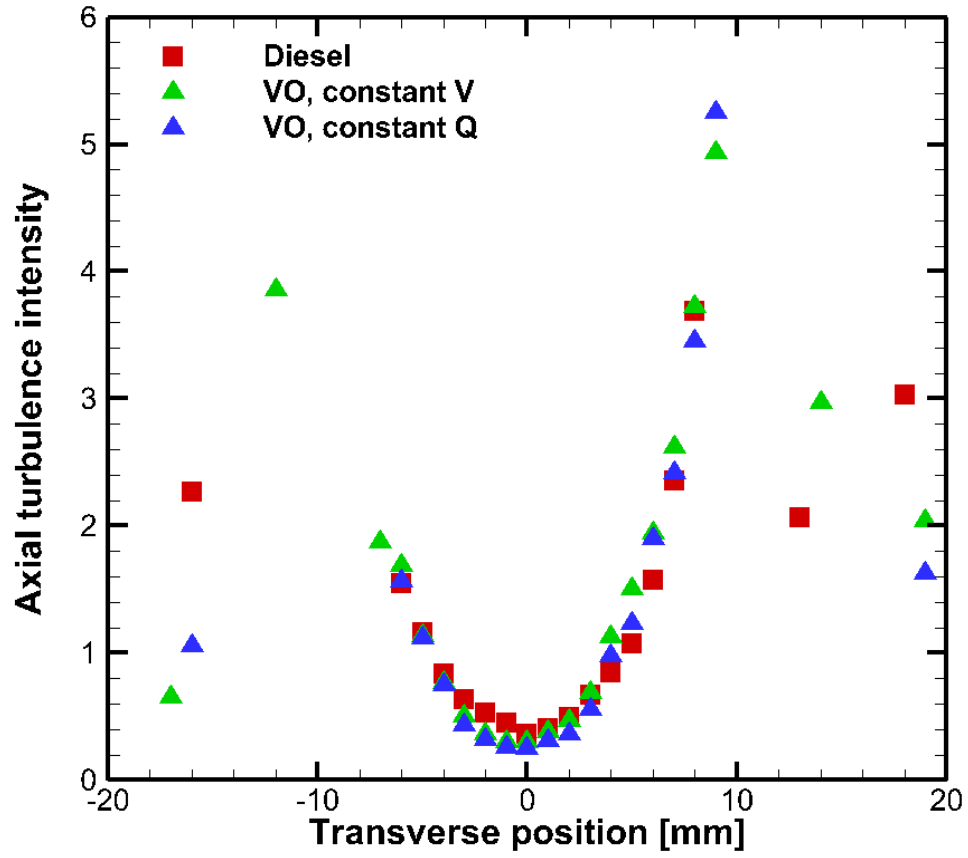


Figure 5.11 Axial turbulence intensity, ALR = 2

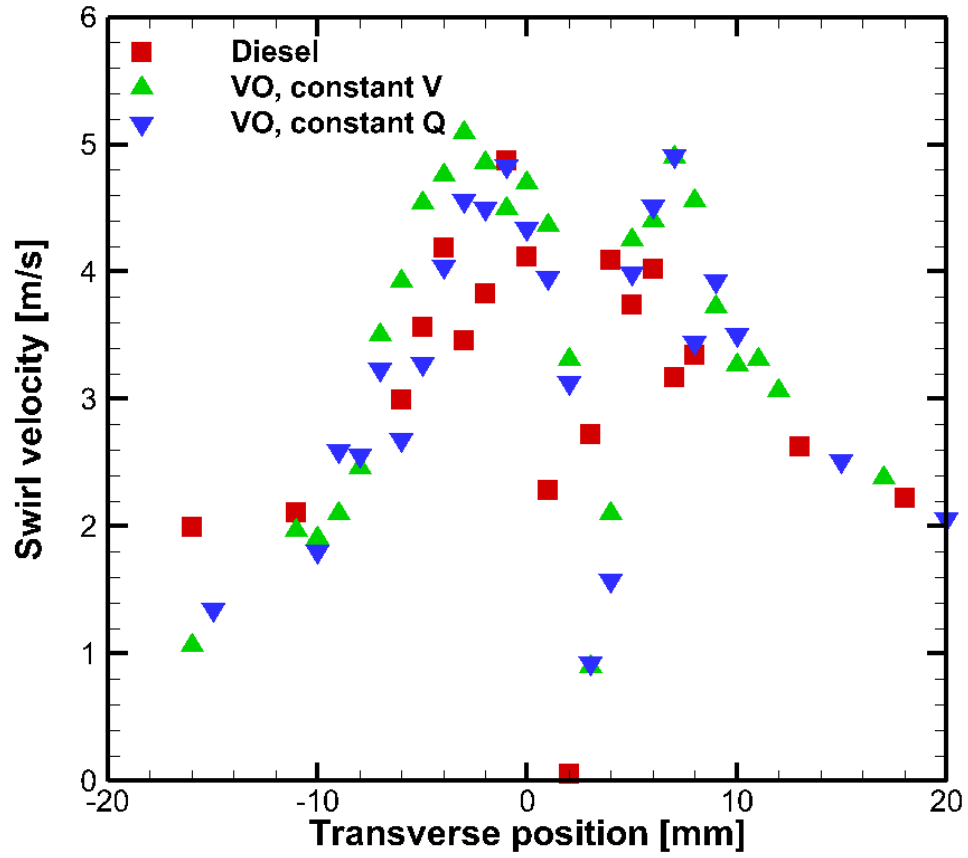


Figure 5.12 Swirl velocity, ALR = 2

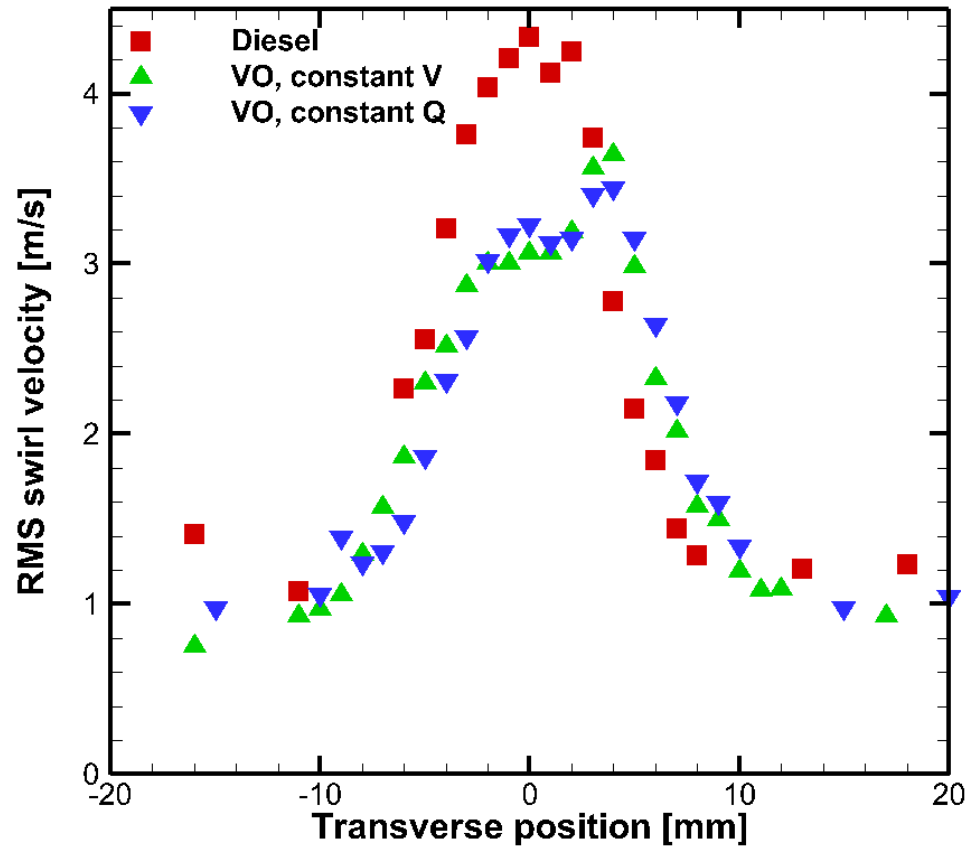


Figure 5.13 RMS swirl velocity, ALR = 2

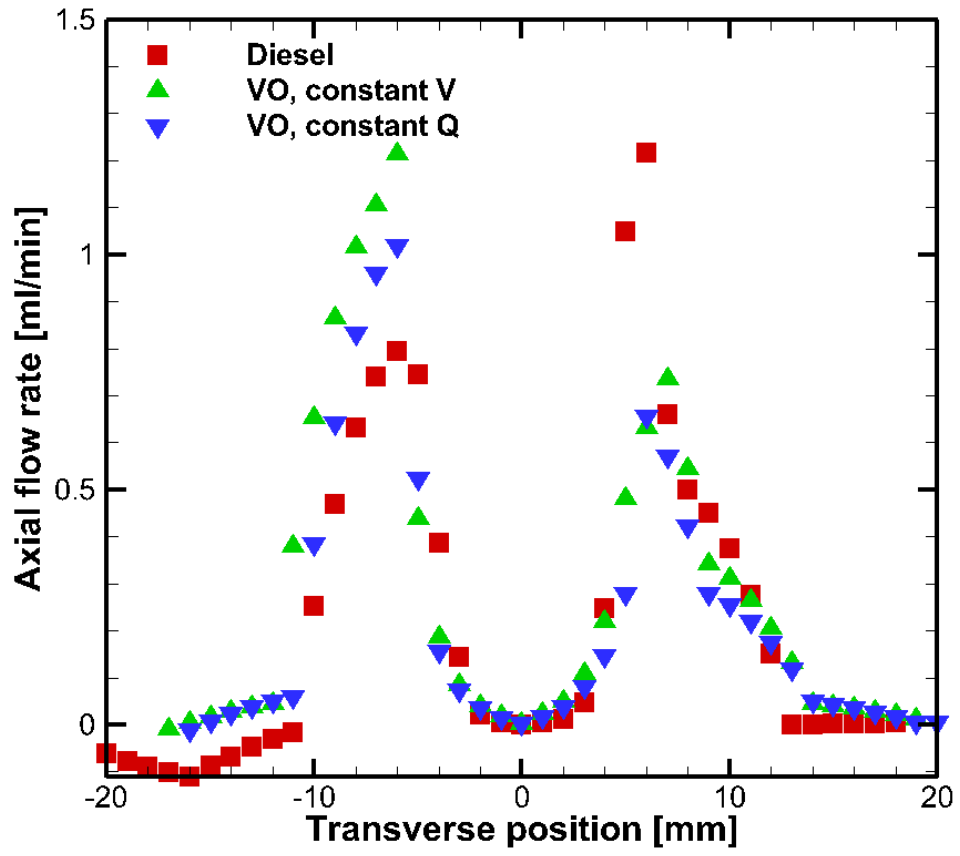


Figure 5.14 Axial volume flow, ALR = 2

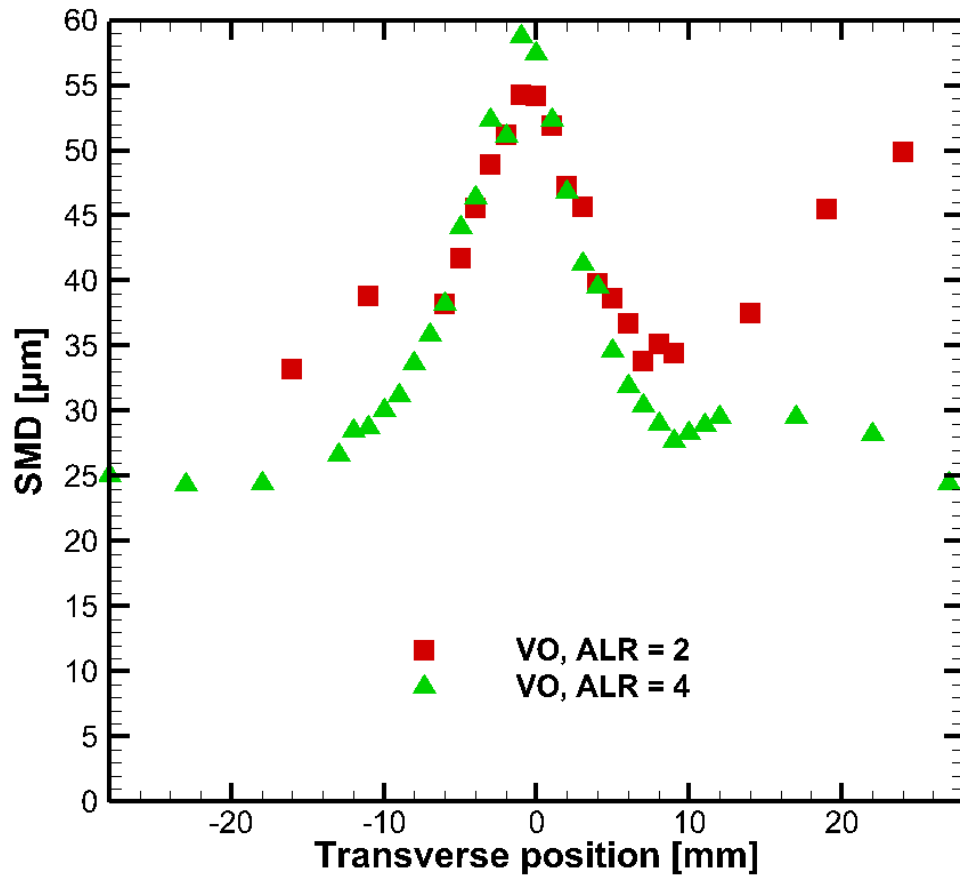


Figure 5.15 SMD profiles

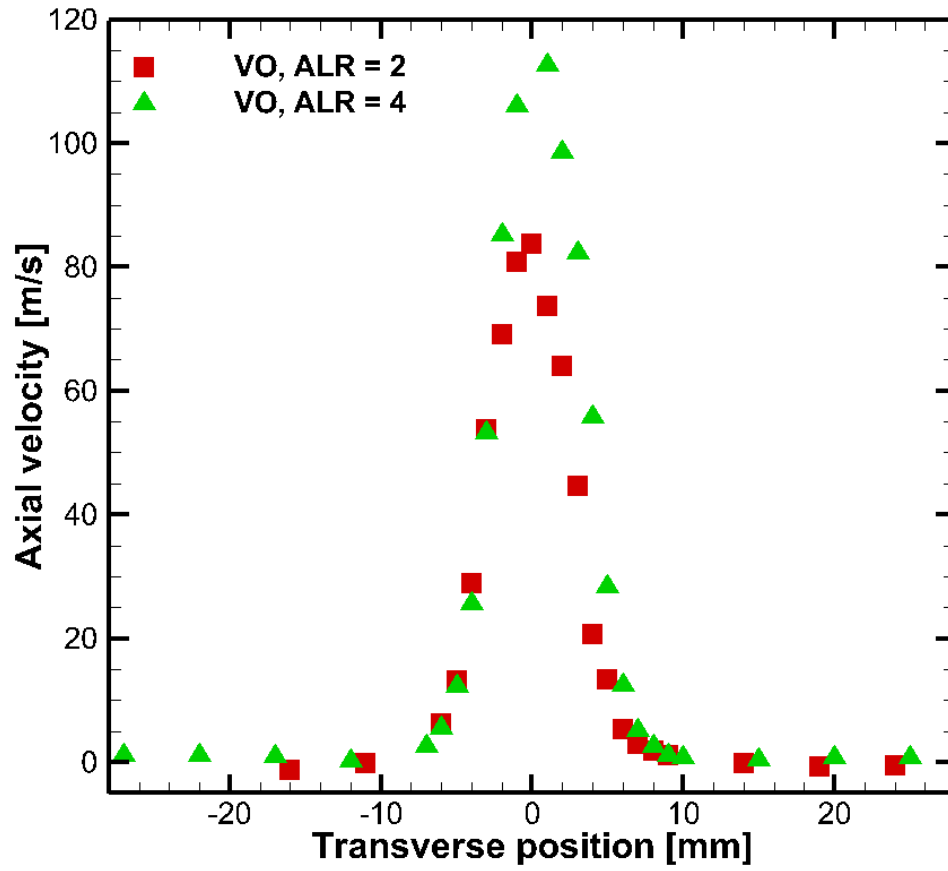


Figure 5.16 Axial velocity profiles

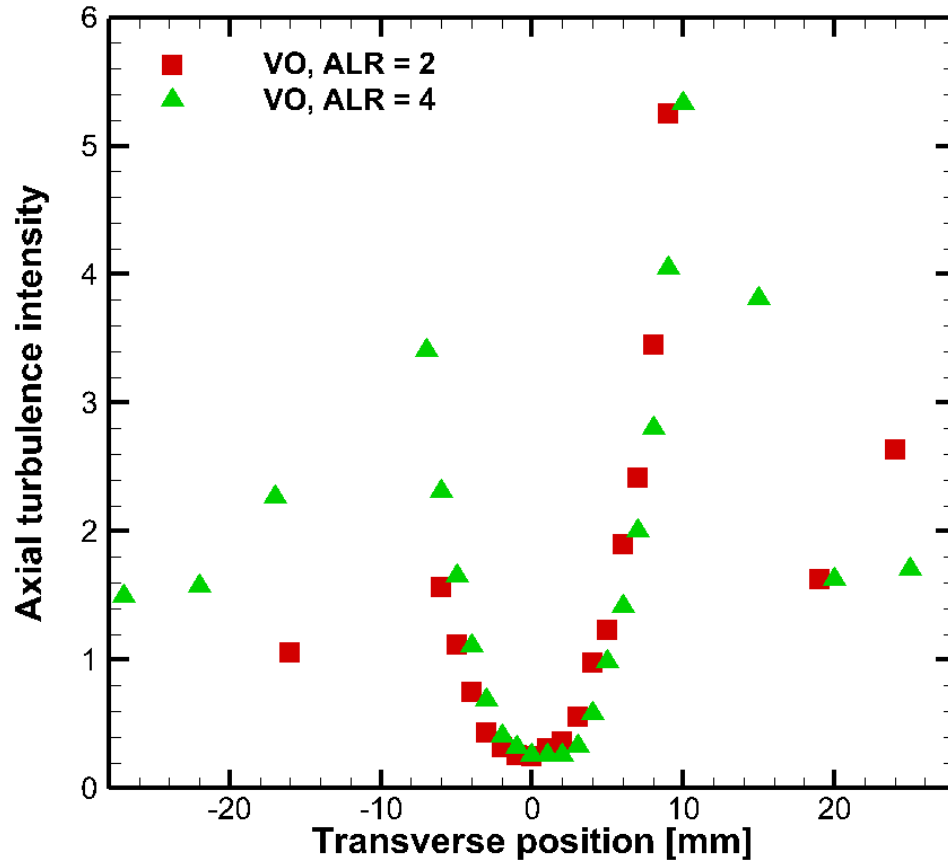


Figure 5.17 Axial turbulence intensity profiles

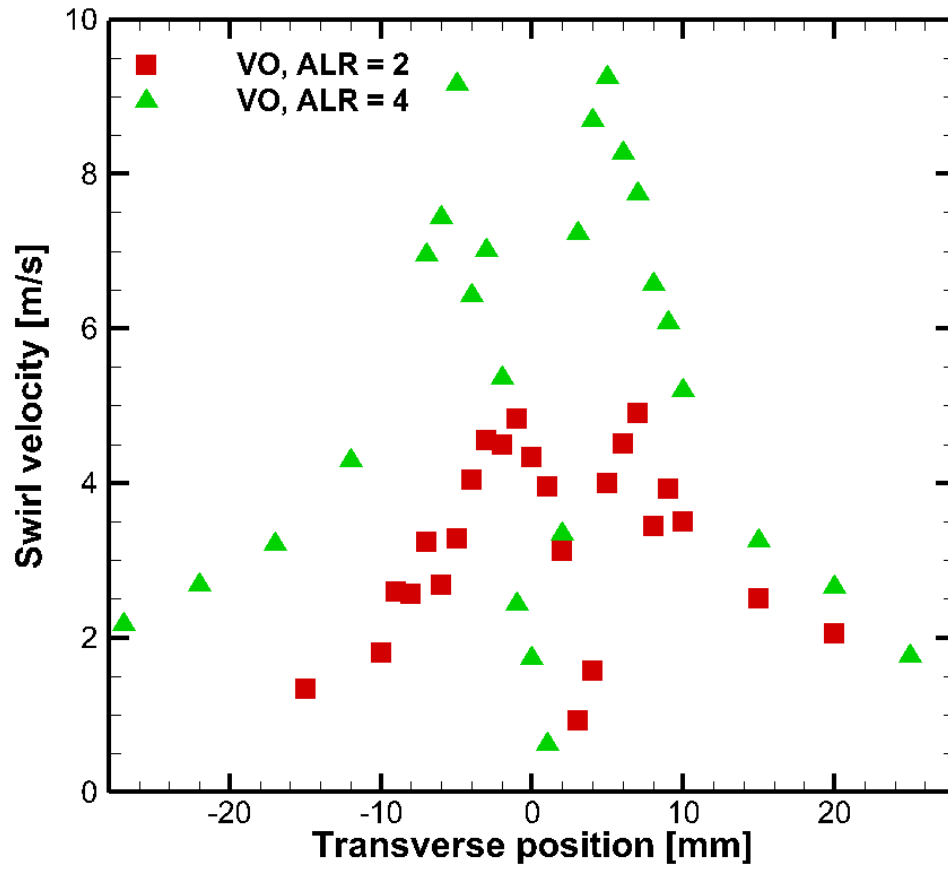


Figure 5.18 Swirl velocity profiles

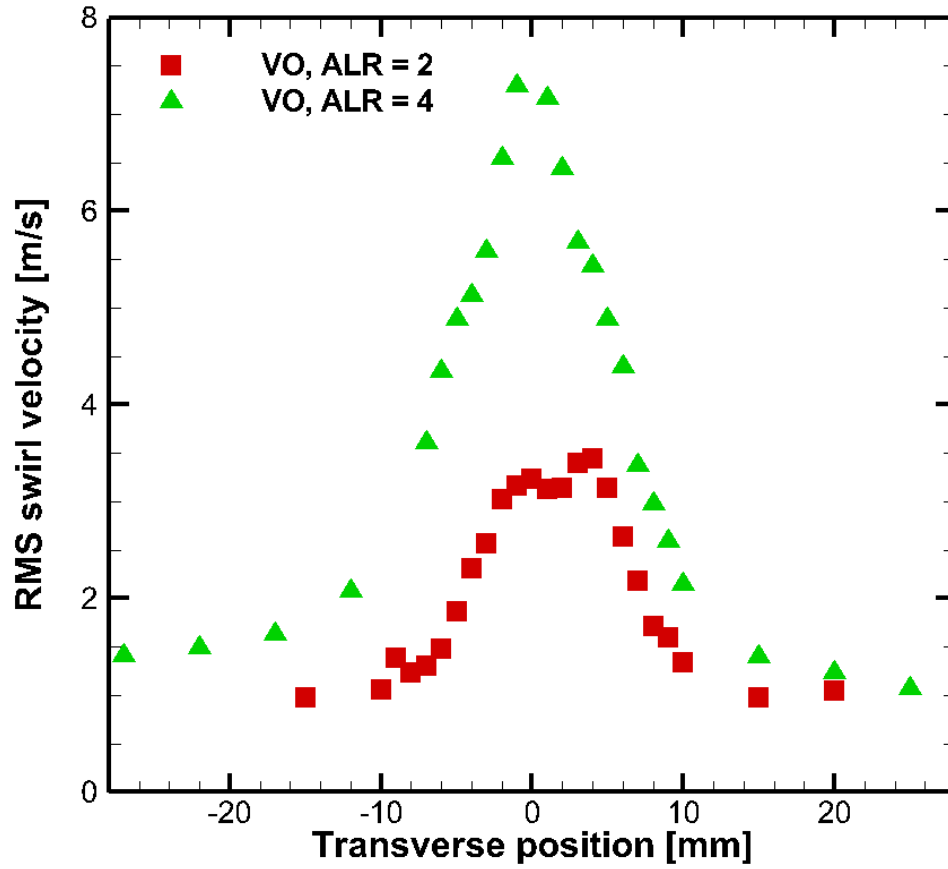


Figure 5.19 RMS swirl velocity profiles

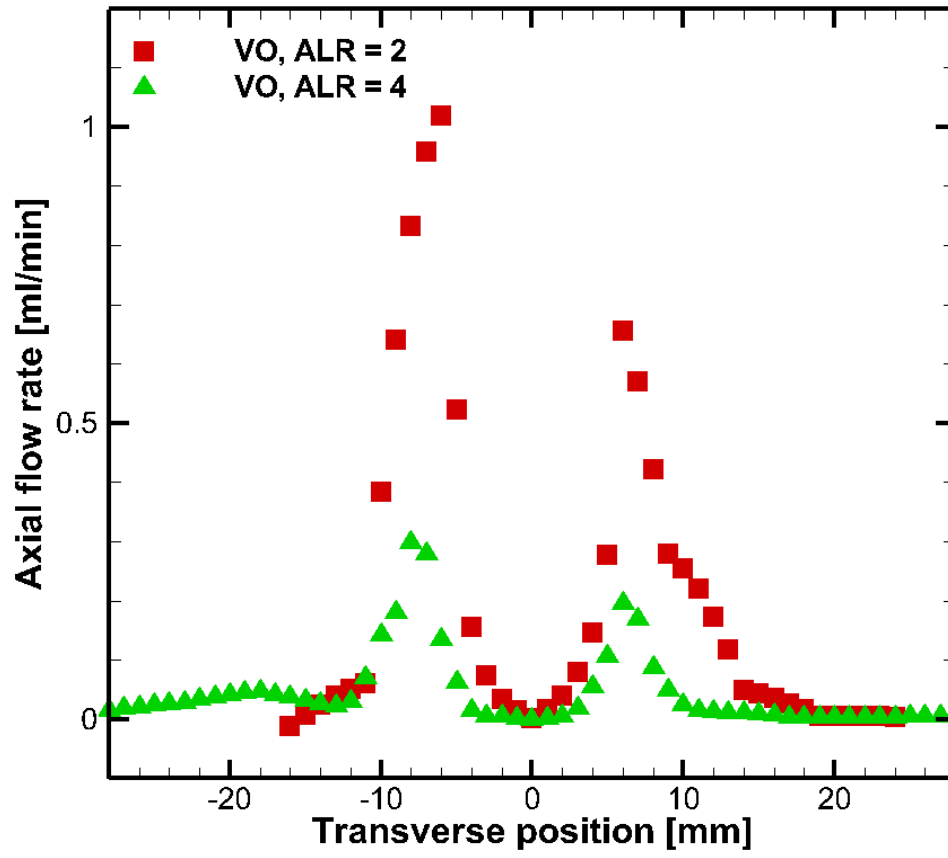


Figure 5.20 Axial volume flow profiles

CHAPTER 6

FLOW AND DROPSIZE MEASUREMENTS IN GLYCEROL SPRAY FLAMES

6.1 Background

The transesterification process is used to reduce the viscosity of source bio-oil and create biodiesel, but the byproduct glycerol is produced at roughly a 10% volumetric rate of biodiesel. The National Biodiesel Board has estimated that approximately 498 million gallons of biodiesel will be produced between 2006 and 2015, meaning large quantities of glycerol as well [2006]. While glycerol has many applications, its production has surpassed its demand in recent times, causing it to be treated as a waste stream and costing manufacturers for its disposal. While the price of glycerol has increased recently, it is likely that this problem will be encountered again. Glycerol could prove to be an easily used energy source for biodiesel manufacturers if a simple method is discovered for its clean combustion.

Table 6.1 shows some common properties for glycerol [Panchasara et al, 2009b; CRC Handbook, 2010; da Silva and Müller, 2010; #2 Diesel MSDS, 2011; Glycerol MSDS, 2011; Sahin and Gurgum, 2007]. The table shows that glycerol has many negative properties, especially in comparison to diesel fuel. Most noticeably, glycerol's kinematic viscosity is around 190 times that of diesel at 25° C. Glycerol also has twice the surface tension of diesel. Both properties are central in the suppression of instabilities leading to fine fuel sprays. Higher enthalpy of vaporization, vaporization temperature, and auto-ignition temperature signify that glycerol requires greater amount of thermal energy to pre-vaporize and combust in premixed mode. Therefore, sufficient energy from the flame must reach the near-field of the spray to

ensure proper vaporization and combustion. Glycerol has a low heating value, but still offers significant energy that can be recovered onsite.

Table 6.1 Fuel Properties

| | # 2 Diesel | Glycerol |
|---|-------------------|-----------------|
| Chemical Formula | varies | $C_3H_5(OH)_3$ |
| Mol. Weight [kg/kmol] | 142.2 | 92.1 |
| Density @ 25°C [kg/m ³] | 834 | 1260 |
| Kinematic Viscosity @ 25°C [mm ² /s] | 3.88 | 741 |
| Surface Tension @ 25°C (mN/m) | 28.2 | 62.5 |
| Lower Heating Value [MJ/kg] /[MJ/m ³] | 44.6/37,200 | 16.2/20,400 |
| Enthalpy of Vaporization [kJ/kg] | 522 | 662 |
| Auto-Ignition Temperature [°C] | 260 | 370 |
| Vaporization Temperature [°C] | 160-370 | 290 |

Previous studies have shown that glycerol can be combusted in a combustion system. Bohon et al reported on two glycerol combustion systems: insulated 7 kW and 82 kW combustors [2011]. Results showed single digit NO_x and undetectable CO (meaning less than 0.1%) for pure glycerol in the 7 kW system, while the 82 kW system produced much higher NO_x (up to 235 ppm at 0% O₂ for raw glycerol samples). While the 7 kW system was able to operate on unheated glycerol fuel, the 82 kW system utilized a fuel heater to preheat the raw glycerol and reduce its viscosity [Bohon et al. 2011]. Figures 6.1 and 6.2 show emissions measurements for the insulated 7kW system discussed in chapter 3 operating with glycerol/methane flames created using a flow-blurring (FB) fuel injector. Results show that low emissions can be achieved, that

pure glycerol (G100) can be cleanly combusted, and methane addition can be tailored to reduce both carbon monoxide (CO) and nitric oxide (NO_x) emissions.

Air-blast (AB) atomization is widely used for fuel breakup in stationary combustion applications. In the AB method, atomizing air interact with a fuel stream at high relative velocity to create high shear in the fuel surface. This high shear causes the growth of instabilities that deform the fuel stream surface and cause it to break up into droplets. Compatible fuel properties are critical in the atomization success of the AB process. The instabilities leading to breakup are suppressed by high kinematic viscosity and surface tension. The effervescent atomization (EA) technique is less dependent on fuel properties than the AB technique. EA consists of fuel and atomizing air being mixed upstream of an injector exit to form a two-phase mixture. As this two-phase mixture exits the injector, it travels through a negative pressure gradient, causing the gas phase to rapidly expand. This rapid expansion causes air bubbles to burst, creating a spray with very fine droplets. The EA concept has only been implemented on a limited basis because of its inherent drawbacks, such as flow instabilities due to two-phase flow under certain conditions [Sovani et al, 2001].

The FB atomization concept utilizes a simple design yet delivers a robust atomization method. Gañán-Calvo first reported the FB concept, seen conceptually in figure 6.3 [2005]. A fuel tube is kept some distance (H) from an exit orifice of the same diameter (d), while atomizing air flows around this fuel tube. This distance (H) is critical to the flow field within the FB injector. When H is relatively large, the atomizing airflow and the fuel stream exit the orifice and interact similarly to an AB atomizer. As H is decreased, a dramatic change in the internal flow path takes place. When H is equal to approximately 0.25d, the atomizing air turns into the fuel stream and mixes intensely with the fuel at the tip of the fuel tube. Thus, a bubbly two-

phase flow is created, which subsequently experiences a rapid pressure decrease across the orifice, causing the gas phase to expand to create a fine spray. The FB process is inherently different from the EA process, as fuel/air mixing occurs only in a short region in the fuel tube and is determined only by the FB injector's geometry.

The FB injection technique's superiority over AB atomization has been widely documented. Gañán-Calvo reported that the FB concept created "five to fifty times" more fuel surface area than a plain-jet AB atomizer operating at the same conditions [2005]. Another study compared water sprays from AB and FB injectors and concluded that the FB injector produced sprays with smaller average droplet sizes and required less atomizing air line pressure than the AB injector [Simmons and Agrawal, 2011]. Research has also been done on FB injectors in reacting systems. Panchasara et al. reported that the FB injector reduced carbon monoxide (CO) and nitric oxides (NO_x) emissions by three to five times, as compared to an AB atomizer operating at the same conditions [2009a]. It was also reported that the FB injector is able to efficiently atomize and combust straight VO [Simmons et al, 2008]. As discussed earlier in chapter 3, the FB injector has also been used successfully in the combustion of straight glycerol in insulated environments. This study seeks to investigate droplet diameter and velocities within the reacting glycerol spray to explain the low emissions measured in glycerol flames.

6.2 Experimental Setup

The combustion system used in this study can be seen in figure 6.4. Primary air (for combustion) enters through the bottom of the combustor and mixes with methane before passing through a swirler and entering the insulated combustion chamber. Atomizing air (for fuel breakup) travels through a small pipe in the center of the system and then enters the injector assembly located in the center of the swirler. Liquid fuel is introduced through the side of the

system before entering the FB injector assembly. The FB injector was created by keeping the external dimensions of a commercial AB injector (Delevan model 30609-2) while changing the internal structure. Fuel passages were widened to 1.5 mm and the FB method was ensured by using a spacer to precisely distance the fuel tube from the injector orifice.

Methane is supplied from pressurized tanks and its flow is controlled using Sierra Instruments Smart-Trak mass flow controllers. Glycerol is both supplied and metered using a Cole-Parmer peristaltic pump with an uncertainty of $\pm 0.25\%$ of the reading. Air is supplied by a compressor system and passes through filters to remove moisture before being introduced into the system. Primary air flow is measured by a laminar flow element with an uncertainty of ± 5 standard liters per minute (slpm). Atomizing air flow is controlled using a Sierra Instruments 810C mass flow controller with an uncertainty of ± 0.5 slpm.

Droplet size and velocity measurements were acquired with the phase Doppler particle analyzer (PDPA) technique. Two sets of beams (488 nm and 514.5 nm wavelength) intersect at the measurement volume. A Bragg cell is used to slightly shift the frequency of one beam from each pair, creating a moving fringe pattern in the measurement volume. As a droplet passes through the measurement volume, it scatters light to form an interference signal, which is detected by a receiver which is located 144° from the transmission probe. The acquired signal is processed by software (TSI FlowSizer version 2.0.4) to obtain the dominant frequency, which is directly proportional to the droplet velocity. The phase difference from two measurement signals is then determined and used to calculate the droplet size.

Combustion took place in a pentagonal enclosure (seen in Figure 6.5) to allow the laser beams to enter the system normally. Figure 6.6 shows a diagram of the PDPA system with the pentagonal enclosure. Pentagon was used to allow laser beams and receiver line of sight to enter

the system normally. The traverse moves the entire PDPA system on the Cartesian coordinate displayed in the figure. X is parallel to laser beams, while Y is parallel to them. Figure 6.7 shows the details of the enclosure and the coordinates used for measurement. The spray can be seen in the middle of the enclosure. By sweeping across the dashed lines (representing two radii in the spray), the X direction aligns with the radial and swirl directions within the spray. This allows the 2-d PDPA system to be used for 3-d measurements within the spray. More details on PDPA operation and alignment can be seen in appendix F.

Experiments were started by igniting a methane/air flame and then gradually increasing glycerol flow rate while decreasing methane flow rate until the desired conditions were met. For present experiments, total air flow rate was 150 slpm, heat release rate was 7.9 kW, and gas flow through the injector was 30 g/min. The percentage of total heat release rate from glycerol and methane was varied, with some methane being injected through the injector with atomizing air. G68 and G45 represent 68% and 45% of heat release from glycerol, respectively, with the balance coming from methane. The term G45-29 means that 29% of the total methane flow is supplied through the atomizer. All measurements were taken approximately 10 cm from the FB injector exit as this was the most downstream point of optical access. R within the text refers to the transverse axis across the spray. Figure 6.8 shows a diagram of the spray and flame location for the test cases. In all cases the flame stabilized at the exit of the steel combustor, downstream of the spray and measurement location. Therefore, measurements were not in the flame zone.

6.3 Results and Discussion

Figure 6.9 shows the mean axial velocity profiles for sprays in G68, G45, and G45-29 flames. All three sprays have the same gaseous and liquid mass flow rates through the injectors. Thus, the axial velocity profiles are similar, with peak values around 65 to 70 m/s. Velocities

decreased to 20 m/s around $R = 40$ mm. Figure 6.10 shows that the RMS axial velocity is around 12 m/s at the periphery of the spray and it increases to 25 to 35 m/s towards the center of the spray. Figure 6.11 shows mean radial velocity profiles for the three cases. Mean radial velocity is around 5 to 6 m/s on the edge of the spray and reduces to around zero at the center of the spray. Figure 6.12 presents the RMS radial velocity for the three sprays with values around 1.5 m/s in the center of the spray and increasing to 4 to 5 m/s on one side and around 3.5 m/s on the other side. Figure 6.13 shows the mean swirl velocities for the three test conditions. mean swirl velocity is around 2.5 to 3 m/s at the periphery of the spray and it approaches zero towards the center of the spray. Figure 6.14 presents the RMS swirl velocity for all three sprays. Maximum RMS swirl velocity is in the center of the spray, with its values decreasing to 1 to 1.5 m/s at the periphery of the spray. Asymmetries in radial and swirl measurements show that the PDPA and combustion systems were not perfectly aligned.

Figure 6.15 shows the transverse profile of the measured SMD within the spray. The G68 flame produces the largest droplets even though there is significant overlap among all cases. It is expected that the G68 flame would result in the largest droplets as more glycerol is being atomized by the same amount of atomizing fluid. The two G45 cases produce very similar results with the methane through the swirler case resulting in slightly smaller droplets. In all sprays the SMD is generally around 25 to 40 μm . These values are smaller than data taken in non-reacting vegetable oil and diesel sprays from Simmons and Agrawal [2011]. VO sprays were seen to have droplets with SMDs from between to 35 to 55 μm . Simmons and Agrawal reported data at an axial distance of 20 mm from the injector, so the glycerol measurements have the benefit of a longer period of time in a hot environment when making comparisons [2011].

Still, these glycerol data suggest that the FB injector can successfully atomize an extremely viscous fuel.

Figures 6.16 through 6.21 show droplet diameter distributions and cumulative volume distributions from three points within the spray: $R = 10, 20,$ and 30 mm. Figures 6.16 and 6.17 show that at $R = 10$ mm, the G68 spray contains slightly larger droplets with SMD of $36 \mu\text{m}$. Droplet diameter data from $R = 20$ mm are presented in figures 6.18 and 6.19. The G68 case again has the largest SMD ($35 \mu\text{m}$), while the two G45 cases have very similar SMDS of 31 and $32 \mu\text{m}$. Figures 6.20 and 6.21 present droplet data distribution and cumulative volume distribution, respectively, at $R = 30$ mm. Even though the G68 and G45 have different diameter distribution profiles, they have the same SMD of $38 \mu\text{m}$. The G68 flame has more large droplets, but it also contains more droplets below $50 \mu\text{m}$, seen clearly in Figure 6.21.

Figure 6.22 shows the axial volumetric flux of glycerol within the spray. Glycerol flow in the center of the spray is nearly negligible while it increases towards the spray periphery. Data in figure 6.22 can be coupled with the SMD data in figure 6.15 to calculate a flow-weighted SMD for the entire spray (discussed in detail in chapter 5). This results in flow-weighted SMDs of $40, 35,$ and $37 \mu\text{m}$ for G68, G45, and G45-29, respectively. Clearly the flow-weighted SMD for all three flames is similar and again highlights the effectiveness of the FB technique to atomize high viscosity fuel for a wide range of operating conditions.

6.4 Conclusions

This study presents the first known measurements of velocity and droplet diameter statistics within a glycerol combustion system. Flow fields were similar for G68, G45, and G45-29 flames. SMD values in reacting glycerol sprays were measured and seen to be lower than those in previous measurements in VO cold sprays. G68, G45, and G45-29 flames resulted in

flow-weighted SMDs of 40, 35, and 37 μm , respectively. This study shows the FB injector can be used to successfully atomize and combust glycerol and presumably other highly viscous biofuels.

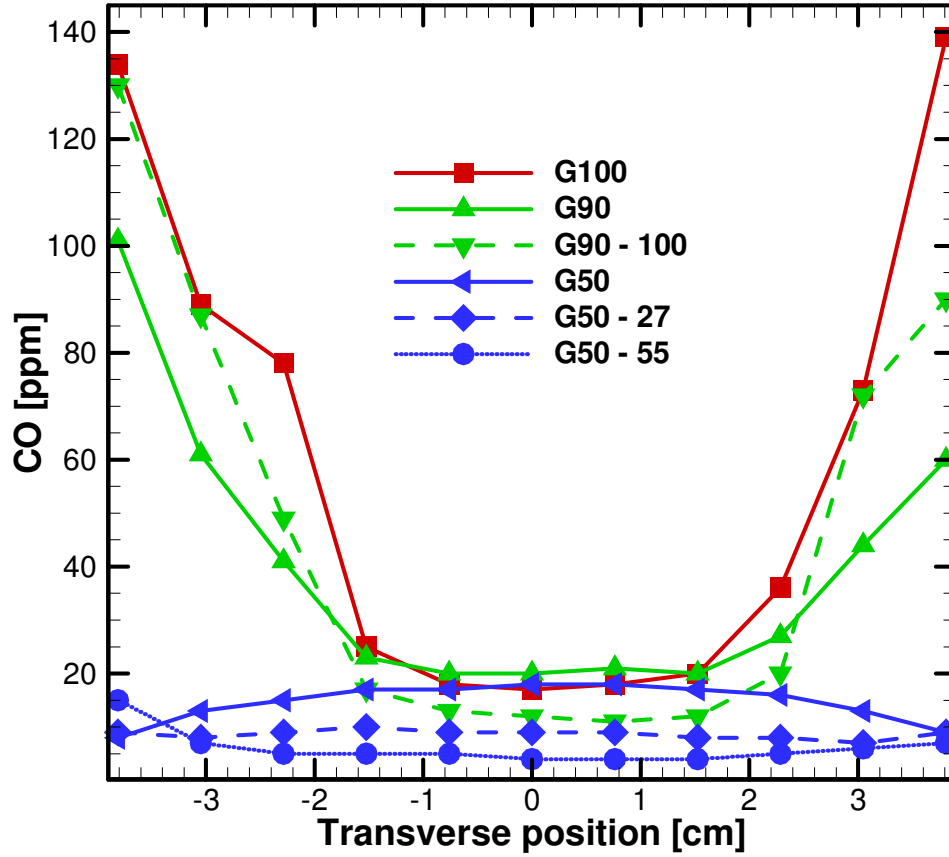


Figure 6.1 CO emissions at exit of insulated combustion chamber

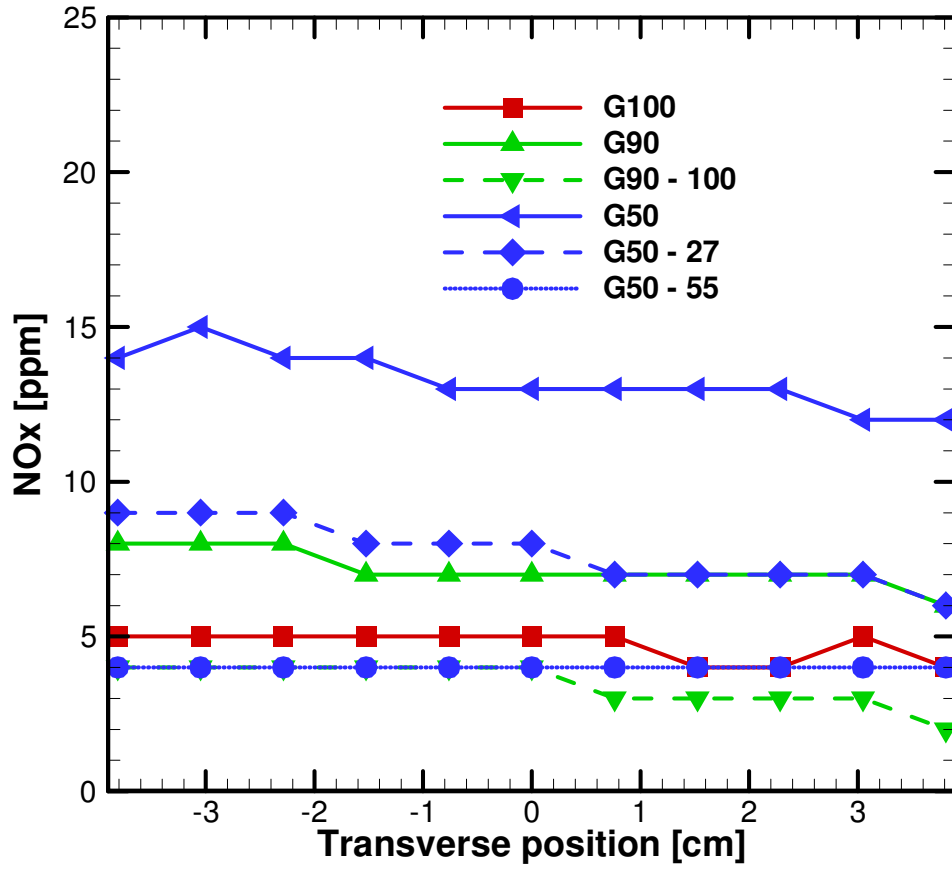


Figure 6.2 NO_x emissions at exit of insulated combustion chamber

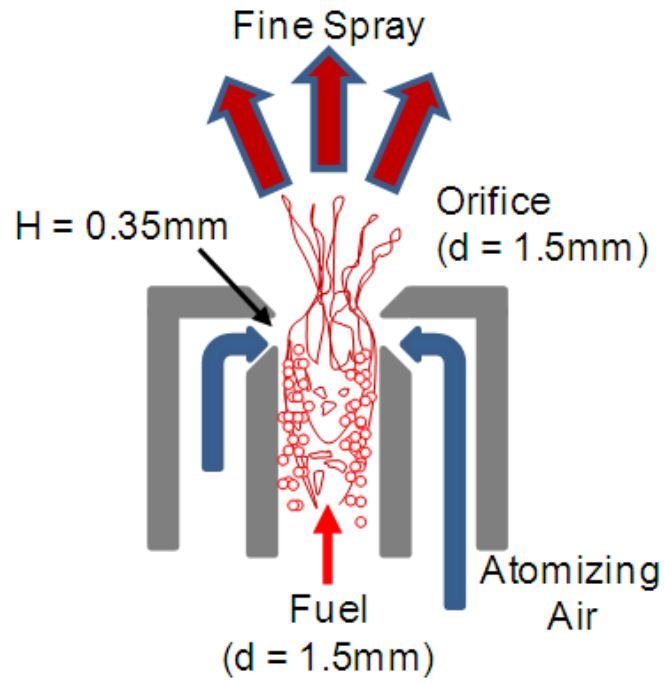


Figure 6.3 FB injection concept

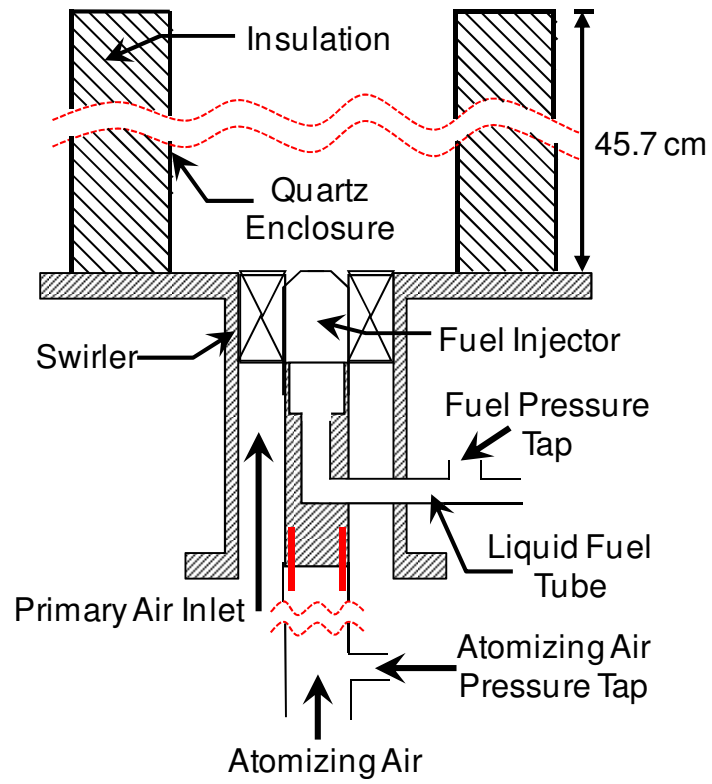


Figure 6.4 Experimental setup

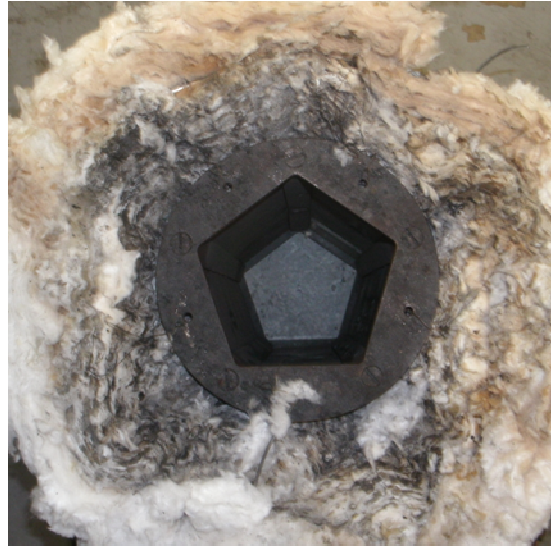


Figure 6.5 Insulated pentagonal enclosure with optical access

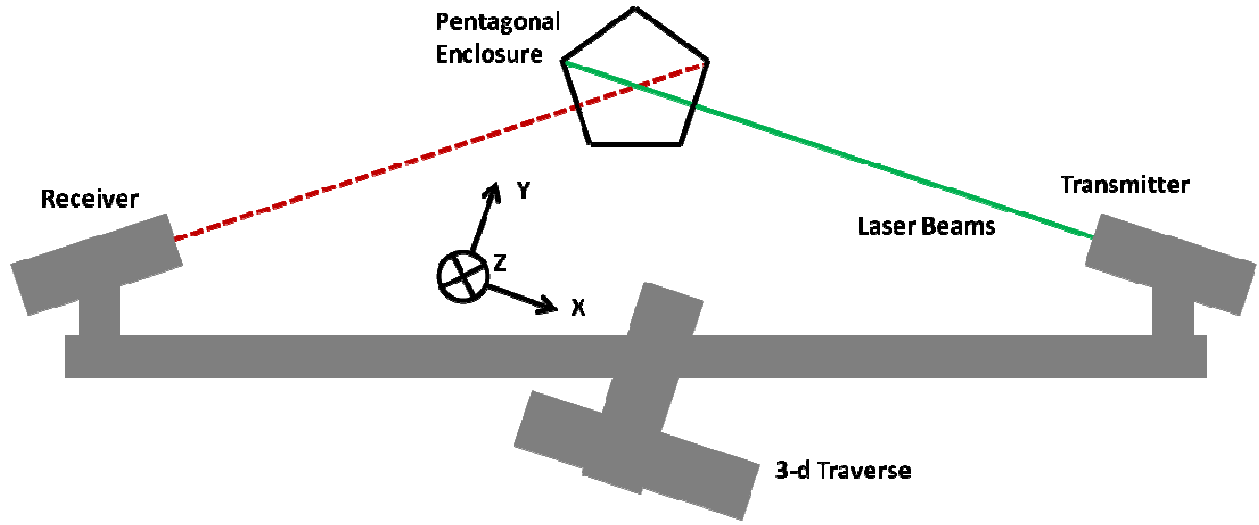


Figure 6.6 Diagram of PDPA setup, traverse, and pentagonal enclosure

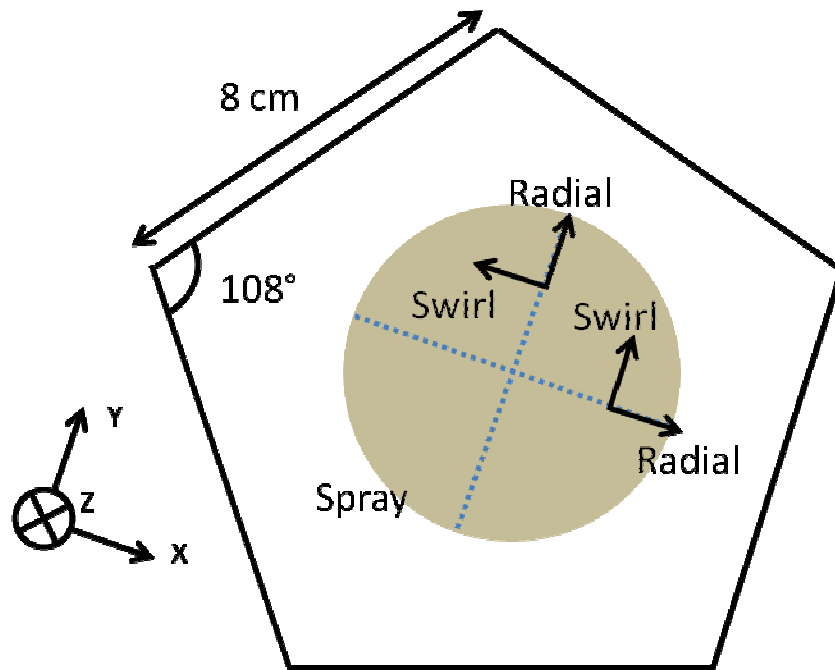


Figure 6.7 Diagram of PDPA pentagonal enclosure

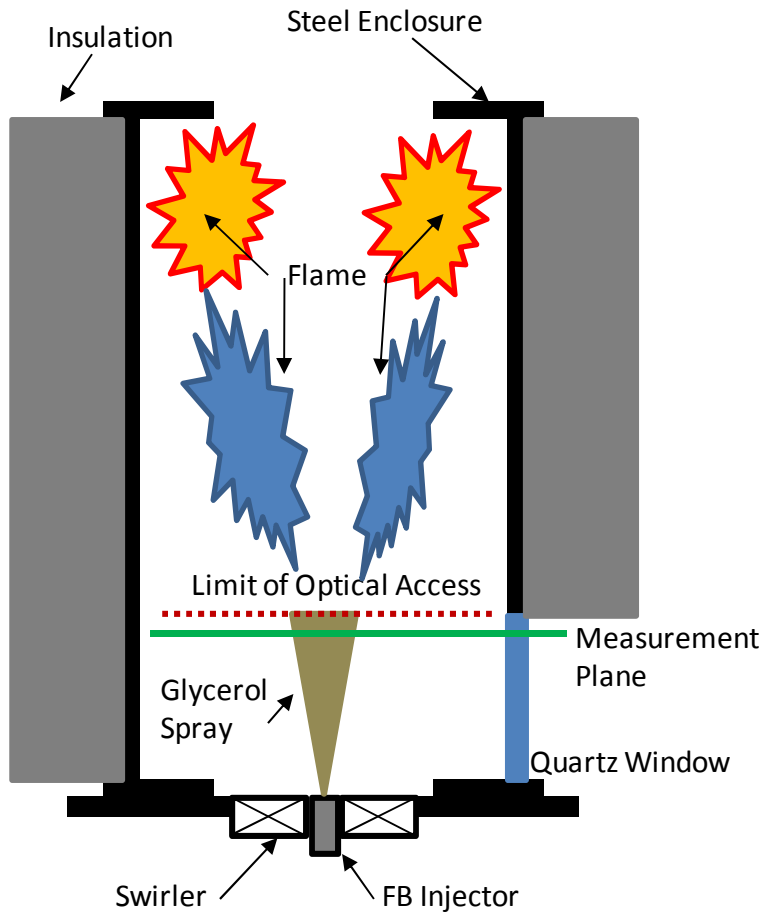


Figure 6.8 Diagram of spray and flame location in pentagonal insulated combustor

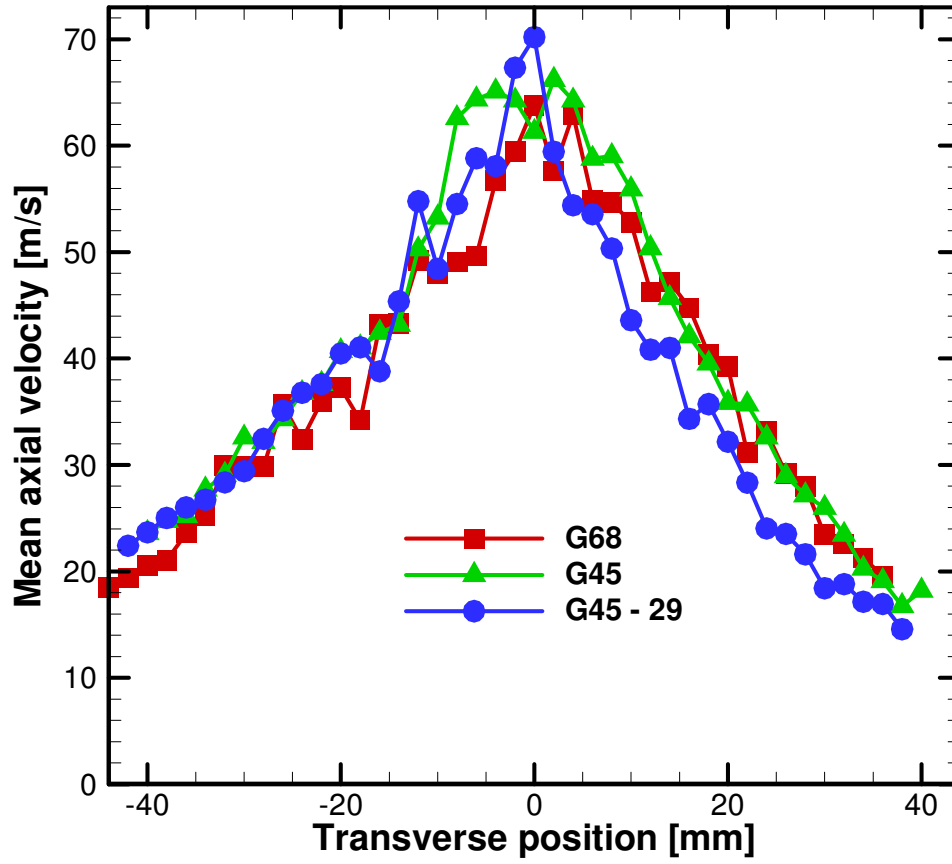


Figure 6.9 Mean axial velocity profiles of three cases

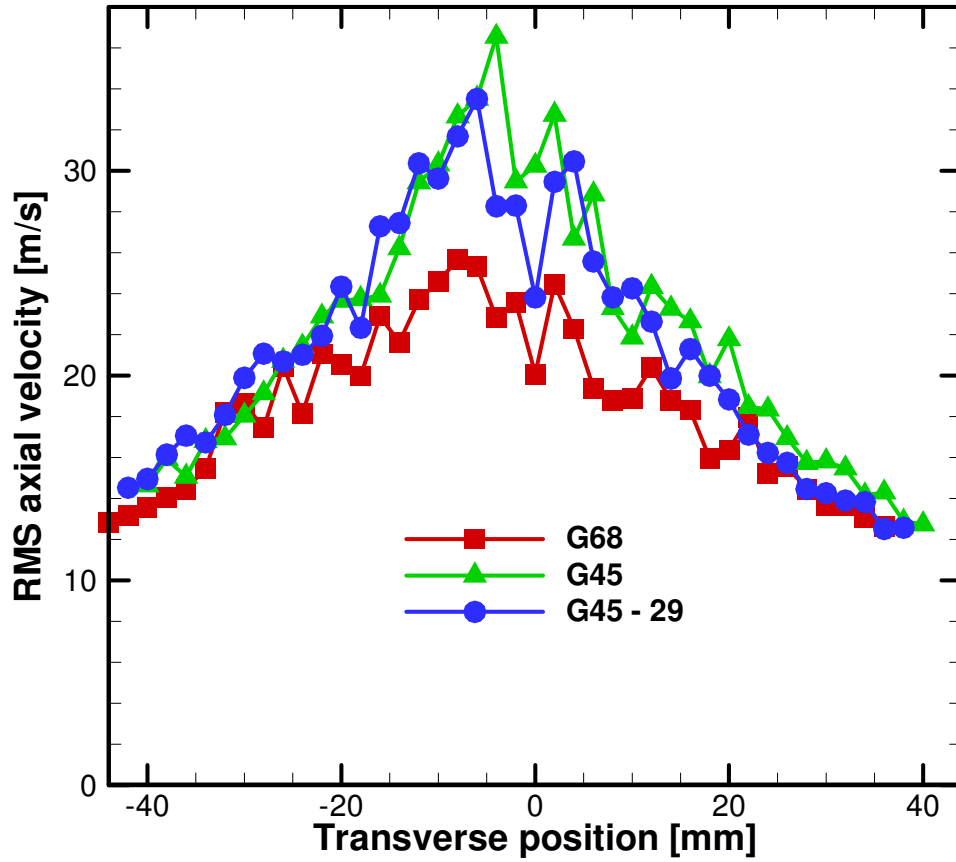


Figure 6.10 RMS axial velocity profiles of three cases

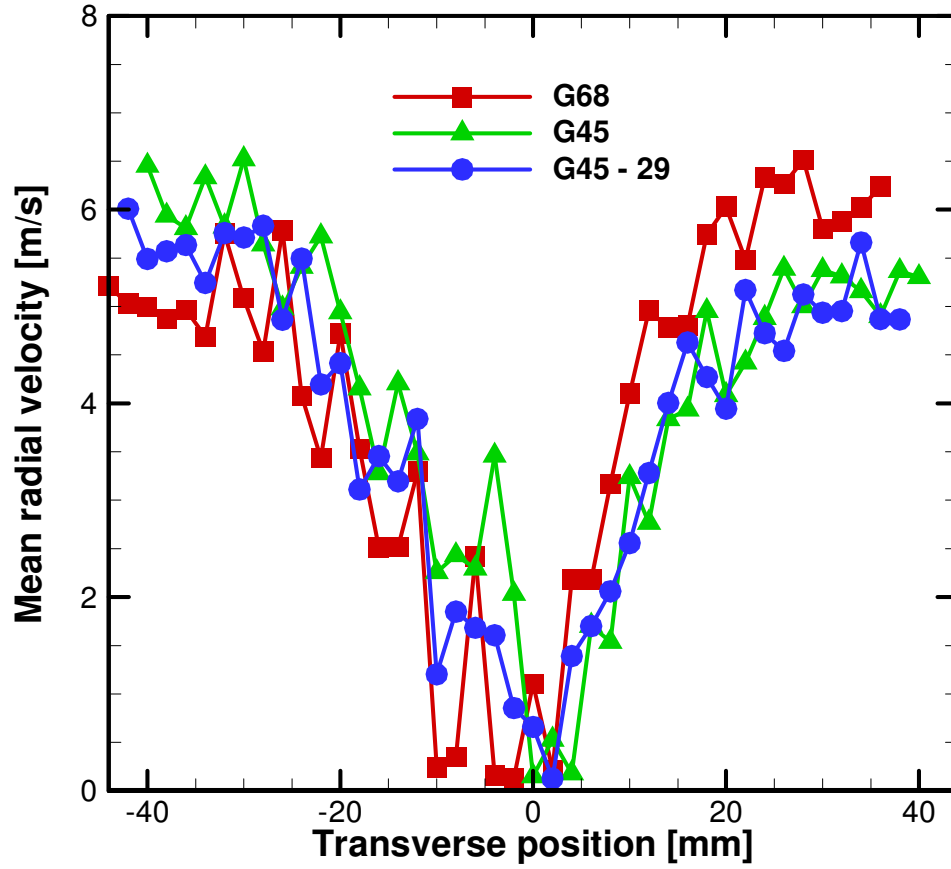


Figure 6.11 Mean radial velocity profiles of three cases

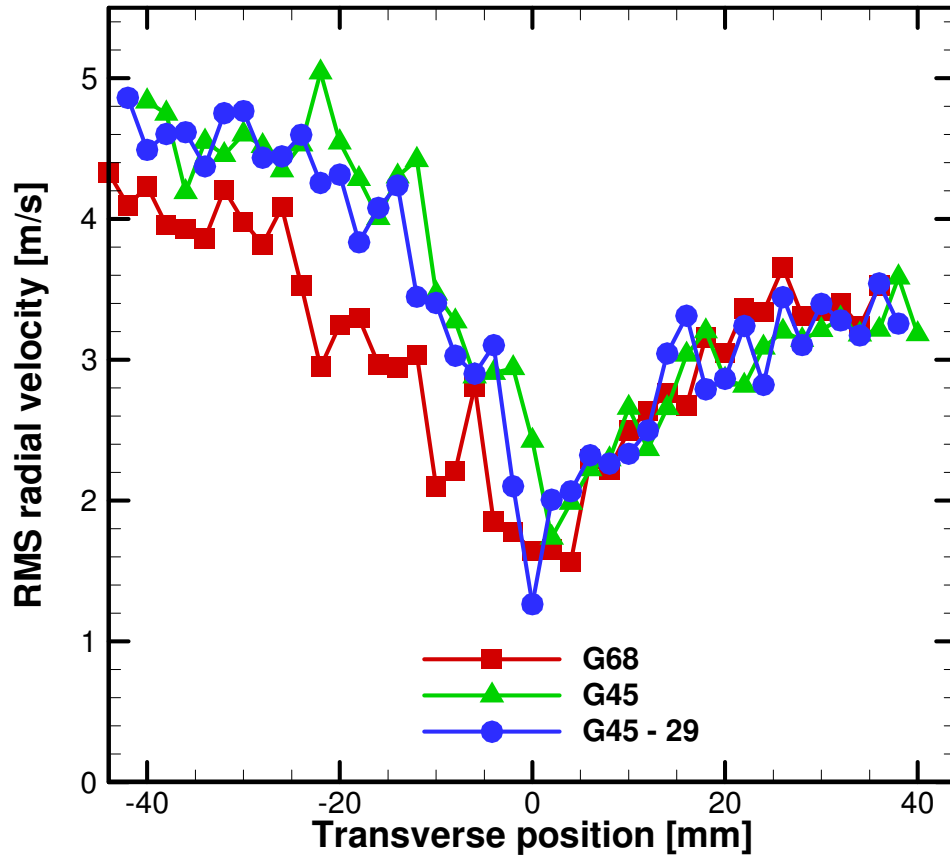


Figure 6.12 RMS radial velocity profiles of three cases

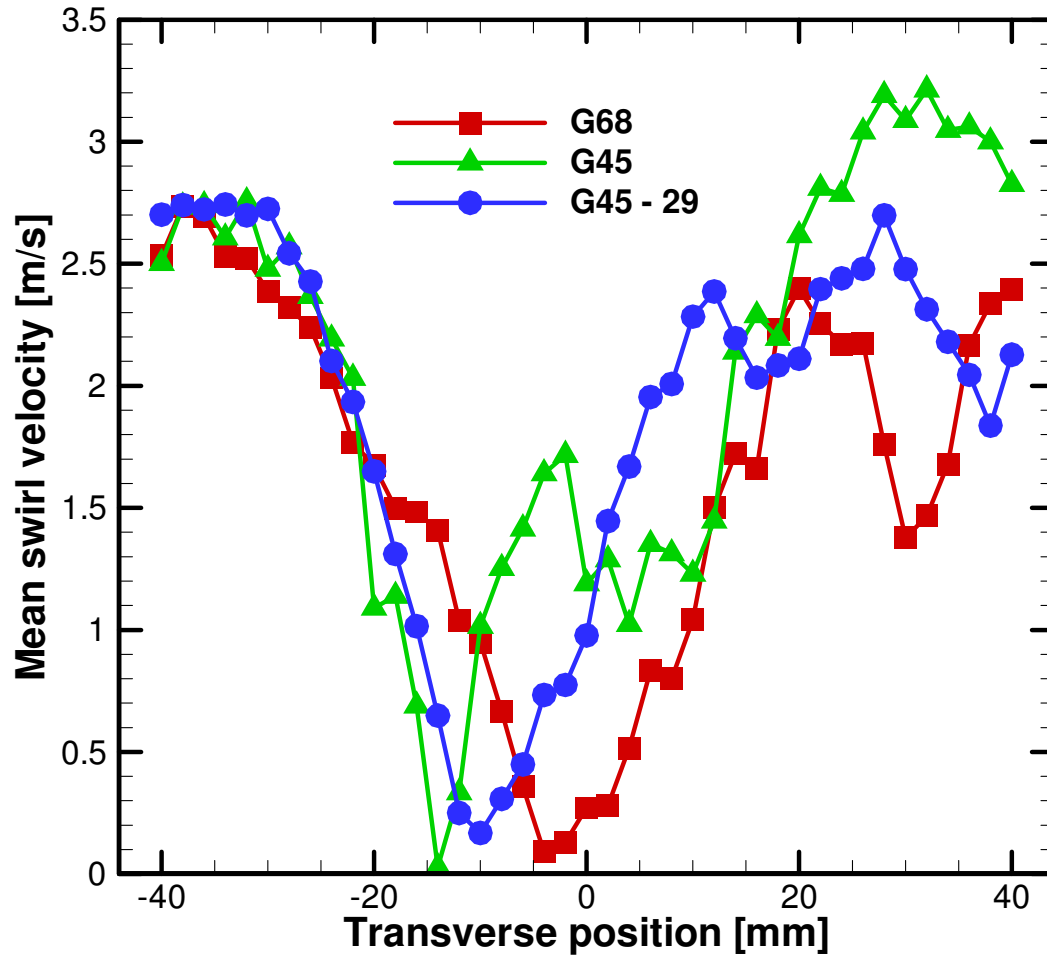


Figure 6.13 Mean swirl velocity profiles of three cases

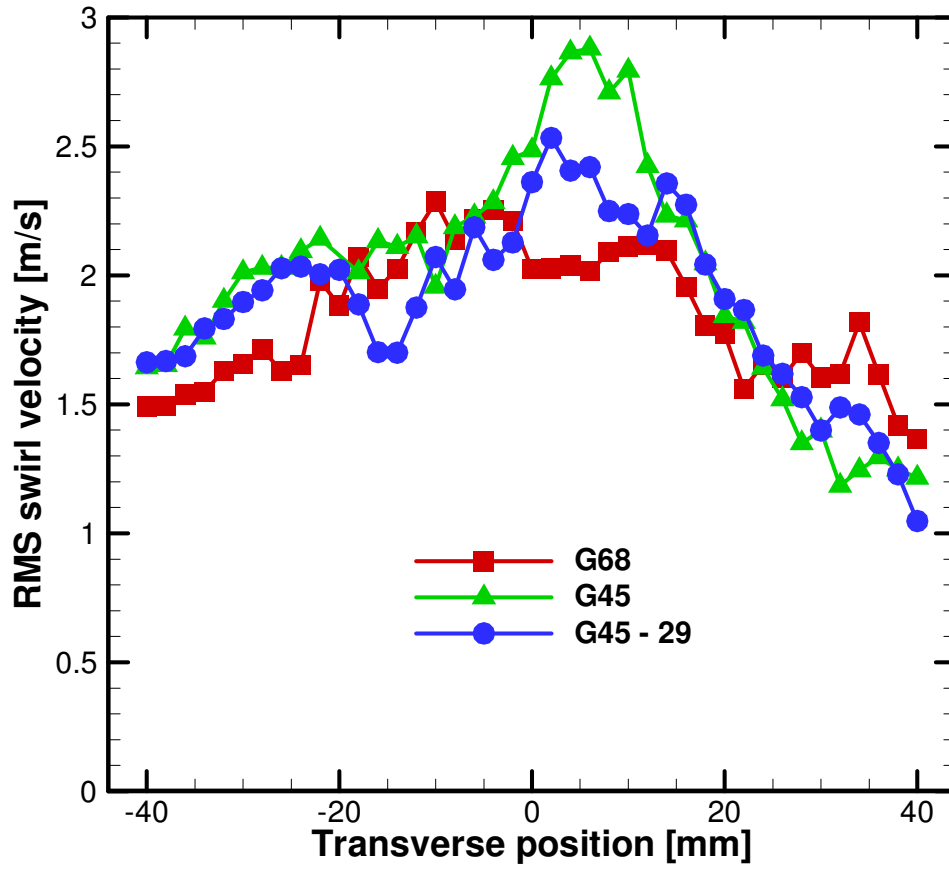


Figure 6.14 RMS swirl velocity profiles of three cases

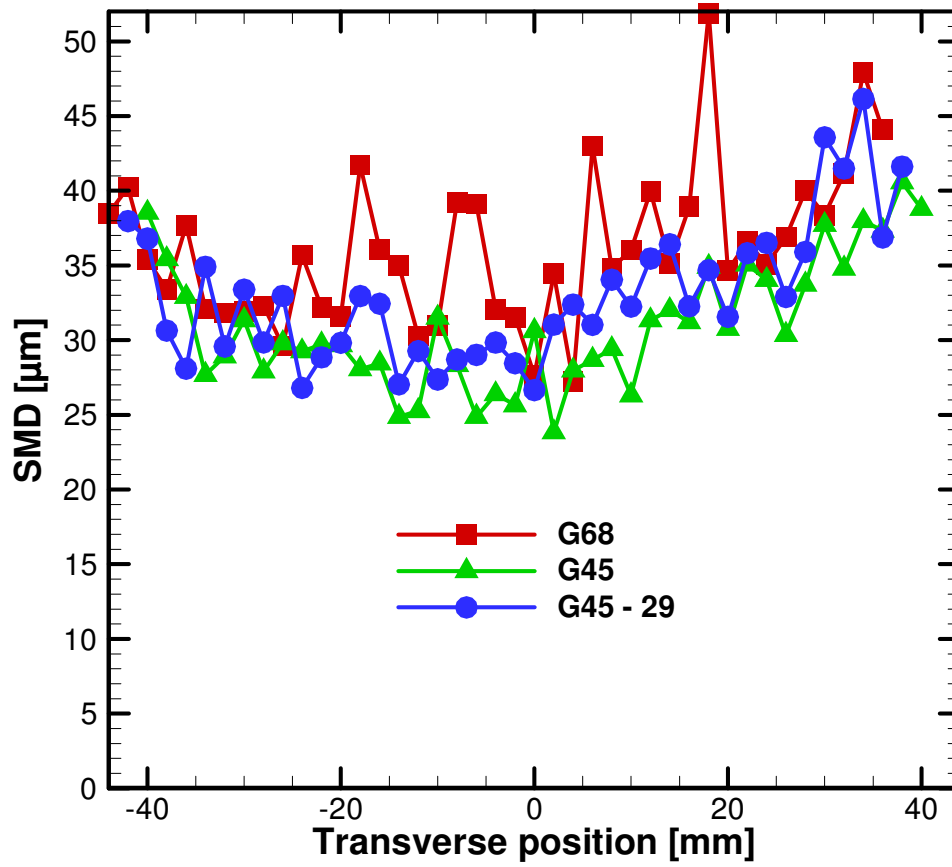


Figure 6.15 SMD profiles of three cases

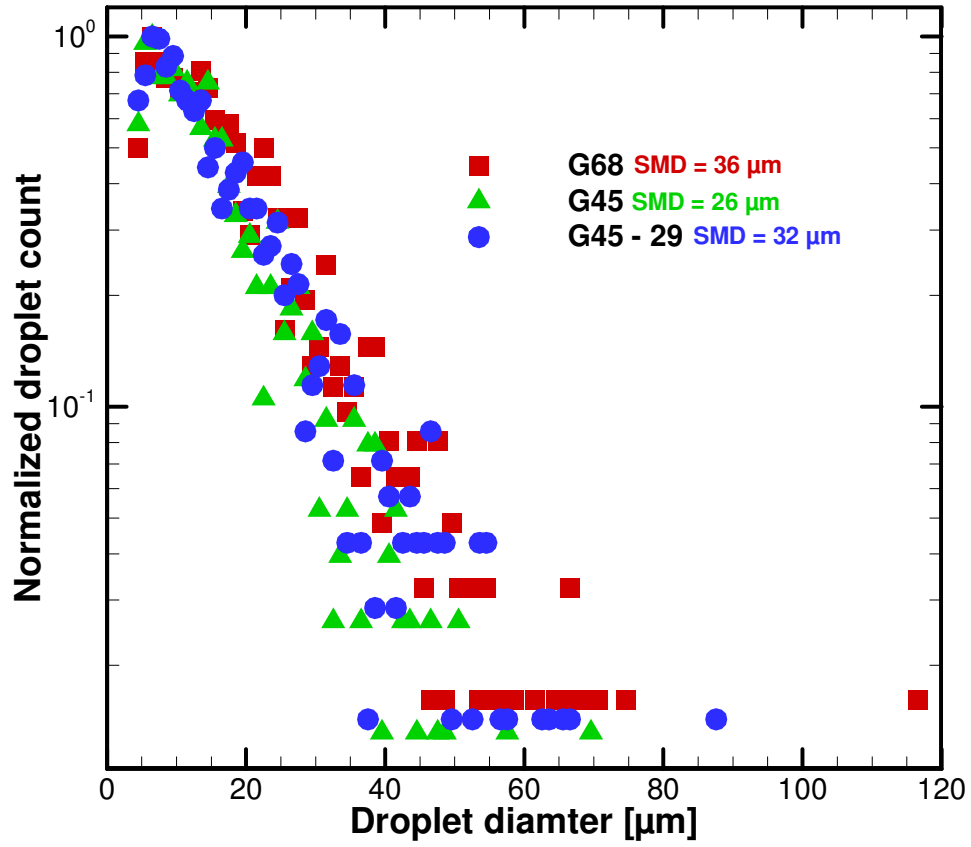


Figure 6.16 Droplet diameter distribution at R = 10 mm

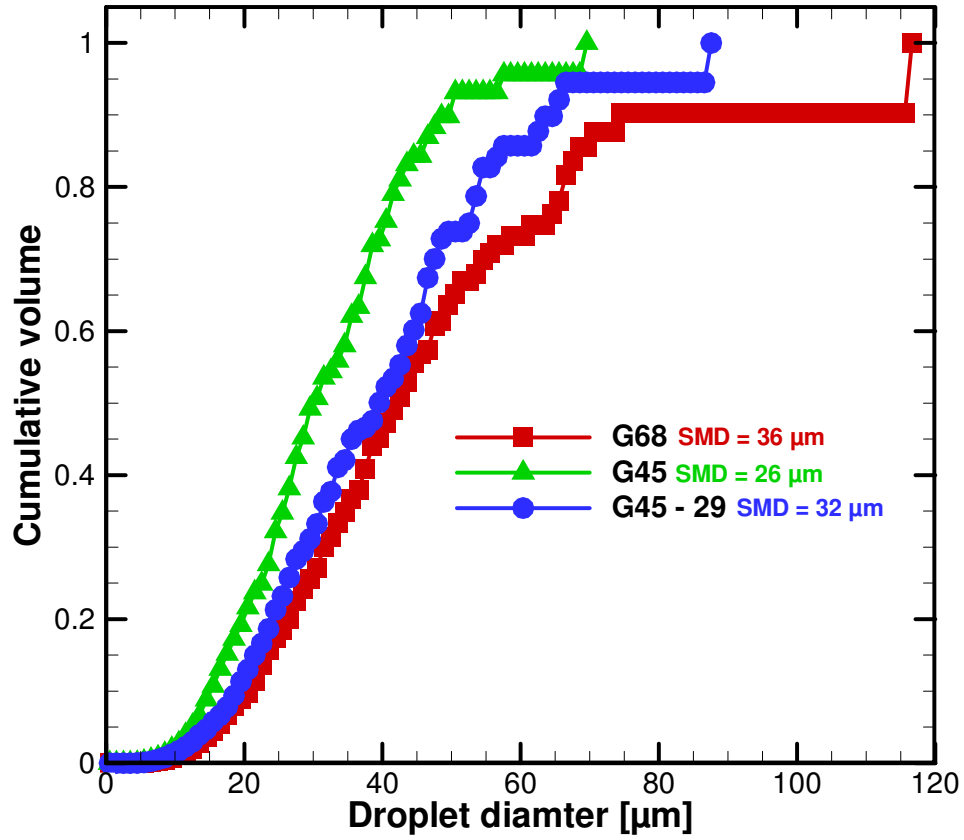


Figure 6.17 Cumulative volume distribution at R = 10 mm

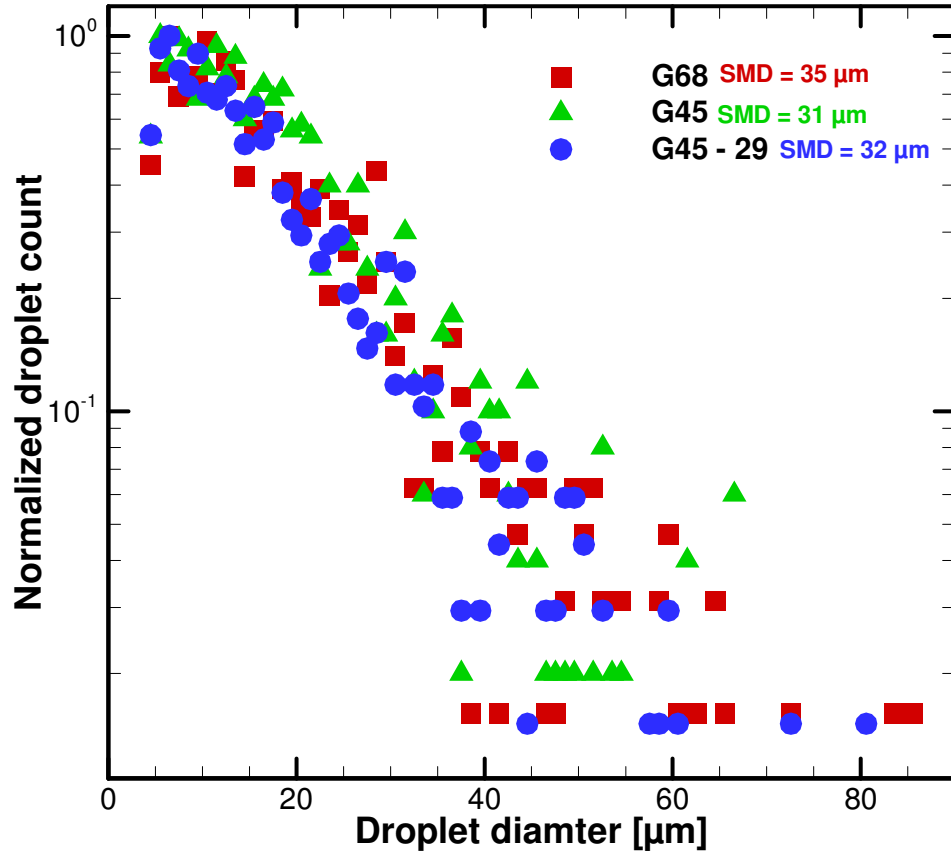


Figure 6.18 Droplet diameter distribution at R = 20 mm

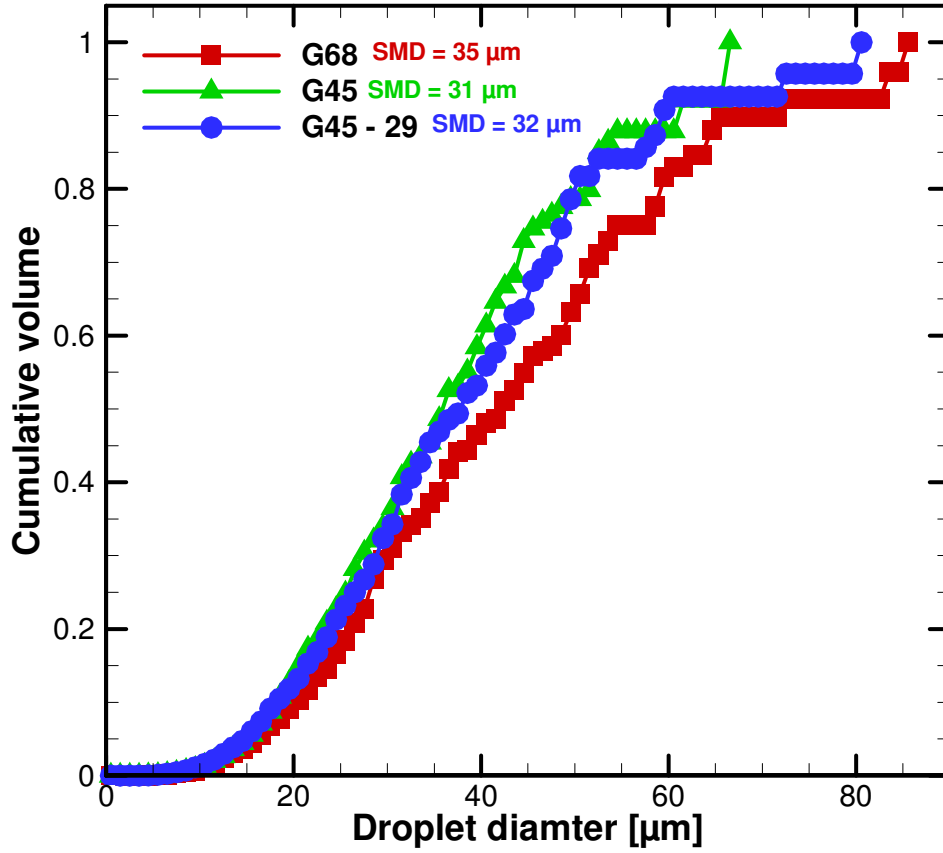


Figure 6.19 Cumulative volume distribution at R = 20 mm

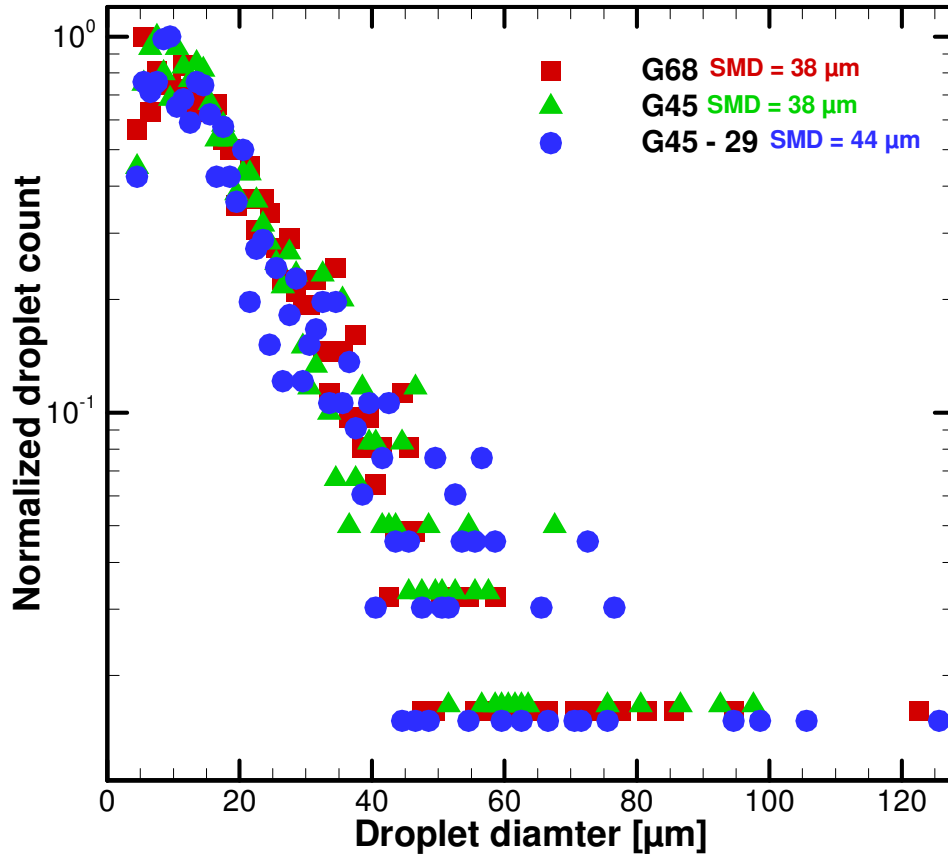


Figure 6.20 Droplet diameter distribution at R = 30 mm

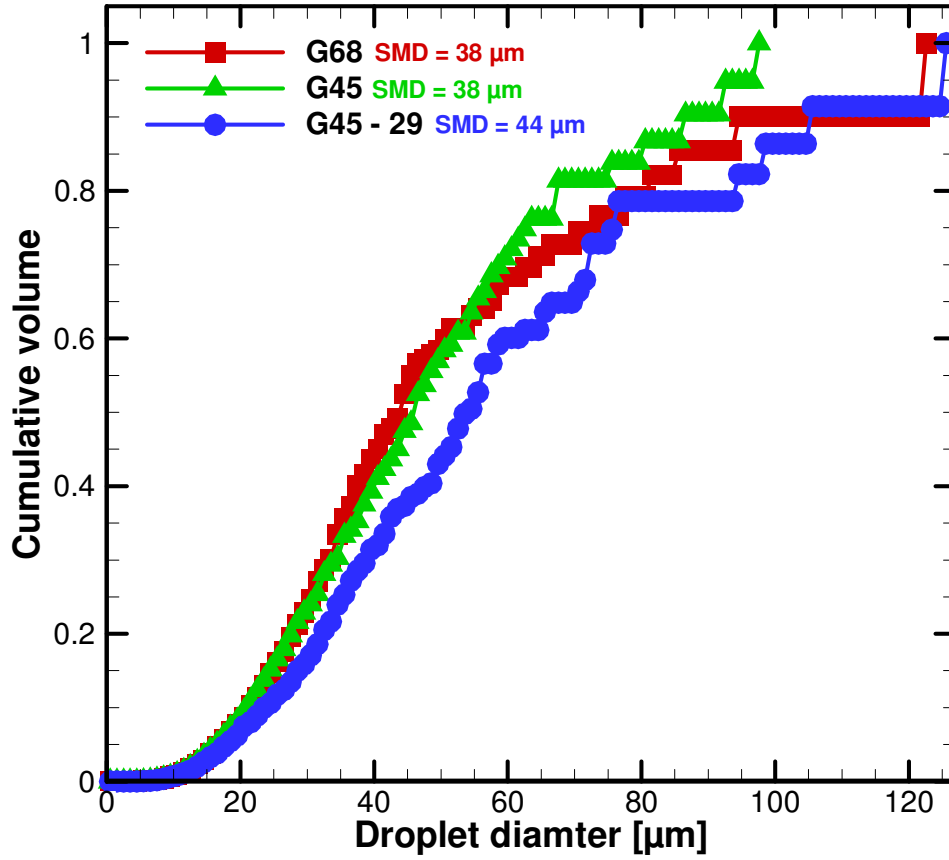


Figure 6.21 Cumulative volume distribution at R = 30 mm

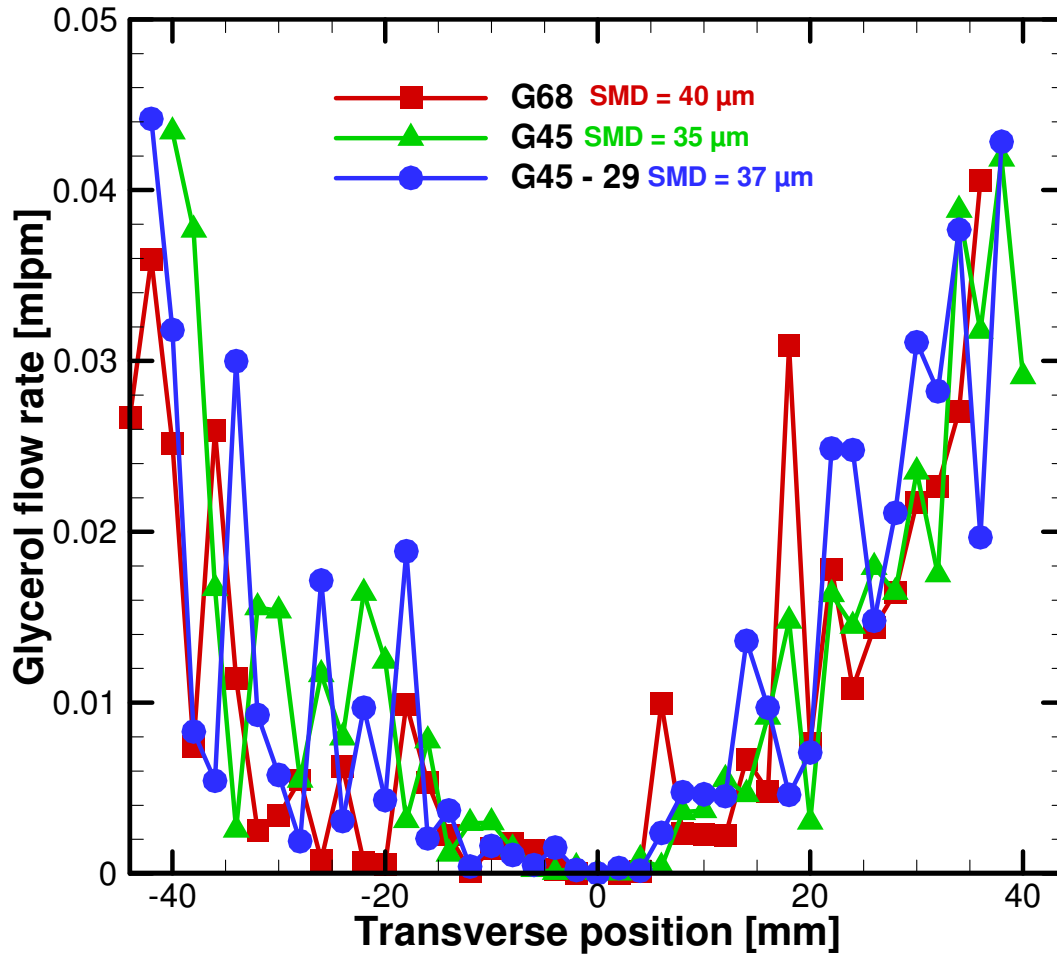


Figure 6.22 Axial glycerol volumetric flow rate as measured by PDPA

CHAPTER 7

CONCLUSIONS AND RECOMMENDATIONS

7.1 Conclusions

This study investigated the combustion performance of biodiesel, VO, and glycerol using the FB atomization technique. The FB and AB atomization concepts were then compared with each other using water as the working fluid. Next, a PDPA system was used to gather velocity and droplet diameter statistics in non-reacting diesel and VO sprays. Finally, the PDPA technique was applied to reacting glycerol flames co-fired with methane. The following conclusions were drawn from research:

- FB injector provides a simple atomization method that can drastically reduce CO and NO_x emissions as compared to AB injectors.
- FB atomization method is inherently different than AB process in that atomization mechanism is based on expansion of gas in two-phase flow instead of shear between two fluids.
- FB atomizer is capable of cleanly atomizing and combusting straight bio-oil (VO) with no fuel processing or preheating.
- FB atomizer operating with bio-oil produces lower emissions than AB atomizer operating with biodiesel, meaning that transesterification of bio-oil to produce biodiesel is unnecessary under some circumstances.

- Pressure drop in atomizing air and fuel lines in FB injector is independent of the fuel. Majority of the pressure drop results from FB mixing process instead of friction loss at walls.
- An insulated combustion environment is necessary to ensure proper heat feedback in glycerol flames.
- FB combustor can be used to atomize and combust glycerol in an insulated environment without any fuel mixing or preheating.
- Sufficient residence time within hot environment is critical to complete oxidation of glycerol.
- While co-firing glycerol with methane, the methane flow can be split between combustion and atomizing air lines to minimize emissions.
- FB atomizer produces water sprays with smaller droplets and a narrower range of droplet sizes as compared to AB atomizer.
- There reaches a point of diminishing returns where increases in ALR only very slightly reduces droplet diameter.
- FB spray angle is narrower and relatively insensitive to ALR as compared to AB atomizer.
- RMS velocities are higher in FB atomizer, indicating a more turbulent spray, as compared to AB atomizer.
- Atomizing air line pressure drop is lower in the FB atomizer than the AB atomizer for given operating conditions.

- Fuel line pressure drop is higher in the FB atomizer than the AB atomizer for given operating conditions since the fuel must overcome resistance from two-phase flow at the fuel tube exit.
- While SMD profiles are different between bio-oil (VO) and traditional fuel (diesel), when a mass flow rate-weighted SMD is considered sprays are very similar when using FB atomizer.
- G68, G45, and G45-29 flames contain sprays with flow-weighted SMDs of 40, 35, and 37 μm , respectively.

7.2 Recommendations

After all research, the following recommendations are made:

- FB injector can be optimized to determine geometric parameters to match the air and fuel flow rates.
- Experimental system can be redesigned to minimize disassembly for injector monitoring and replacement.
- An insulated enclosure for PDPA measurements can be created with minimal un-insulated area and also with cross-sectional area closest to that of circular combustor used for combustion experiments.
- A water cooled emissions probe would allow for taking emissions measurements nearer to PDPA measurements, helping to establish link between droplet sizes and emissions.
- PDPA measurements in glycerol flames difficult to obtain for following reasons:
 - Pentagonal enclosure results in significant changes in flow field that result in poor flame stabilization.

- Providing optical access results in removing insulation needed for proper thermal feedback.

REFERENCES

- # 2 diesel MSDS, <http://www.petrocard.com/Products/MSDS-ULS.pdf>, accessed on April 21, 2011.
- Alptekin, E., Canakci, M. (2009) Characterization of the key fuel properties of methyl ester-diesel fuel blends, *Fuel*, 88(1), 75-80.
- Balat, M. (2007) An overview of biofuels and policies in the European Union, *Energy Sources Part B: Economics, Planning & Policy*, 2(2), 167-181.
- Battin-Leclerc, F. (2008) Detailed chemical kinetic models for the low-temperature combustion of hydrocarbons with application to gasoline and diesel fuel surrogates, *Progress in Energy and Combustion Science*, 34(4), 440-498.
- Birouk, M. and Gokalp, I. (2006) Current status of droplet evaporation in turbulent flows, *Progress in Energy and Combustion Science*, 32(4), 408-423.
- Bolszo, C.D., McDonell, V.G. (2009a) Emissions optimization of a biodiesel fired gas turbine, *Proceedings of the Combustion Institute*, 32(2), 2949-2956.
- Bolszo, C.D., McDonell, V.G. (2009b) Evaluation of plain-jet air blast atomization and evaporation of alternative fuels in a small gas turbine engine application, *Atomization and Sprays*, 19(8), 771-785.
- Chiu, H. H. (2000) Advances and challenges in spray combustion. I. Toward a unified theory of droplet aerothermochemistry, *Progress in Energy and Combustion Science*, 26(4), 381-416.
- Clack, H.L., Koshland, C.P., Lucas, D., Sawyer, R.F. (2004) Development of an air-blast atomizer for independent control of droplet size and spray density, *Atomization and Sprays*, 14(3), 265-288.
- CRC Handbook of Chemistry and Physics, <http://www.hbcnetbase.com/>, accessed on January 13, 2011.
- Demirbas, A. (2006) Biodiesel production via non-catalytic SCF method and biodiesel fuel characteristics, *Energy Conversion and Management*, 47(15), 2271-2282.
- Diesel physical properties, <http://www.matbase.com/material/other/fuel/diesel/properties>, accessed on February 10, 2011.

- Duncan, M. (2003) U.S. federal initiatives to support biomass research and development, *Journal of Industrial Ecology*, 7(3), 193-201.
- Faeth, G. M., Hsiang, L.P., Wu, P.K. (1995) Structure and breakup properties of sprays, *International Journal of Multiphase Flow*, 21(1), 99-127.
- Fisher, E.M., Pitz, W.J., Curran, H.J., Westbrook, C.K. (2000) Detailed chemical kinetic mechanisms for combustion of oxygenated fuels, *Proceedings of the Combustion Institute*, 28(2), 1579-1586.
- Fuel table, <http://www.afdc.energy.gov/afdc/pdfs/fueltable.pdf>, accessed on April 3, 2011.
- Gañán-Calvo, A.M. (2005) Enhanced liquid atomization: from flow focusing to flow-blurring, *Applied Physics Letters*, 86, 214101.
- Glaude, P.A., Fournet, R., Bounaceur, R., Molière, M. (2010) Adiabatic flame temperature from biofuels and fossil fuels and derived effect on NO_x emissions, *Fuel Processing Technology*, 91(2), 229-235.
- Glycerol MSDS, <http://www.jtbaker.com/msds/englishhtml/g4774.htm>, accessed on April 21, 2011.
- Graboski, M.S., McCormick, R.L. (1998) Combustion of fat and vegetable oil derived fuels in diesel engines, *Progress in Energy and Combustion Science*, 24(2), 125-164.
- Han, Y. M., Seol, W. S., Lee, D. S., Yagodkin, V. I., Jeung, I. S. (2001) Effects of fuel nozzle displacement on pre-filming airblast atomization, *Journal of Engineering for Gas Turbines and Power*, 123(1), 33-40.
- Herbinet, O., Pitz, W.J., Westbrook, C.K. (2008) Detailed chemical kinetic oxidation mechanism for a biodiesel surrogate, *Combustion and Flame*, 154(3), 507-528.
- Herbinet, O., Pitz, W.J., Westbrook, C.K. (2010) Detailed chemical kinetic mechanism for the oxidation of biodiesel fuels blend surrogate, *Combustion and Flame*, 157(5), 893-908.
- Hoeg, D.P., Wang, Z., Friedman, P.D., Laoulache, R.N. (2008) Investigation of a coaxial air-blast atomizer using particle image velocimetry and computational fluid dynamics, *Atomization and Sprays*, 18(8), 739-759.
- Karl, J.J., Huilier, D., Burnage, H. (1996) Mean behavior of a coaxial air-blast atomized spray in a co-flowing air stream, *Atomization and Sprays*, 6(4), 409-433.
- Kuo, K. K. Ed. (1996a) *Recent Advances in Spray Combustion, Volume I: Spray Atomization and Drop Burning Phenomena*, AIAA, Virginia.
- Kuo, K. K. Ed. (1996b) *Recent Advances in Spray Combustion, Volume II: Spray Combustion Measurements and Model Simulation*, AIAA, Virginia.

- Lefebvre, A. H. (1989) *Atomization and Sprays*, Hemispheres, New York, 136-141.
- Lefebvre, A.H. (1992) Twin fluid atomization: factors influencing mean drop size, *Atomization and Sprays*, 2(2), pp. 101-119.
- Lefebvre, A. H., Ballal, D. R. (2010) *Gas Turbine Combustion: Alternative Fuels and Emissions*, CRC Press, Boca Raton, 443-511.
- Li, T.X., Zhu, D.L., Akafuah, N.K., Saito, K., Law, C.K. (2011) Synthesis, droplet combustion, and sooting characteristics of biodiesel produced from waste vegetable oils, *Proceedings of the Combustion Institute*, 33(2), 2039-2046.
- Misra, R.D., Murthy, M.S. (2010) Straight vegetable oils usage in a compression ignition engine- a review, *Renewable and Sustainable Energy Reviews*, 14(9), 3005-3013.
- Moliere, M. (2005) Expanding fuel flexibility of gas turbines, *Proceedings of the Institution of Mechanical Engineers, Part A: Power & Energy*, 219(2), 109-119.
- Moliere, M., Panarotto, E., Aboujaib, M., Bisseaud, J.M., Campbell, A., Citeno, J., Maire, P., Ducrest, L. (2007) Gas turbines in alternative fuel applications: biodiesel field test, *ASME Conference Proceedings*, 2007(4790X), 397-406.
- Pan, K.L., Li, J.W., Chen C.P., Wang, C.H. (2009) On droplet combustion of biodiesel fuel mixed with diesel/alkanes in microgravity condition, *Combustion and Flame*, 156(10), 1926-1936.
- Panchasara, H., Sequera, D., Schreiber, W., Agrawal, A.K. (2009a) Combustion performance of a novel injector using flow-blurring for efficient fuel atomization, *Journal of Propulsion and Power*, 25(4), 984-987.
- Panchasara, H. V., Simmons, B. M., Agrawal, A. K. (2009b) Combustion performance of biodiesel and diesel-vegetable oil blends in a simulated gas turbine burner, *Journal of Engineering for Gas Turbines and Power*, 131(3), 031503:1-11.
- Park, S.H., Cha, J., Lee, C.S. (2011) Spray and engine performance characteristics of biodiesel and its blends with diesel and ethanol fuels, *Combustion Science and Technology*, 183(8), 802-822.
- Qi, D.H., Chen, H., Geng, L.M., Bian, Y.ZH., Ren, X.CH. (2010) Performance and combustion characteristics of biodiesel–diesel–methanol blend fuelled engine, *Applied Energy*, 87(5), 1679-1686.
- Raghavan, V., Rajesh, S., Parag, S., Avinash, V. (2009) Investigation of combustion characteristics of biodiesel and its blends, *Combustion Science and Technology*, 181(6), 877-891.
- Rakopoulos, C.D., Antonopoulos, K.A., Rakopoulos, D.C. (2007) Development and application of multi-zone model for combustion and pollutants formation in direct injection diesel

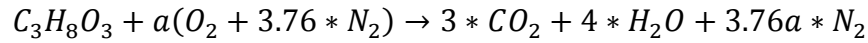
- engine running with vegetable oil or its bio-diesel, *Energy Conversion Management*, 48(7), 1881-1901.
- Rizk, N. K., Lefebvre, A. H. (1984) Spray characteristics of plain-jet airblast atomizers, *Journal of Engineering for Gas Turbines and Power*, 106(3), 634–638.
- Rizk, N. K., Mongia, H. C. (1992) Calculation approach validation for airblast atomizers, *Journal of Engineering for Gas Turbines and Power*, 114(2), 386-394.
- Rosell-Llompart, J., Gañán-Calvo, J. M. (2008) Turbulence in pneumatic flow focusing and flow blurring regimes, *Physical Review E*, 77(3), 036321:1-10.
- Sadasivuni, V., Agrawal, A.K. (2009) A novel meso-scale combustion concept for operation with liquid fuels, *Proceedings of the Combustion Institute*, 32(2), 3155-3162.
- Sahin, Z. Durgum, O. (2007) Theoretical investigation of effects of light fuel fumigation on diesel engine performance and emissions, *Energy Conversion and Management*, 48(7), 1952-1964.
- Santos, J.C.O., Santos, M.G.O., Dantas, J.P., Conceição, M.M., Athaide-Filho, P.F., Souza, A.G. (2005) Comparative study of specific heat capacities of some vegetable oils obtained by DSC and microwave oven, *Journal of Thermal Analysis and Calorimetry*, 79(2), 283-287.
- Schwab, A.W., Dykstra, G.J., Selke, E., Sorenson, S.C., Pryde, E.H. (1988) Diesel fuel from thermal decomposition of soybean oil, *Journal of the American Oil Chemists' Society*, 65(11), 1781-1786.
- Simmons, B.M., Panchasara, H.V., Agrawal, A.K. (2008) Effect of fuel injection concept on combustion performance of liquid biofuels, *Session B3: Biofuels*, 2008 Technical Meeting of the Central States Section of the Combustion Institute, April 20-22, Tuscaloosa, AL.
- Simmons, B.M., Panchasara, H.V., Agrawal, A.K. (2009) A comparison of air-blast and flow-blurring injectors using phase Doppler particle analyzer techniques, *ASME Conference Proceedings*, 2009(48838), 981-992.
- Simmons, B.M., Agrawal, A.K. (2011) Spray characteristics of a flow-blurring atomizer, *Atomization and Sprays*, 20(9), 821-825.
- Sirignano, W.A., Mehring, C. (2000) Review of theory of distortion and disintegration of liquid streams, *Progress in Energy and Combustion Science*, 26(4-6), 609-655.
- Sirignano, W.A. (2005) Volume averaging for the analysis of turbulent spray flows, *International Journal of Multiphase Flow*, 31(6), 675-705.
- Song, J., Alam, M., Boehman, A.L. (2007) Impact of alternative fuels on soot properties and DPF regeneration, *Combustion Science and Technology*, 179(9), 1991-2037.

- Sovani, S. D., Sojka, P. E., Lefebvre, A. H. (2001), Effervescent atomization, *Progress in Energy and Combustion Science*, 27(4), 483-521.
- Soybean oil MSDS, <http://www.sciencelab.com/msds.php?msdsId=9925064>, accessed on February 10, 2011.
- Specific heat table, <http://www.armstronginternational.com/files/common/allproductscatalog/cg-53.pdf>, accessed on April 3, 2011.
- Tsai, S. C., Viers, B. (1992) Airblast atomization of viscous Newtonian liquids using twin-fluid jet atomizers of various designs, *Journal of Fluids Engineering*, 114(1), 113-118.
- Tyner, W. E. (2008) The US ethanol and biofuels boom: its origins, current status, and future prospects, *Bioscience*, 58(7), 646-653.
- Turns, S.R. (2000) *An Introduction to Combustion, 2nd ed.*, McGraw-Hill Higher Education, USA, 256.
- Wang, X., Huang, Z., Kuti, O.A., Zhang, W., Nishida, K. (2011) An experimental investigation on spray, ignition and combustion characteristics of biodiesels, *Proceedings of the Combustion Institute*, 33(2), 2071-2077.
- Zheng, Q. P., Jasuja, A. K., Lefebvre, A. H. (1997) Structure of airblast sprays under high ambient pressure conditions, *Journal of Engineering for Gas Turbines and Power*, 119(3), 512-518.

APPENDIX A

EQUIVALENCE RATIO CALCULATION

The chemical formula for glycerol is given as $C_3H_8O_3$. Air is taken to be 79% nitrogen and 21% oxygen on a molar basis ($O_2 + 3.76N_2$). Assuming complete stoichiometric combustion with no dissociation, the reaction formula of one mole (or kmol) of glycerol is given by:

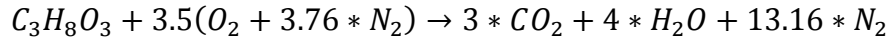


Solving for the variable a by balancing O atoms gives:

$$2 * a + 3 = 3 * 2 + 4$$

$$a = 3.5$$

The stoichiometric equation becomes:



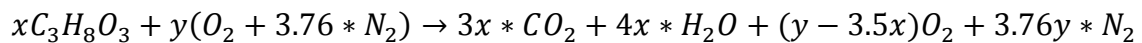
This gives a stoichiometric molar air to fuel ratio $(\overline{A/F})_{\phi=1}$ of:

$$(\overline{A/F})_{\phi=1} = \frac{(N \text{ air})}{(N \text{ fuel})} = \frac{(3.5 * 4.76 \text{ kmol})}{(1 \text{ kmol})} = 16.66 \frac{\text{kmol}}{\text{kmol}}$$

Expressing this as the stoichiometric mass air to fuel ratio $(A/F)_{\phi=1}$ gives:

$$(A/F)_{\phi=1} = \frac{(N \text{ air})(MW \text{ air})}{(N \text{ fuel})(MW \text{ fuel})} = \frac{(3.5 * 4.76 \text{ kmol}) \left(28.85 \frac{\text{kg}}{\text{kmol}}\right)}{(1 \text{ kmol}) \left(92.1 \frac{\text{kg}}{\text{kmol}}\right)} = 5.219 \frac{\text{kg}}{\text{kg}}$$

For lean combustion, the reaction equation is given by:



where x and y are the molar flow rates of glycerol and air, respectively. For the experiments, glycerol flow rate was constrained at 21 mlpm and air at 150 slpm. Calculating x and y :

$$x = \left(21 \frac{\text{milliliters}}{\text{minute}}\right) \left(\frac{\text{m}^3}{10^6 \text{milliliters}}\right) \left(1260 \frac{\text{kg}}{\text{m}^3}\right) \left(\frac{\text{kmol}}{92.1 \text{kg}}\right) = 0.0002873 \frac{\text{kmol}}{\text{min}}$$

$$y = \left(150 \frac{\text{liters}}{\text{minute}}\right) \left(\frac{\text{m}^3}{10^3 \text{liters}}\right) \left(1.18 \frac{\text{kg}}{\text{m}^3}\right) \left(\frac{\text{kmol}}{28.85 \text{kg}}\right) = 0.006135 \frac{\text{kmol}}{\text{min}}$$

This gives an actual molar air to fuel ratio of:

$$(\overline{A/F}) = \frac{y}{x} = \frac{0.006135 \frac{\text{kmol}}{\text{min}}}{0.0002873 \frac{\text{kmol}}{\text{min}}} = 21.35 \frac{\text{kmol}}{\text{kmol}}$$

Dividing the stoichiometric molar air to fuel ratio by this value will give the equivalence ratio:

$$\Phi = \frac{(\overline{A/F})_{\Phi=1}}{(\overline{A/F})} = \frac{16.66}{21.35} = 0.78$$

Alternatively x , y , and Φ can be calculated on a mass (instead of molar) basis:

$$x = \left(21 \frac{\text{milliliters}}{\text{minute}}\right) \left(\frac{\text{m}^3}{10^6 \text{milliliters}}\right) \left(1260 \frac{\text{kg}}{\text{m}^3}\right) = 0.02646 \frac{\text{kg}}{\text{min}}$$

$$y = \left(150 \frac{\text{liters}}{\text{minute}}\right) \left(\frac{\text{m}^3}{10^3 \text{liters}}\right) \left(1.18 \frac{\text{kg}}{\text{m}^3}\right) = 0.177 \frac{\text{kg}}{\text{min}}$$

$$(A/F) = \frac{y}{x} = \frac{0.177 \frac{\text{kg}}{\text{min}}}{0.02646 \frac{\text{kg}}{\text{min}}} = 6.689 \frac{\text{kg}}{\text{kg}}$$

$$\Phi = \frac{(A/F)_{\Phi=1}}{(A/F)} = \frac{5.219}{6.689} = 0.78$$

APPENDIX B

REYNOLDS NUMBER CALCULATION

Reynolds number (Re) is used as a means determining the ratio of inertial to viscous forces and is given by the following expression:

$$Re = \frac{\rho UL}{\mu}$$

where ρ is the fluid density, U is the mean fluid velocity, L is a characteristic length dependent on the circumstances, and μ is the fluid dynamic viscosity. When calculating Re for flows in annular regions, the characteristic length is the hydraulic diameter, D_H , the difference between the outer and inner diameters.

For this combustor, Re will be calculated at the point where the air enters the swirler before entering the combustion chamber. In this case, air is the working fluid with the following properties:

$$\rho_{air} = 1.18 \frac{kg}{m^3}$$

$$\mu_{air} = 1.983 * 10^{-5} \frac{kg}{m * s}$$

The inner and outer diameters were measured as 0.0409 m and 0.0159 m, respectively, giving a hydraulic diameter of 0.0250 m. The mean air velocity is calculated by dividing the volumetric air flow by the annular cross sectional area:

$$U = \frac{Q}{A} = \frac{Q}{(\pi/4)(D_o^2 - D_i^2)} = \frac{(125 \frac{liters}{min}) (\frac{m^3}{1000 liters}) (\frac{min}{60 sec})}{(\frac{\pi}{4}) [(0.0409m)^2 - (0.0159m)^2]} = 1.87 \frac{m}{s}$$

These values give Re:

$$Re = \frac{\rho UL}{\mu} = \frac{\left(1.18 \frac{kg}{m^3}\right) \left(1.87 \frac{m}{s}\right) (0.025 m)}{1.983 * 10^{-5} \frac{kg}{m * s}} = 2781$$

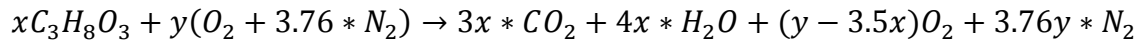
APPENDIX C

EQUIVALENCE RATIO VALIDATION

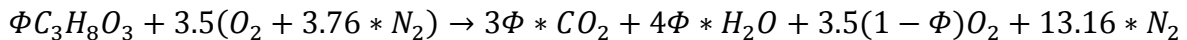
Equivalence ratios calculated from measured air and fuel flow rates will be compared to equivalence ratios calculated from the measured quantities of oxygen and carbon dioxide in the combustion products. For this comparison to be valid, it is assumed that all fuel reacts to form carbon dioxide and water and that there is no dissociation of combustion products. Glycerol and air flow rates were chosen as 21 mlpm and 150 slpm, respectively. As discussed in appendix A, this gives an equivalence ratio calculated from flow rates as:

$$\Phi = 0.78$$

As discussed in appendix A, the lean combustion reaction of glycerol is given by:



The coefficients in this equation can be rewritten in terms of Φ :



The coefficients in the products can be used to calculate the dry molar percentage of products:

$$X_{CO_2} = \frac{3\Phi}{3\Phi + 3.5(1 - \Phi) + 13.16}$$

$$X_{O_2} = \frac{3.5(1 - \Phi)}{3\Phi + 3.5(1 - \Phi) + 13.16}$$

$$X_{N_2} = \frac{13.16}{3\Phi + 3.5(1 - \Phi) + 13.16}$$

The dry composition of product gases was measured during experiments as a means of confirming equivalence ratio. As an example, the following values were measured at an experimental point:

$$X_{CO_2} = 14.4$$

$$X_{O_2} = 5.0$$

These values can be plugged into the previous equations and used to solve for an equivalence ratio based on product gas measurement:

$$14.4 = \frac{3\Phi_{CO_2}}{3\Phi_{CO_2} + 3.5(1 - \Phi_{CO_2}) + 13.16}$$

$$5.0 = \frac{3.5(1 - \Phi_{O_2})}{3\Phi_{O_2} + 3.5(1 - \Phi_{O_2}) + 13.16}$$

Solving gives:

$$\Phi_{CO_2} = 0.78$$

$$\Phi_{O_2} = 0.77$$

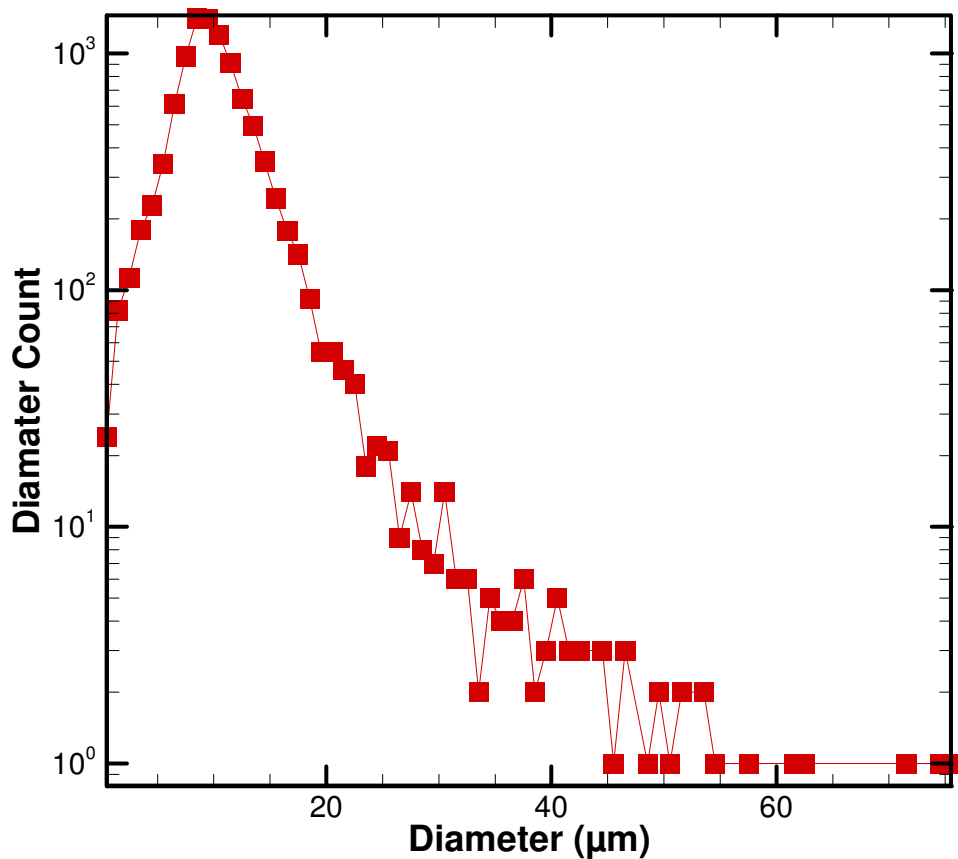
These values show that the product gas measurements corroborate the equivalence ratio calculated based on flow rates.

APPENDIX D

UNCERTAINTY ANALYSIS

It can be difficult to quantify the error in phase Doppler particle analyzer (PDPA) measurements. As a means to express this error, statistical methods can be applied. Using the mean, standard deviation, sample size, and desired confidence level, a type of uncertainty can be applied to a set of data. For example, a 99% confidence interval means that if an experimental point is repeated infinitely the true mean will occur in the interval 99% of the time.

This method can be applied to the PDPA data seen in the following figure.



Even though this data is not a normal distribution, this technique can still be applied to get approximate confidence intervals. The first step is to calculate the mean for the sample data:

$$\bar{x} = \frac{\sum x_i}{n} = \frac{104,419}{10,000} = 10.44\mu\text{m}$$

Next, the standard deviation is calculated:

$$s = \sqrt{\frac{\sum x_i^2 - \frac{(\sum x_i)^2}{n}}{n - 1}} = \sqrt{\frac{1,324,319 - \frac{(104,419)^2}{10,000}}{9,999}} = 4.84\mu\text{m}$$

Then a confidence interval is calculated based on a desired confidence interval, here 99%:

$$\bar{x} \pm z_{\alpha/2} \frac{s}{\sqrt{n}} = 10.44 \pm 2.576 * \frac{4.84}{\sqrt{10,000}} = 10.44\mu\text{m} \pm 0.12\mu\text{m}$$

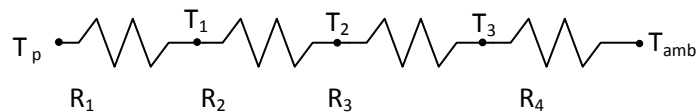
The following table presents the instrument uncertainties for other equipment used.

| Instrument | Purpose | Reported Uncertainty |
|---------------------------------------|--------------------------|-----------------------------|
| Cole Parmer peristaltic pump | Liquid fuel | ±0.25% reading |
| Laminar flow element | Primary air | ±5 slpm |
| Sierra 810 mass flow controller | Atomizing air | ±0.75 slpm |
| Sierra SmartTrak mass flow controller | Methane | ±0.5 slpm |
| Sierra SmartTrak mass flow controller | Methane through injector | ±0.5 slpm |
| NOVA emissions analyzer | CO and NO _x | ±2 ppm |

APPENDIX E

INSULATION THICKNESS DETERMINATION

For the glycerol combustion experiments, preliminary calculations were performed to assess an acceptable insulation thickness. Using the electrical resistance technique for heat transfer, the following model can be formed:



where,

T_p = temperature of the product gases

T_1 = temperature of the inner surface of quartz enclosure

T_2 = temperature at quartz enclosure/ insulation interface

T_3 = temperature of outer surface of insulation

T_{amb} = temperature of ambient air

R_1 = resistance due to forced convection on interior of quartz enclosure

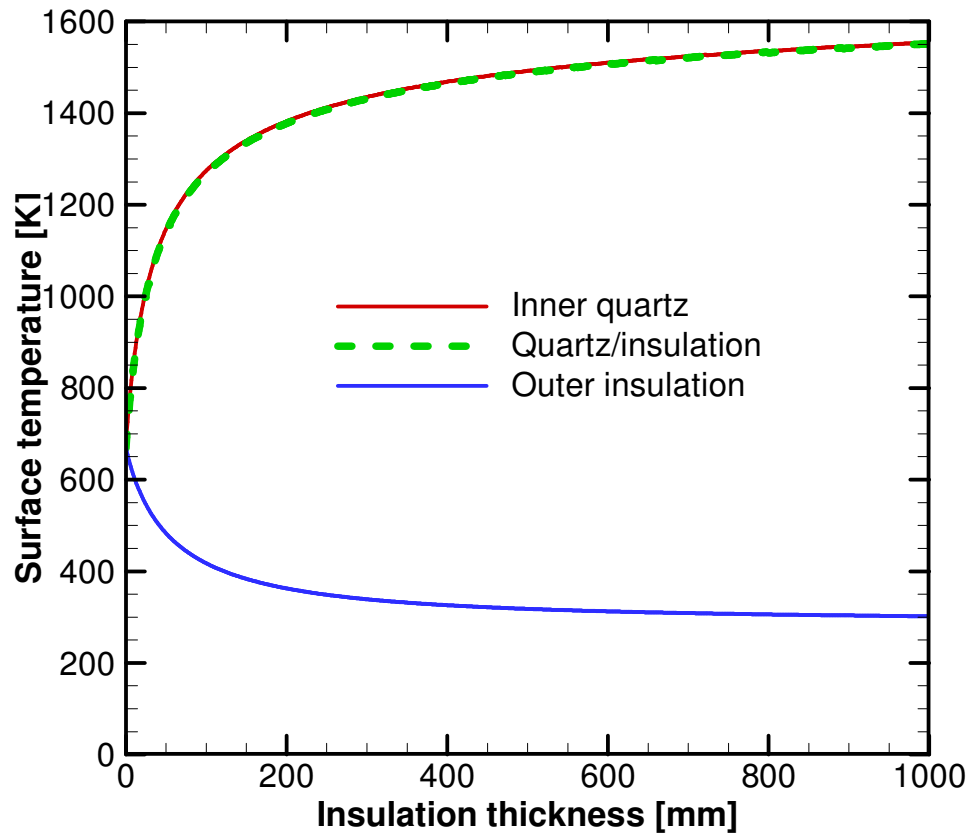
R_2 = resistance due to conduction through quartz enclosure

R_3 = resistance due to conduction through insulation

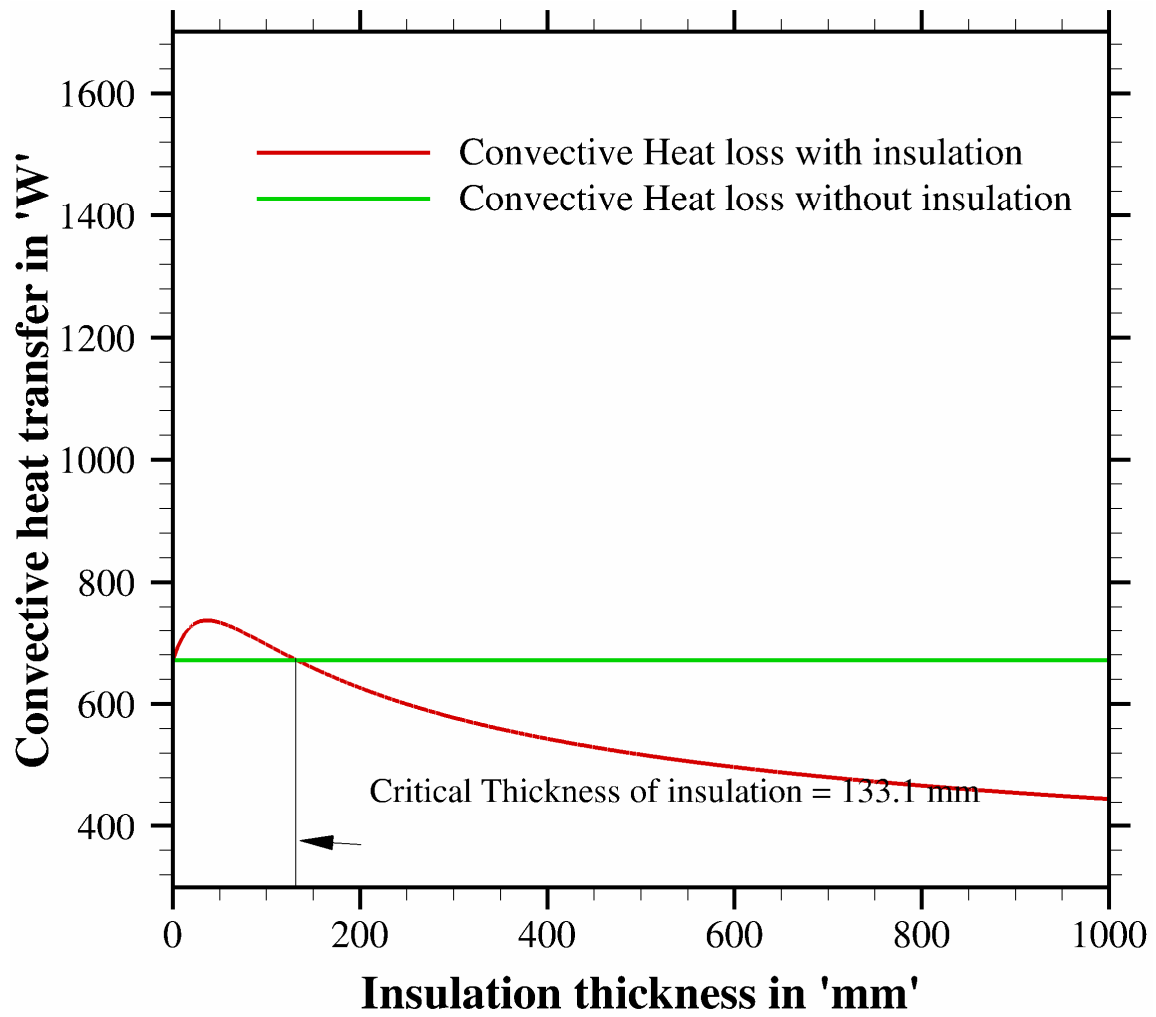
R_4 = resistance due to natural convection on exterior of insulation

All material properties are known. T_p assumed to be 1900 K from equilibrium calculations. T_{amb} assumed to be 288 K. Natural convection on outside of insulation assumed to be $5 \text{ W/m}^2\text{K}$.

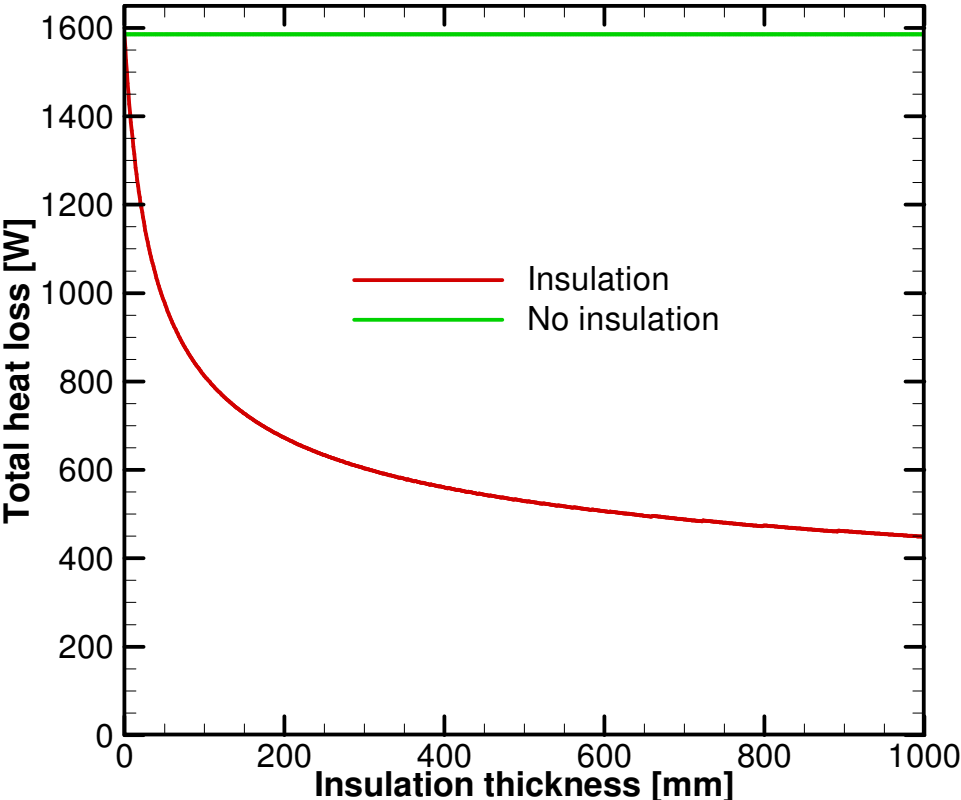
Resulting equations solved iteratively for varying insulation thicknesses. The following plot presents calculated temperatures versus insulation thickness if exterior radiation is also considered.



If only convection is considered on outer surface, following critical insulation thickness is obtained.



If both convective and radiation heat loss are considered, plot is changed as follows.



APPENDIX F

PDPA OPERATION AND ALIGNMENT

The 2-d PDPA system (manufactured by TSI, inc.) utilized in this study provides an accurate, simple method for obtaining droplet diameter and velocity statistics from sprays. The basis of this system is the following, 2 W, argon-ion laser.



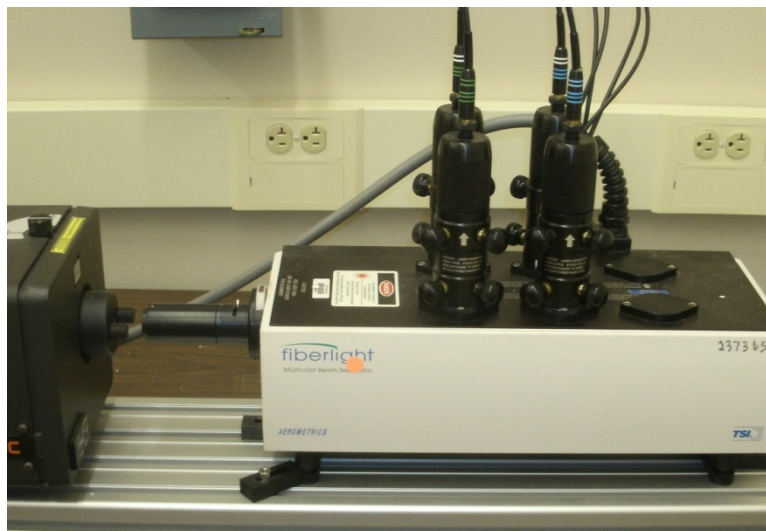
The laser is controlled and monitored using a simple digital interface connected to the laser power supply.



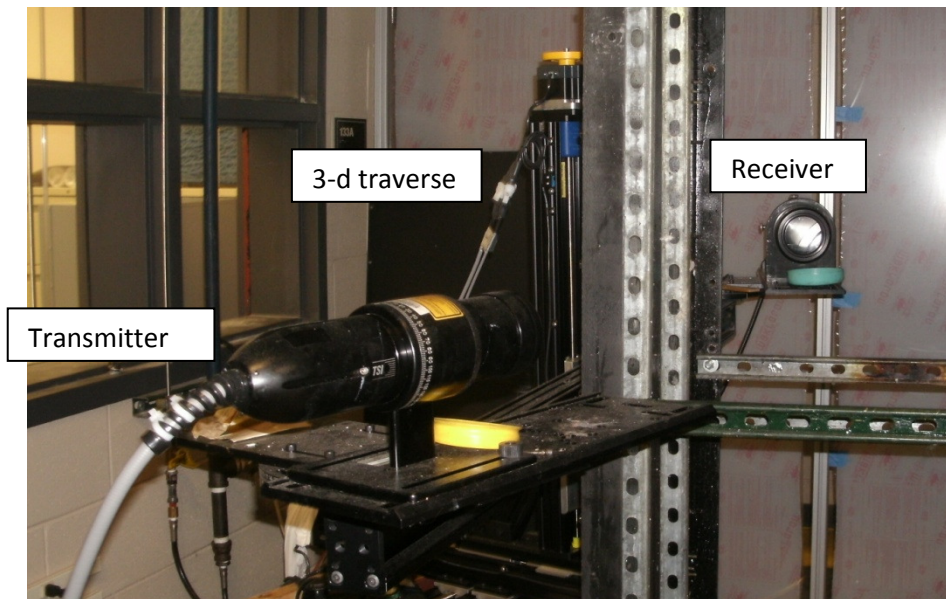
The power supply is cooled using a closed loop chiller with an adjustable cooling temperature.



After exiting the laser, the beam is separated into two sets of beams (514.5 nm and 488 nm wavelength). One beam of each set is then shifted by 40 MHz using a Bragg cell. The four beams are then directed onto fiber optic cables. All of this takes place in the following beam separator housing.



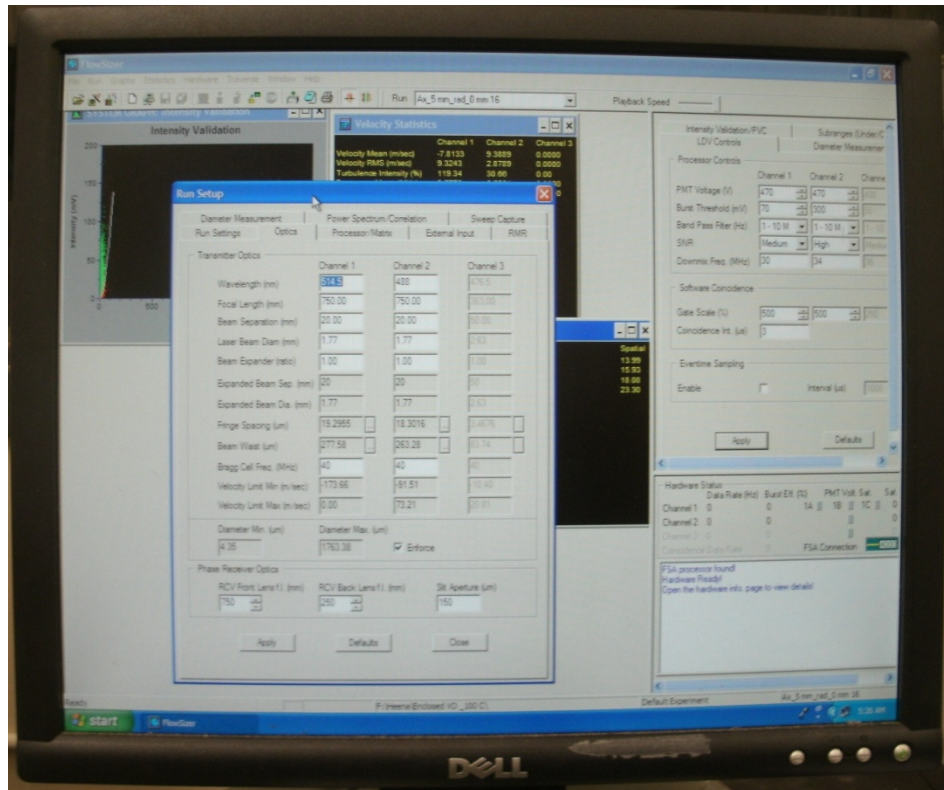
After leaving the beam separator, the beams travel via fiber optic cables to the PDPA transmitter. After exiting the transmitter, the beams meet in the measurement volume. Reflected signals that contain information about the spray are then collected by the PDPA receiver. The whole assembly is moved by a 3-d traverse.



The collected signals are then processed via TSI's external processors.



The analyzed signals are then sent to a desktop computer where they displayed and manipulated in TSI FlowSizer software.



While the PDPA system is set up in 2-d Cartesian coordinates, the sprays and their resulting information are best analyzed using cylindrical coordinates. In order to align the system for this conversion, the following steps must be taken. First, the axial distance of interest is obtained by moving the traverse system. Then, the point of highest axial velocity is manually searched for and obtained. This is considered the center of the spray. The following diagram shows the procedure for converting the Cartesian measurement into radial and swirl measurements. The black symbols represent the point of measurement. Once the center of the spray is found (where red lines cross), sweeping the radius parallel to the beam measurement direction (vertical red line) will give radial measurements in the spray. Sweeping the radius normal to the measurement direction (horizontal red line) will give swirl measurements.

